

EXPERIMENTAL AND NUMERICAL INVESTIGATION OF
REGENERATIVE COOLING WITH SUBCOOLED NUCLEATE BOILING IN
LIQUID ROCKET ENGINES

A THESIS SUBMITTED TO
THE GRADUATE SCHOOL OF NATURAL AND APPLIED SCIENCES
OF
MIDDLE EAST TECHNICAL UNIVERSITY



BY
MAHMUT MURAT GÖÇMEN

IN PARTIAL FULFILLMENT OF THE REQUIREMENTS
FOR
THE DEGREE OF DOCTOR OF PHILOSOPHY
IN
MECHANICAL ENGINEERING

JULY 2023

Approval of the thesis:

**EXPERIMENTAL AND NUMERICAL INVESTIGATION OF
REGENERATIVE COOLING WITH SUBCOOLED NUCLEATE BOILING
IN LIQUID ROCKET ENGINES**

submitted by **MAHMUT MURAT GÖÇMEN** in partial fulfillment of the requirements for the degree of **Doctor of Philosophy in Mechanical Engineering, Middle East Technical University** by,

Prof. Dr. Halil Kalıpçılar
Dean, Graduate School of **Natural and Applied Sciences**

Prof. Dr. Mehmet Ali Sahir Arıkan
Head of the Department, **Mechanical Engineering**

Prof. Dr. Cüneyt Sert
Supervisor, **Mechanical Engineering, METU**

Examining Committee Members:

Prof. Dr. Abdullah Ulaş
Mechanical Engineering, METU

Prof. Dr. Cüneyt Sert
Mechanical Engineering, METU

Prof. Dr. Almıla Güvenç Yazıcıoğlu
Mechanical Engineering, METU

Prof. Dr. Murat Köksal
Mechanical Engineering, Hacettepe University

Assist. Prof. Dr. Sıtkı Uslu
Mechanical Engineering, TOBB ETU

Date: 12.07.2023



I hereby declare that all information in this document has been obtained and presented in accordance with academic rules and ethical conduct. I also declare that, as required by these rules and conduct, I have fully cited and referenced all material and results that are not original to this work.

Name Last name : Mahmut Murat Göçmen

Signature :

ABSTRACT

EXPERIMENTAL AND NUMERICAL INVESTIGATION OF REGENERATIVE COOLING WITH SUBCOOLED NUCLEATE BOILING IN LIQUID ROCKET ENGINES

Göçmen, Mahmut Murat
Doctor of Philosophy, Mechanical Engineering
Supervisor: Prof. Dr. Cüneyt Sert

July 2023, 145 pages

Ever since the development of liquid rocket engines (LRE), there has been a need to cool the engine, i.e. combustion chamber and nozzle wall, to prevent thermal failure. The most common approach for this is regenerative cooling, where one or both of the propellants flow as coolants inside the passages of the engine walls before entering the injector. In this study, a complete tool set has been developed that enables design and simulation of regenerative cooling phenomenon during the design of an LRE. The developed set consists of three tools, a one-dimensional (1D) design tool, a two-dimensional (2D) heat conduction solver, and a three-dimensional (3D) two phase flow solver based on the free and open source computational fluid dynamics software, OpenFOAM. The 1D design tool is simple and fast, and uses thermal circuit modeling to investigate the effect of geometrical parameters on the cooling channel design. The 2D tool simulates heat conduction in the solid walls of the engine to predict wall temperatures using the finite difference technique. It also enables the use of nucleate boiling by locating the subcooled nucleate boiling onset point and using appropriate heat transfer rates. The 3D simulation tool is capable of solving two-phase nucleate boiling and conjugate heat transfer in real cooling channel geometries. In order to create an accurate and computationally efficient 3D

solver, different phase change models and model parameters have been investigated and their optimal combination of them for regenerative cooling channel simulations is selected. In addition, the developed computational tool set is validated through experiments on a straight cooling channel by using a test setup designed, manufactured and used as a part of this work.

Keywords: Liquid Rocket Engines, Regenerative Cooling, Subcooled Nucleate Boiling



ÖZ

SIVI YAKITLI ROKET MOTORLARINDA AŞIRI SOĞUTULMUŞ KABARCIKLI KAYNAMALI REJENERATİF SOĞUTMANIN DENEYSEL VE SAYISAL İNCELENMESİ

Göçmen, Mahmut Murat
Doktora, Makina Mühendisliği
Tez Yöneticisi: Prof. Dr. Cüneyt Sert

Temmuz 2023, 145 sayfa

Sıvı yakıtlı roket motorlarının (SYRM) geliştirilmeye başlanmasından bu yana, ısı sebeplerden başarısızlığa uğramaması için motoru (yanma odası ve lüle duvarları) soğutmaya ihtiyaç duyulmaktadır. SYRM'lerin soğutulması için en sık kullanılan teknik rejeneratif soğutmadır. Bu teknikte yakıtlardan biri ya da ikisi birden enjektöre girmeden önce motor duvarları içindeki kanallardan geçerek soğutucu olarak görev görür. Bu çalışmada, SYRM tasarlama sürecinde rejeneratif soğutmanın modellenmesini sağlayacak komple bir tasarım ve benzetim aracı geliştirilmiştir. Benzetim aracı üç çözücünden oluşmaktadır; bir boyutlu (1B) tasarım aracı, iki boyutlu (2B) ısı iletimi çözücüsü ve özgür, açık kaynaklı bir hesaplamalı akışkanlar dinamiği yazılımı olan OpenFOAM tabanlı bir üç boyutlu (3B) iki fazlı akış çözücüsü. 1B tasarım aracı, geometrik parametrelerin soğutma kanalı tasarımına etkisini incelemek için ısı devre modeline dayalı olarak çalışan en basit ve en hızlı yöntemdir. 2B model, sonlu farklar yöntemi kullanarak motorun katı kısmında çözüm yapıp duvar sıcaklıklarını tahmin etmekte ve buna ek olarak aşırı soğutulmuş kabarcıklı kaynamanın yerini belirleyerek ve buna göre ısı transferi değerlerini değiştirerek kabarcıklı kaynamanın tasarımlarda kullanılmasını sağlar. 3B benzetim aracı gerçek soğutma kanalı geometrileri için kabarcıklı kaynama ve eşlenik ısı

aktarımı hesabı yapabilmektedir. Doğruluđu yüksek ve hesaplama gücünü kullanım açısından verimli bir 3B çözücü oluşturmak için, farklı faz deđişimi modelleri ve model parametreleri incelenerek rejeneratif sođutma kanalı benzetimleri için en uygun olan kombinasyon seçilmiştir. Ayrıca araç seti, bu çalışmanın bir parçası olarak geliştirilen bir test düzeneđi kullanılarak düz bir sođutma kanalında yapılan çeşitli deneylerle doğrulanmıştır.

Anahtar Kelimeler: Sıvı Yakıtlı Roket Motoru, Rejeneratif Sođutma, Aşırı Sođutulmuş Kabarcıklı Kaynama





To my family

ACKNOWLEDGMENTS

I would like to express my deepest gratitude to my thesis supervisor Prof. Dr. Cüneyt Sert for his patience, guidance, advice, criticism, encouragements and insight throughout the research.

Roketsan Inc. is gratefully acknowledged for granting access to the test setup to carry out experiments in this research. The numerical calculations reported in this thesis were partially performed at TUBITAK ULAKBIM, High Performance and Grid Computing Center (TRUBA resources).

I would like to thank my thesis monitoring committee members Prof. Dr. Abdullah Ulaş and Assist. Prof. Dr. Sıtkı Uslu for their invaluable advices and support. Their positive feedbacks encouraged me to do more all through this work.

My colleagues at Roketsan Inc. provided invaluable assistance and support that greatly facilitated the completion of this thesis. First of all, I would like to express my deepest appreciation to Senem Gülmez for her friendship, encouragements, contributions and inexhaustible support in all parts of the thesis. I am very grateful to Gönenç Güldemet and Ufuk Kayabaşı without their help experimental work would not have been possible. I am also thankful to Mehmet Nazım Tomaç, Mehmet Can Köse, Erkan İlhan, Adil Topaloğlu, Rıdvan Arık, and Mevlüt Doğan for their efforts and support through the experiments. Many thanks to Aykut Sever, Oğuz Korkmaz, and Tolga Kurşun for their friendship and encouragements. I am also thankful to my manager Sevda Açık Akkuş for her understanding and support.

A special thanks to Ali Karakuş who generously provided his knowledge about computational sciences, advice and coffee. I would like to extend my sincere thanks to Alper Çelik for scientific discussions, edits and support.

Many thanks to Gökay Günacar, Merve Günacar, Kadir Ali Gürsoy, Merve Özdemir, Ahmet Alkan, Tufan Akba, Sinan Karamahmutoglu, and Erinç Erol for always being available for friendly chats, entertainment and moral support.

Lastly, this endeavor would not have been possible without my parents. Their belief in me has kept my spirits and motivation high during this process.



TABLE OF CONTENTS

ABSTRACT	v
ÖZ.....	vii
ACKNOWLEDGMENTS	x
TABLE OF CONTENTS	xii
LIST OF TABLES	xv
LIST OF FIGURES	xvi
LIST OF ABBREVIATIONS	xxi
LIST OF SYMBOLS.....	xxiii
CHAPTERS	
1 INTRODUCTION.....	1
1.1 Regenerative Cooling	6
1.2 Types of Boiling	11
1.3 Motivation of the Study.....	13
1.4 The Current Study	14
1.5 Structure of the Thesis.....	15
2 LITERATURE REVIEW	17
2.1 Regenerative Cooling	17
2.2 Modeling of Boiling	23
2.3 Experimental Studies on Flow Boiling.....	26
3 EXPERIMENTAL STUDY	31
3.1 Test Setup	31
3.1.1 Feeding System	31

3.1.2	Test Specimen	36
3.2	Uncertainty Analysis	39
3.3	Test Matrix	43
3.4	Test Results	44
4	ONE- AND TWO-DIMENSIONAL DESIGN TOOLS	49
4.1	One Dimensional (1D) Design Tool	50
4.1.1	Equivalent Thermal Resistance	51
4.1.2	Hot Gas Side Heat Transfer	53
4.1.3	Coolant Side Heat Transfer	54
4.1.4	Verification and Results	55
4.1.4.1	300 kN LOX/RP-1 Engine Cooled by RP-1	55
4.1.4.2	Comparison with Current Experiments	58
4.2	Two-dimensional Design Tool	59
4.2.1	Theoretical Background	59
4.2.2	Governing Equations	61
4.2.3	Prediction of the Onset of Nucleate Boiling (ONB)	66
4.2.4	Coolant Side Heat Transfer for Subcooled Flow Boiling Regime	67
4.2.5	Coolant Pressure Loss	68
4.2.6	Solution Procedure	69
4.3	Verification and Validation	72
4.3.1	89 kN LRE Cooled by Liquid Hydrogen	72
4.3.2	100 kN LRE Cooled by Liquid Oxygen	77
4.3.3	ONB on a Rectangular Channel Cooled by Water	79
4.3.4	23 kN Demonstration Thrust Chamber Cooled by MMH	83
4.3.5	Comparison with Current Experiments	86

5	3D CFD SOLVER	89
5.1	Theoretical Background	90
5.1.1	Mass, momentum and energy conservation	90
5.1.2	Interface tracking with volume of fluid method (VOF)	91
5.1.3	Phase change models	92
5.2	Verification and Validation Simulations	93
5.2.1	Horizontal Film Condensation (Stefan Problem)	94
5.2.2	Smooth Falling Film Condensation	96
5.2.3	Bubble Condensation	99
5.2.4	Rising Bubble Problem	102
5.2.5	Subcooled Flow Boiling in a Rectangular Channel	111
5.2.6	Comparison with Current Experiments	118
6	CONCLUSION	123
6.1	Conclusions	123
6.2	Recommendations for Future Work	124
	REFERENCES	127
	APPENDICES	
	A. Tabulated Results of Experiments	143
	CURRICULUM VITAE	145

LIST OF TABLES

TABLES

Table 2.1. Comparison of existing numerical simulation of boiling studies	24
Table 3.1. Component list of the test setup.....	35
Table 3.2. Test matrix with water being the coolant.....	44
Table 4.1. Grids used in mesh independence study	73
Table 4.2. Selected cases from experimental study (Liu et al., 2005) for validation of the 2D FDM Solver	80
Table 4.3. Comparison of the 2D FMD solver predictions of incipient heat flux against experimental results (Liu et al., 2005).....	81
Table 4.4. Maximum and mean absolute error values for 2D FDM solver's coolant bottom wall temperature predictions.....	86
Table 5.1. Fluid properties for isobutene at 25 °C	95
Table 5.2. Analysis details horizontal film condensation problem.....	96
Table 5.3. Fluid properties for the smooth falling film condensation problem	98
Table 5.4. Analysis details for the smooth falling film condensation problem	98
Table 5.5. Fluid properties for bubble condensation problem	100
Table 5.6. Analysis properties for bubble condensation problem.....	101
Table 5.7. Fluid properties, physical properties and dimensionless numbers for the rising bubble problem	104
Table 5.8. Comparison of terminal velocities of the rising bubble problem	107
Table 5.9. Terminal velocities of rising bubble (Case-2) with STAR-CCM+.....	110
Table 5.10. Performance comparison of uniform and AMR grids for Case-2.....	110
Table 5.11. Water properties for subcooled flow boiling in rectangular channel.	112
Table 5.12. Comparison of bubble growth and resulting grids of uniform and AMR grids at simulation physical times of 0, 200 and 400 ms ($\alpha = 1$ is pure liquid, $\alpha = 0$ is pure vapor, the bubble boundary is $\alpha = 0.5$)	114
Table 5.13. Computational performance comparison of uniform and AMR grids	116

LIST OF FIGURES

FIGURES

Figure 1.1. Heat flux distribution along an LRE wall (Sutton & Biblarz, 2017)	1
Figure 1.2. A regeneratively cooled LRE (“The British Library”, 2013)	2
Figure 1.3. Dump cooling schematic (Naraghi, 2015)	3
Figure 1.4. Film cooling schematic (Grisson, 1991)	4
Figure 1.5. A sample ablative engine design (Harmon, 2009)	5
Figure 1.6. Radiative cooling of Merlin 1D engine’s nozzle extension (NASA, 2017).....	5
Figure 1.7. Schematic and temperature profile of a regeneratively cooled LRE (Sutton & Biblarz, 2017; Naraghi, 2015)	7
Figure 1.8. Change of heat flux of a typical propellant in various heat transfer regions (Huzel et al., 1992)	9
Figure 1.9. a) Pool boiling modes (Incropera, 2007) b) Forced convection boiling modes (Castro, Maprelian & Ting, 2001)	12
Figure 2.1. First regeneratively cooled thrust chamber (Crocco, 1967).....	18
Figure 2.2. A sample 2D temperature distribution on a cross section of a LRE wall (Naraghi, 2002).....	19
Figure 2.3. A sample result from 3D regenerative cooling channel simulation (from left to right, velocity vector, pressure, temperature distribution of the coolant) (Froelich et al., 1991)	20
Figure 2.4. Velocity profiles of coolant for different channel aspect ratios (Boysan, 2008).....	21
Figure 2.5. Thermal nozzle test specimen (Torres & Desmet, 2008).....	22
Figure 2.6. Nucleate boiling process in a microchannel retrieved from the study of Liu, Lee and Garimella (2005)	27
Figure 2.7. Flow patterns taken from the study of Galvis and Gulham (2012).....	28
Figure 3.1. Piping and instrumentation diagram of the test setup	32
Figure 3.2. Test setup	36

Figure 3.3. 3D model of the test specimen design and a photograph of the actual manufactured part	37
Figure 3.4. Top view showing thermocouple port distances and numbering of stations	38
Figure 3.5. Cross-sectional view showing thermocouple port distances	39
Figure 3.6. Change in wall temperature with respect to heat input (black horizontal lines denotes uncertainty of each wall heat flux value)	46
Figure 3.7. Change in heat transfer coefficient with respect to wall superheat (black horizontal lines denotes uncertainty of each value)	47
Figure 4.1. Main regenerative cooling channel design parameters.....	49
Figure 4.2. 1D design tool; an equivalent thermal resistances (left), an engine subdivided into stations (right) (Naraghi, 2002).....	51
Figure 4.3. Hot gas side wall temperature change along Boysan’s engine (Boysan, 2008)) for 4 different nozzle efficiency values (channel geometry: $ch = 4$ mm, $cw = 4$ mm, $N_{cc} = 100$)	56
Figure 4.4. Effect of channel height and aspect ratio on maximum gas side wall temperature	57
Figure 4.5. Effects of number of channels on maximum gas side wall temperature (channel geometry: $ch = 4$ mm, $cw = 2$ mm).....	58
Figure 4.6. Comparison of coolant wall temperature change along the test specimen for Test-2.....	59
Figure 4.7. Detailed view of a station (left) and finite difference grids and boundary conditions superimposed on computational domain (right).....	61
Figure 4.8. Resistances and heat fluxes of a typical interior node (Reproduced from Naraghi, 1987)	62
Figure 4.9. 2D FDM solver algorithm	71
Figure 4.10. Combustion chamber contour with bifurcation regions indicated (Wadel, 1997)	73

Figure 4.11. Wall temperature values with grids used in mesh independence study (hot gas side wall temperature on the left axis and chamber radius on the right axis)	74
Figure 4.12. Comparison of hot gas side wall temperature along the nozzle with the reference studies (Wadel & Meyer, 1996; Boysan, 2008; Suer et al., 2019) (hot gas side wall temperature on the left axis and chamber radius on the right axis)	75
Figure 4.13. Ideal rib thermocouple placement (Wadel & Meyer, 1996)	76
Figure 4.14. Rib thermocouple temperature comparison of reference experimental and analysis (Wadel & Meyer, 1996; Suer et al., 2019) versus current analysis results (rib thermocouple temperature on the left axis and chamber radius on the right axis).....	77
Figure 4.15. Comparison of the inner wall and coolant temperature along the nozzle with the reference study (Naraghi & Armstrong, 1988) (temperature on the left axis and chamber radius on the right axis).....	78
Figure 4.16. a) 3-D view of test section and right, b) cross section of test section (Liu et al., 2005)	79
Figure 4.17. Visualization of validation Case-1 by Liu et al. (Liu et al., 2005).....	80
Figure 4.18. The coolant and channel bottom wall temperature change across the channel ($x_{inlet} = 25.4$ mm and $x_{outlet} = 0$ mm) for of Case-1 (calculated by the 2D FDM solver).....	82
Figure 4.19. Temperature distribution at the outlet of the channel for Case-1 (calculated by the 2D FDM solver)	83
Figure 4.20. Change of hot gas side wall temperature along the DTC nozzle compared to the reference study (Pauckert & Tobin, 1975)	84
Figure 4.21. Change of hot gas side wall temperature along the DTC nozzle for different FoS values (filled circles indicates locations of boiling).....	85
Figure 4.22. Comparison of experimental (Test-2 and Test-7) cooling channel bottom wall temperature with 2D FDM solver across the test specimen (dark red dots in dark circles denotes the part of the specimen where boiling occurs)	87
Figure 5.1. Problem domain for horizontal film condensation (Stefan Problem)...	95

Figure 5.2. Film thickness growth of the Stefan problem.....	96
Figure 5.3. Problem domain for smooth falling film condensation (Nusselt Problem).....	97
Figure 5.4. Wall heat flux result comparison for the smooth falling film condensation problem	99
Figure 5.5. Solution domain and boundary conditions that are used for bubble condensation problem in this study.....	100
Figure 5.6. Heat transfer coefficient comparison for the bubble condensation problem (Ranz & Marshall, 1952)	102
Figure 5.7. Solution domain and boundary conditions for the rising bubble problem	103
Figure 5.8. Comparison of final shapes of the bubble for Case-1, (a) reference 2D simulation by Hysing et al. (2009), (b) current 3D simulation on $z = 0$ plane, (c) current 3D simulation with AMR on $z = 0$ plane (alpha indicates the phase, alpha=1 is pure liquid and alpha=0 is pure vapor).....	105
Figure 5.9. Comparison of final shapes of the bubble for Case-2, (a) experimental result by Bhaga and Weber (1981), (b) current 3D simulation on $z = 0$ plane (c) current 3D simulation with AMR on $z = 0$ plane	106
Figure 5.10. Comparison of final shapes of the bubble for Case-2, (a) reference 2D simulation by Hysing et al. (2009), (b) reference 3D simulation by Hua and Lou (2007), (c) current 3D simulation on $z = 0$ plane	106
Figure 5.11. Bubble shape development for Case-2 of the rising bubble problem	108
Figure 5.12. Comparison of final shapes of the bubble on $z = 0$ plane for the Case-2 , (a) current 3D OpenFOAM simulation with uniform mesh, (b) current 3D STAR-CCM+ simulation with uniform mesh, (c) current 3D OpenFOAM simulation with AMR and (d) current 3D STAR-CCM+ simulation with AMR .	109
Figure 5.13. 3-D view of mini-channel test section (Liu et al., 2005).....	111
Figure 5.14. Domain and boundary conditions for flow boiling analyses.....	112
Figure 5.15. Comparison of the bubble growth with reference experimental (Liu et al., 2005) and numerical (Zhuan & Wang, 2010) studies	115

Figure 5.16. Effect of mass transfer model coefficients ($rl = rv = 1, 2, 4, 8$) on bubble growth.....	117
Figure 5.17. Domain and boundary conditions for the simulation of Test-7	118
Figure 5.18. Comparison of the coolant bottom wall ($x = 0.75$ mm line) temperature with experiment data (Test-7)	119
Figure 5.19. Predicted bubble radius change by simulation through the channel for Test-7	120
Figure 5.20. A snapshot of the simulation at the 400 ms, (a) bubble locations on the channel ($z = 250 - 255$ mm), (b) the shape of the bubble that indicated with dashed lines square on $x = 0$ mm line (the bubble boundary is transparent pale blue with $alpha = 0.5$)	121
Figure 5.21. The velocity vectors (in black) around the bubble at the 400 ms, the length of the arrows indicates the velocity magnitude, gray lines shows the grid element edges (the bubble boundary is transparent pale blue with $alpha = 0.5$)	121

LIST OF ABBREVIATIONS

ABBREVIATIONS

1D	One-dimensional
2D	Two-dimensional
3D	Three-dimensional
CFD	Computational Fluid Dynamics
FEM	Finite Element Method
FVM	Finite Volume Method
HARCC	High Aspect Ratio Cooling Channel
LRE	Liquid Rocket Engine
LOX	Liquid Oxygen
LS	Level Set
LSM	Level Set Method
MAE	Mean Absolute Error
MMH	Monomethylhydrazine
NASA	National Aeronautics and Space Administration
NIST	National Institute of Standards and Technology
OFHC	Oxygen Free high Conductivity Copper
ONB	Onset of Nucleate Boiling
OpenFOAM	Open Source CFD Solver

PLIC	Piecewise Linear Interface Calculation
P&ID	Piping and Instrumentation Diagram
RANS	Reynolds-Averaged Navier-Stokes
ROCCID	Rocket Combustor Interactive Design
RP-1	Rocket Propellant-1, Kerosene
RTE	Rocket Thermal Evaluation
TDK	Two-Dimensional Kinetics
UDF	User Defined Function
VOF	Volume of Fluid

LIST OF SYMBOLS

SYMBOLS

Latin Symbols

A	Cross-sectional area, m ²
Bo	Boiling number
c	Specific heat capacity, J/(kg · K)
c_p	Specific heat capacity at constant pressure, J/(kg · K)
C	Constant
C_{cl}	Coolant constant
C^*	Characteristic velocity, m/s
Cg	Correlation Coefficient
ch	Cooling channel height, m
cw	Cooling channel width, m
d_t	Diameter of nozzle throat, m
D	Diameter, m
Eo	Eötvös number
\dot{E}	Energy, J
f	Darcy friction factor
\vec{f}_{st}	Surface tension force, N
\vec{g}	Gravitational acceleration, m/s ²

G	Mass flux, $\text{kg}/(\text{m}^2 \cdot \text{s})$
h	Heat transfer coefficient, $\text{W}/(\text{m} \cdot \text{K})$
h_{fg}	Latent heat, J/kg
h_{lv}	Latent heat, J/kg
h_m	Element edge length, μm
H_c	Mini-channel height, μm
i_{LV}	Enthalpy of phase change, kJ/kg
k	Thermal conductivity, $\text{W}/(\text{m} \cdot \text{K})$
L	Length of the current station, m or total width under the cooling channel, m
M	Mach number or Molecular weight, kg/kmol
\dot{m}	Mass change between two phases, kg/s or mass flow rate, kg/s
Mo	Morton number
N	Number of tests
N_{cc}	Number of cooling channels
p	Pressure field, Pa
P_c	Combustion chamber pressure, Pa
P_g	Combustion chamber pressure, Pa
Pr	Prandtl number
q	Heat, W
\dot{q}_{pc}	Phase change rate

q''	Heat flux, W/m ²
Q	Heat, W
r_l	Empirical rate parameter
r_v	Empirical rate parameter
rf	Recovery factor
R	Radius, m or universal gas constant, J/(K · mol) or function of variables or resistance
R_{tc}	Curvature of nozzle throat, m
Re	Reynolds number
t	Time, s or thickness, m
T	Temperature, K or temperature field
T_f	Coolant Temperature, K
T_c	Stagnant combustion chamber temperature, K
T_{cl}	Coolant bulk temperature, K
T_{cs}	Coolant static temperature, K
T_{g0}	Stagnant combustion gas temperature, K
T_{HGSWT}	Hot gas side wall temperature, K
T_{sat}	Saturated boiling temperature, K
T_w	Wall temperature, K
t	Thickness, m or Liner thickness, m
\vec{u}	Velocity field, m/s

U_{∞}	Bubble terminal rising velocity, m/s
V	Velocity, m/s
\dot{V}	Volumetric flowrate, m ³ /s
w_c	Mini-channel width, μm
x	Variable

Greek Symbols

α	Volume fraction
γ	Ratio of specific heats
δ	Fin thickness, m
ΔR	Radial distance between cells, m
ΔT	Temperature difference, $^{\circ}\text{C}$
$\Delta\phi$	Angular distance between cells, $^{\circ}$
η	Efficiency or fin efficiency
μ	Dynamic viscosity, Pa · s
ρ	Density, kg/m ³
σ	Correction factor
ω_R	Overall uncertainty
ω_x	Uncertainty interval of variables

Letter-Like Symbols

\forall	Volume, m ³
-----------	------------------------

Subscripts

<i>an</i>	Analytical solution
<i>aw</i>	Adiabatic wall
<i>bub</i>	Bubble
<i>c</i>	Convective or coolant
<i>cl</i>	Coolant side or coolant
<i>cs</i>	Coolant side
<i>cond</i>	Condensation or conduction
<i>conv</i>	Convection
<i>eq</i>	Equivalent
<i>evap</i>	Evaporation
<i>f</i>	Fin
<i>fg</i>	Fluid to gas, phase change
<i>g</i>	Hot gas side
<i>gen</i>	Generation
<i>h</i>	Hydraulic
<i>i,j</i>	Indices
<i>in</i>	Inlet
<i>l</i>	Liquid
<i>l,s</i>	Saturated liquid
<i>n</i>	Station
<i>out</i>	Outlet

<i>pc</i>	Phase change
<i>pred</i>	Prediction
<i>sat</i>	Saturation
<i>sim</i>	Simulation
<i>sp</i>	Single-phase
<i>t</i>	Throat
<i>test</i>	Test
<i>tp</i>	Two-phase
<i>v</i>	Vapor
<i>v, s</i>	Saturated vapor
<i>w</i>	Liner
<i>wc</i>	Coolant side wall
<i>wg</i>	Gas side wall

Superscripts

<i>l</i>	Gauss-Seidel iteration index
----------	------------------------------

CHAPTER 1

INTRODUCTION

Since the mid-1940s liquid rocket engines (LRE) have been an indispensable part of both military rockets and launch vehicles. LRE cooling is an important part of the engine design because of the high combustion temperatures (1900 – 3900 K) (Sutton & Biblarz, 2017) and the resulting high heat fluxes (0.8 – 160 MW/m²) (Huzel, Huang & Arbit, 1992). These heat flux values show that 0.5 – 5 % of the total energy emerging from propellants are transferred to the engine walls (Sutton & Biblarz, 2017). Figure 1.1 shows a typical heat flux distribution along an LRE wall.

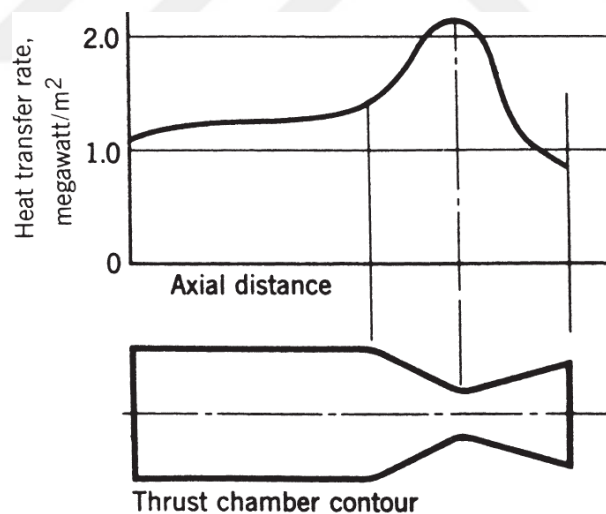


Figure 1.1. Heat flux distribution along an LRE wall (Sutton & Biblarz, 2017)

For short firing durations up to 2-3 seconds (Wadel & Meyer, 1996), engines can withstand the generated heat by utilizing the heat capacity of their own mass without using any other cooling method (Huzel et al., 1992). On the other hand, one or more

cooling methods are required to operate an LRE in steady-state working conditions. The most commonly used cooling techniques in LREs are as follows;

1. Regenerative cooling: Regenerative cooling is the most frequently used cooling method in LREs. One or both of the propellants (usually fuel) pass through channels in the engine walls of the combustion chamber and the nozzle before travelling to the injector (see Fig. 1.2). The coolant absorbs the heat transferred from the hot combustion gases to the walls and keeps them below their melting temperatures.

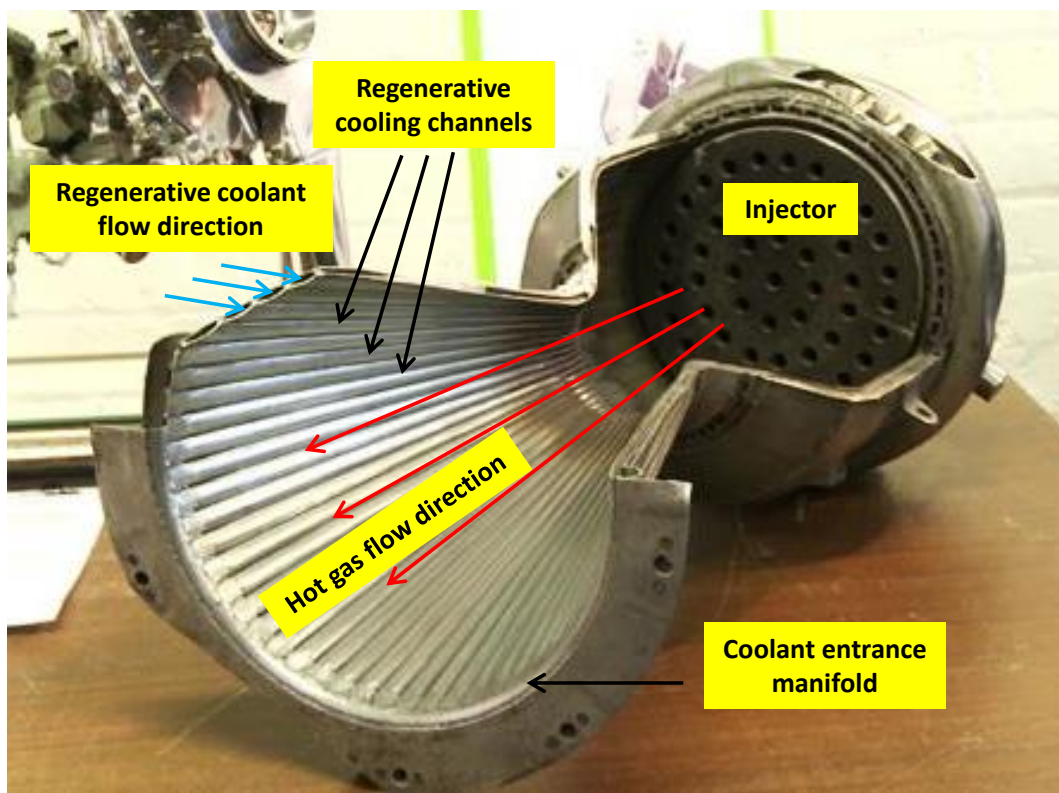


Figure 1.2. A regeneratively cooled LRE (“The British Library”, 2013)

2. Dump Cooling: Similar to regenerative cooling, coolant flowing through channels inside the engine walls provides the necessary cooling. As can be seen in Fig. 1.3, the coolant is discharged at the end of nozzle, which distinguishes it from regenerative cooling. Due to its low density and high specific heat, it is preferred only in systems using liquid hydrogen as propellant (as well as coolant). The

expulsion of some unburned propellant makes this method inefficient, although it produces some extra thrust.

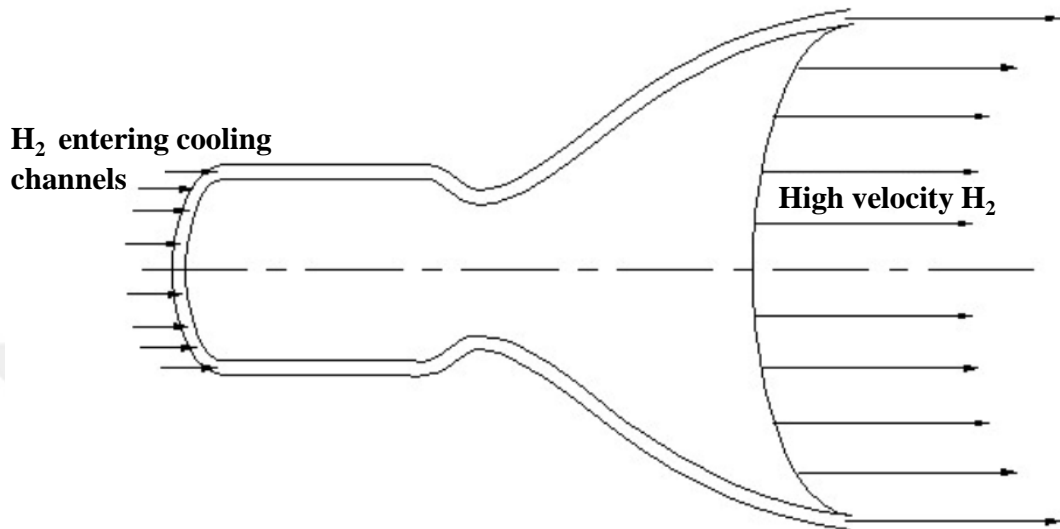


Figure 1.3. Dump cooling schematic (Naraghi, 2015)

3. Film cooling: As coolant, the fuel is sent to the combustion chamber walls through small holes or slits around the injector as a thin sheet. If sending the film layer only from the injector is not enough, more film cooling stations can be added throughout the chamber. The film layer can be liquid or gas. Figure 1.4 shows a simple schematic of this technique. The film sheet formed creates a boundary layer between the hot combustion gases and the engine walls, reducing the heat reaching LRE walls.

4. Transpiration cooling: Transpiration cooling is a special type of film cooling. A small portion of the fuel is sent as coolant into the combustion chamber through very small holes or porous engine walls.

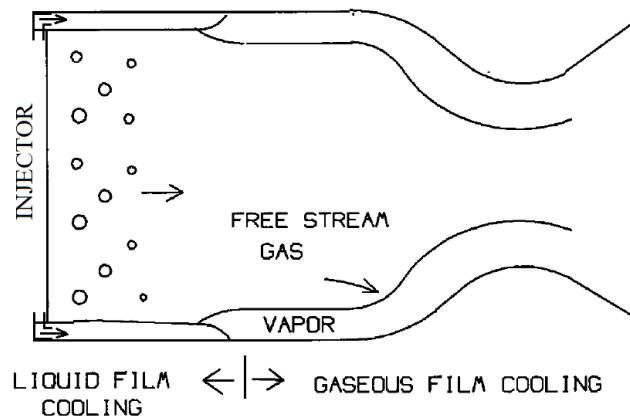


Figure 1.4. Film cooling schematic (Grison, 1991)

5. Ablative cooling: The chamber wall is constructed or coated with a material that will evaporate and corrode away during engine firing. The vaporization process is endothermic and creates a cooler boundary layer on the inner wall of the LRE. Figure 1.5 shows an ablative engine design. Ablative materials are also good insulators and slow down heat transfer to the structural outer shell. The downside is that engine nozzle geometry changes during engine operation due to abrasion of the ablative material.

6. Radiative cooling: The heat radiates away from the surface of the outer engine wall. Its use is limited to small thrusters, where the amount of material required is low, and nozzle extensions of large thrusters, where temperature values are below 1500 K. Special materials such as Niobium, Wolfram and Titanium carbide with sufficient strength even at high temperatures are required to withstand the loads. Figure 1.6 shows Merlin 1D Niobium nozzle extension.

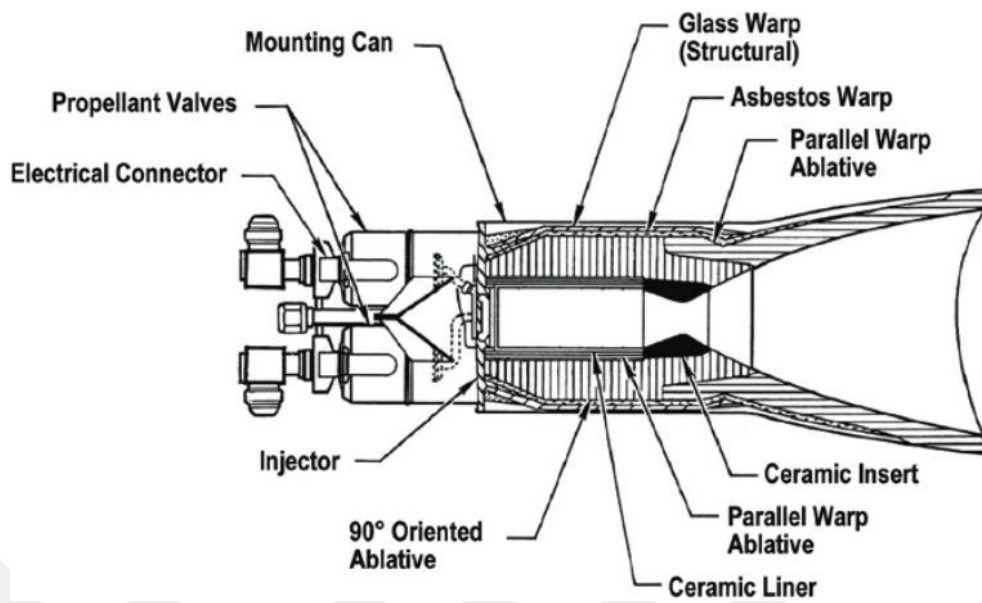


Figure 1.5. A sample ablative engine design (Harmon, 2009)



Figure 1.6. Radiative cooling of Merlin 1D engine's nozzle extension (NASA, 2017)

Of all the cooling methods listed above, regenerative cooling is the most common for LREs. Its details are presented in the next section.

1.1 Regenerative Cooling

In addition to keeping engine temperature under control, regenerative cooling provides an increase in the internal energy of the coolants (fuel) as they return to the injectors. The increase in internal energy results in 0.1 – 1.5 % speed increase at the nozzle outlet (Sutton & Biblarz, 2017). The main disadvantage is the pressure drop introduced by the channels. An appropriate design should guarantee the lifetime characteristics of the LRE while keeping the pressure losses to a minimum. This is a challenging task because of the interdisciplinary nature of the problem. Hot gas side heat transfer from the combustion chamber to the wall depends on the propellants, chamber pressure, the single injector configuration (impinging elements, coaxial swirls etc.) and multi-element injector pattern with film cooling design. Between the hot gas side and the coolant side, there is heat conduction through the wall. Temperature gradients of more than 500 K/mm are common in the liner. The design and geometry of the cooling channels have a major impact on the weight, manufacturing requirements, cost and lifetime of the engine. Figure 1.2 shows a cutaway of a real LRE with regenerative cooling. Figure 1.7 illustrates the temperature variation from the centerline to the outside of the engine along with a schematic of regenerative cooling.

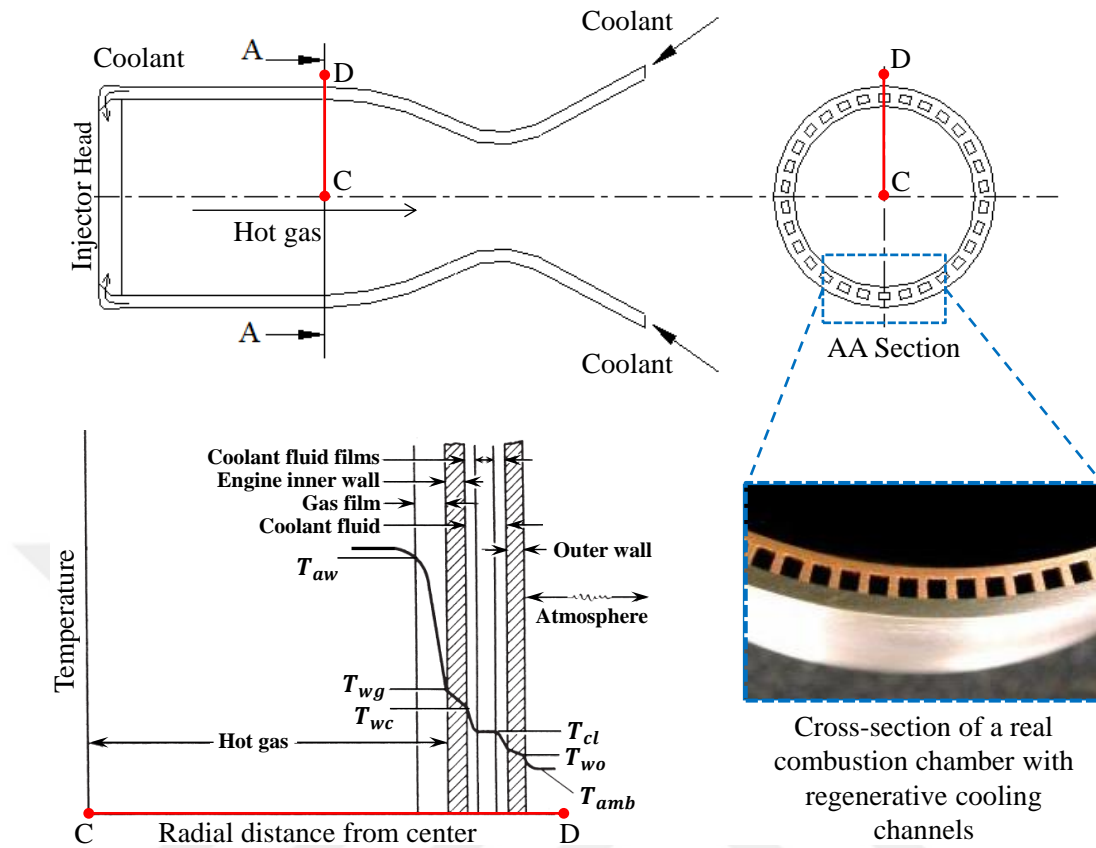


Figure 1.7. Schematic and temperature profile of a regeneratively cooled LRE (Sutton & Biblarz, 2017; Naraghi, 2015)

For a regeneratively cooled LRE, the heat transfer takes place between two dynamic fluids, the hot combustion gases and the coolant, separated by a wall, if the heat transfer between the atmosphere and the engine wall is ignored. The steady-state form of heat transfer from the hot combustion gases to the coolant is summarized in Equations (1.1) - (1.4) given below;

$$q_g'' = h_g(T_{aw} - T_{wg}) \quad (1.1)$$

$$q_w'' = \frac{k_w}{t_w}(T_{wg} - T_{wc}) \quad (1.2)$$

$$q_{cl}'' = h_{cl}(T_{wc} - T_{cl}) \quad (1.3)$$

$$q_g'' = q_w'' = q_{cl}'' \quad (1.4)$$

where T_{aw} , T_{wg} , T_{wc} and T_{cl} are adiabatic wall temperature, gas side wall temperature, coolant side wall temperature and coolant bulk temperature as shown in Fig. 1.7. k_w and t_w are the conductivity and thickness of the liner (inner wall of combustion chamber). Finally, h_g and h_{cl} are the hot gas side and coolant side convective heat transfer coefficients. Equation (1.1) represents the heat transfer rate from the hot combustion gases to the LRE walls. Equation (1.2) is for the heat transfer rate due to conduction on the inner wall of the combustion chamber. The heat flux from the combustion chamber wall to the coolant is shown in Equation (1.3). If radiative heat transfer is ignored in Equations (1.2) and (1.3), the heat fluxes, q_g , q_w and q_{cl} , will be equal. Considering these equations, the main objective of regenerative cooling is to keep h_g low, k_w/t_w and h_{cl} high.

The heat transfer mode between the engine wall and the coolant is forced convection. There are many factors that contribute to the convective heat transfer coefficient, h_{cl} . The propellants used for the coolant can become corrosive, decompose, or deposit impurities under high temperatures and heat fluxes, thereby reducing cooling efficiency (Huzel et al., 1992). Under these circumstances, the only way to determine actual convective heat transfer coefficient, h_{cl} , is to perform experiments or conduct detailed 3D computational fluid dynamics simulations.

The coolant side heat transfer characteristic is mainly determined by the coolant pressure and the regenerative cooling channel wall temperature. Figure 1.8 shows the relation between wall temperature and heat flux for a typical coolant under constant bulk temperature, pressure and velocity. Curves A and B indicate the heat transfer behavior for coolant pressures above and below the critical pressure, respectively. Being above or below the critical pressure is important as it determines the boiling probability of the coolant. A detailed description of the different parts of the curve A is as follows;

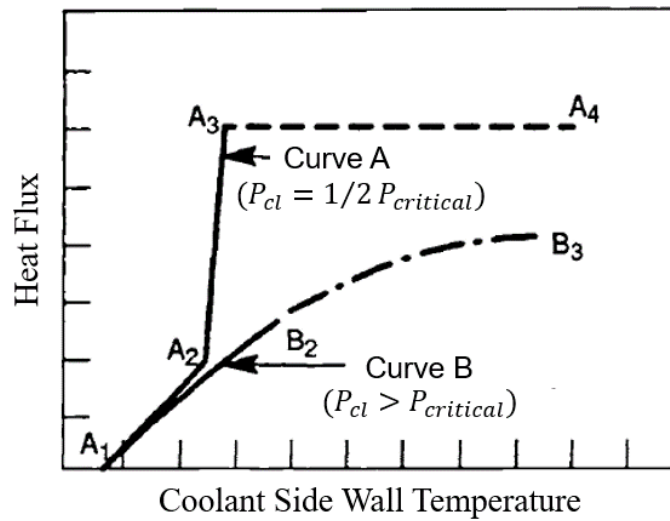


Figure 1.8. Change of heat flux of a typical propellant in various heat transfer regions (Huzel et al., 1992)

- **Section A1-A2:** This part is for forced convection heat transfer only, without boiling. The cooling channel walls are below the saturation temperature of the coolant.
- **Section A2-A3:** In this section, the wall temperatures are higher than the saturation temperature of the coolant. Bubbles that form near the wall condense back to the liquid phase; a phenomenon known as *nucleate boiling*. A small increase in wall temperature increases the heat flux significantly, as can be seen in Fig. 1.8.
- **Section A3-A4:** The increase in the wall temperature beyond point A3 causes an increase in bubble formation around the wall and therefore creates a bubble film. This process is called *film boiling*. The heat transfer coefficients are lower than those of nucleate boiling.

For curve B, the pressure is higher than the critical pressure of the coolant, therefore boiling cannot occur. Detailed explanations of different sections of curve B are as follows;

- **Section A₁-B₂:** This is the region where the wall temperature is lower than the critical temperature of the coolant. The convective heat transfer coefficient is constant and the wall temperature increases continuously with increasing heat flux.
- **Section B₂-B₃:** The wall temperature reaches the critical temperature of the coolant at point B₂. As the wall temperature increases beyond B₂, a stable supercritical vapor film boundary layer slowly develops, resulting in slightly lower heat transfer coefficients.

If applicable, a coolant operating pressure between 0.3 to 0.7 of the critical pressure should be used to take advantage of the high heat transfer coefficients that can be achieved by nucleate boiling (Huzel et al., 1992). Using the Sieder-Tate (1936) correlation given in Equation (1.5), the heat transfer coefficients in the A₁-A₂ and A₁-B₂ regions for turbulent flows can be predicted with reasonable accuracy. The constant C_{cl} in Equation (1.5) needs to be determined for each coolant.

$$Nu_{cl} = \frac{h_{cl}D_h}{k_{cl}} = C_{cl}Re_{cl}^{4/5}Pr_{cl}^{1/3}\left(\frac{\mu_{cl}}{\mu_{wc}}\right)^{0.14} \quad (1.5)$$

Almost all of the Nusselt correlations, like the Sieder-Tate equation, have been developed for straight channels, but secondary flows inside curved cooling channels change heat transfer rates (Froelich, Immich, Lebail, Popp & Scheuerer, 1991). Moreover, the number of correlations for nucleate boiling flows in curved channels is very small, and those that exist are all for water. The experiments needed to develop these correlations are both expensive and challenging because rocket engines and cooling channels can vary greatly in both geometry and size, and almost all propellants used as coolants must be handled with great care (corrosive, suffocating, carcinogenic, etc.). Therefore, a computational fluid dynamics (CFD) tool capable of solving two-phase flow inside cooling channels with phase change has potential use in combination with 1D and/or 2D preliminary design tools to provide initial guidance to the CFD simulations.

1.2 Types of Boiling

Modeling the boiling process is one of the challenging problems of computational fluid dynamics. The two-phase and chaotic nature of the problem is still being actively studied. The boiling phenomenon can be classified in the following two ways.

1. Based on the relative bulk motion of the liquid with respect to the heating surface

- **Pool boiling:** The liquid is stationary and its motion near the heating surface is due to free convection and mixing, driven by bubble growth and detachment. The different phases can be seen in Fig. 1.9a (Incropera, 2007).
- **Forced convection boiling:** Fluid motion is induced by external means in addition to free convection and bubble induced mixing, as shown in Fig. 1.9b (Incropera, 2007). Kakaç and Yener (1995) state that “the boiling heat transfer process is considerably more complicated and more difficult to correlate in situations where the liquid is forced to flow past the heater....there is no general, definitive method correlating flow boiling data.”

2. Based on temperature of the liquid

- **Subcooled boiling:** The liquid temperature is below the saturation temperature. Bubbles formed near the heated surface may collapse back to the liquid phase (Incropera, 2007).
- **Saturated boiling:** Temperature of the liquid is slightly higher than the saturation temperature. The bubbles formed rise in the liquid from the heated surface to the free surface (Incropera, 2007).

In the case of regenerative cooling of LREs, subcooled forced convection cooling is expected (Kakaç & Yener, 1995; Dhir, 1998).

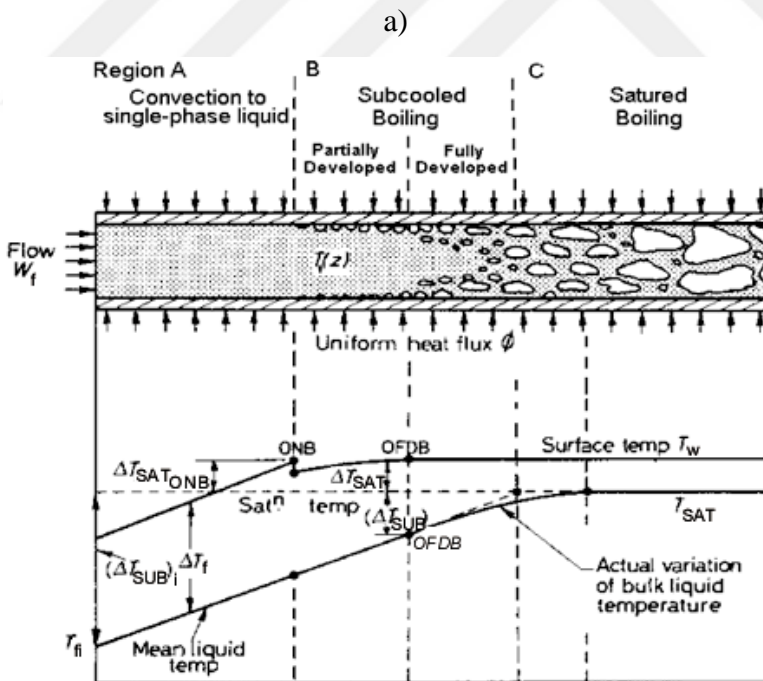
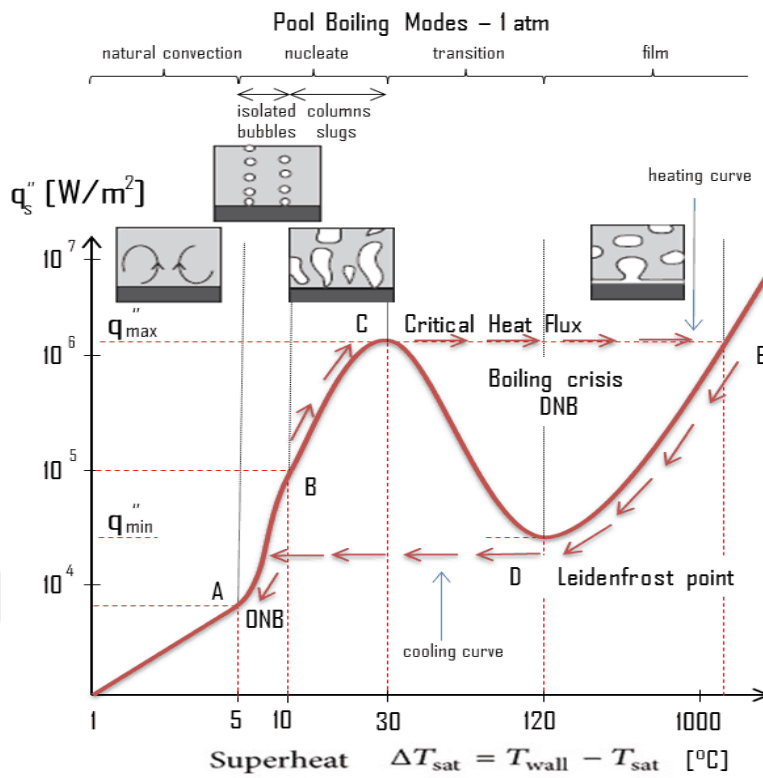


Figure 1.9. a) Pool boiling modes (Incropera, 2007) b) Forced convection boiling modes (Castro, Maprelian & Ting, 2001)

1.3 Motivation of the Study

LREs are preferred for launch vehicles because of their high specific impulse, restart capability and reusability. The cooling method of the engine is chosen by considering weight and performance. In a regeneratively cooled rocket engine, fuel or oxidizer flows through passages in the combustion chamber and nozzle walls and is then fed into the combustion chamber with increasing enthalpy. Accurate prediction of the wall temperatures is critical because the engine must be designed to withstand these temperatures and thermal stresses. To check for degradation and coking that can occur with hydrocarbon fuels along the cooling channels, accurate temperature and pressure predictions should be done. It is also necessary to know any change in the enthalpy of the fuel to determine the actual thrust level of the LRE. To make a fail-safe design, it is also important to consider situations with higher than expected heat loads, such as engines with blocked channels and uneven coolant distribution.

Considering two hypothetical engines of different sizes with the same fuel and the same combustion chamber pressure, the smaller one which generates lower thrust is more critical for cooling. This is due to the fact that as the thrust decreases, the combustion chamber volume as well as the amount of fuel burned decreases one order of magnitude faster than the surface area (Dobrovolski, 2018). Therefore, in the engine with lower thrust, a smaller amount of coolant is available per unit combustion chamber area that needs to be cooled. Pressure-fed LREs can be considered as low thrust systems and hence there will be just enough amount of fuel to cool the engine walls. Also, the budget for pressure loss in the cooling channels will be only a few bars because an increase in pressure loss increases the tank pressure and therefore, increases the LRE stage mass. All the aforementioned limitations enforce the selection of the most efficient cooling strategy. In cases where convective heat transfer is insufficient for engine cooling, nucleate boiling is the strongest candidate, providing the highest heat transfer coefficients as can be seen in Fig. 1.8. Unfortunately, there is a lack of regenerative cooling design studies using nucleate boiling in the literature.

1.4 The Current Study

The main objective of this thesis is to develop a complete design and simulation toolset that enables the modeling of the regenerative cooling phenomena during the design of an LRE. The toolset should be able to investigate different cooling channel designs, predict wall and coolant temperatures and calculate pressure drop in the channels, accurately. In order to design engines with demanding cooling requirements, the ability to use nucleate boiling, which is not available in the literature, is also added to the toolkit. A series of experiments are performed on a single channel test specimen to validate the models used and the solvers developed. The developed computational tools and their capabilities are summarized as follows;

1. One-dimensional (1D) design tool: This tool is based on thermal circuit methodology. Appropriate heat transfer correlations are used for both hot gas and coolant side heat transfers. The tool allows the investigation of four critical cooling channel design parameters, namely liner thickness (t), cooling channel height (ch), cooling channel width (cw) and number of cooling channels (N_{cc}).
2. A two-dimensional (2D) finite difference method (FDM) solver: This is capable of predicting engine wall temperature distribution. Moreover, it calculates the change of the bulk coolant temperature and pressure along the regenerative cooling channel. It can locate the onset point of subcooled nucleate boiling and modify the heat transfer rate accordingly.
3. 3D CFD solver: A multiphase solver capable of simulating subcooled nucleate boiling is developed based on the OpenFOAM framework. It can work with different phase change models. It can perform adaptive mesh refinement (AMR) for accurate and efficient simulations.

1.5 Structure of the Thesis

This thesis consists of the following six chapters:

Chapter 1 gives a brief overview about cooling techniques in liquid rocket engines and discusses liquid rocket engine cooling methods and boiling types.

Chapter 2 presents a comprehensive literature review on experimental and numerical studies on regenerative cooling. The historical development of boiling modeling is discussed in detail. The experimental investigation of flow boiling in the literature is also provided.

Chapter 3 provides information about the experimental part of this thesis. The test setup is described in two main parts: the feeding system and the test specimen. The test matrix and results are discussed.

Chapter 4 focuses on the developed 1D and 2D solvers. The modelling approach used in the 1D solver and its validation are presented. The theoretical background and flowchart of the 2D solver are given in detail. The implementation details of nucleate boiling detection and heat transfer rate calculation are also explained. The chapter is closed with 5 different verification and validation cases. Furthermore, the results obtained by 1D and 2D solvers under the experimental conditions described in Chapter 3 are compared with the test data obtained to validate these solvers.

Chapter 5 discusses the developed two-phase OpenFOAM solver. Details of the governing equations, VOF method and phase change models are presented. The solver used is validated with three different analytical cases. The AMR implementation and its computational advantage is demonstrated on a rising bubble benchmark problem. Finally, the ability to model subcooled nucleate boiling is verified by two experimental studies.

Chapter 6 summarizes and concludes the work done in this thesis and makes recommendation for future work.

CHAPTER 2

LITERATURE REVIEW

In this chapter, historical background of regenerative cooling and flow boiling in terms of experiments and simulations are discussed.

2.1 Regenerative Cooling

Pioneering works on the use of regenerative cooling in LREs are as follows;

- 1930: The first regeneratively cooled (oxidizer as coolant) LRE was built by Luigi Crocco. (see Fig. 2.1) (Sutton, 2006).
- 1930-1940: Eugen Sanger independently worked on regenerative cooling for thrust chambers. He used water and propellants as coolant. In 1936, he operated a thrust chamber cooled entirely by propellant in 1936 (Sutton, 2006).
- 1944: The V-2 rocket was the first mass-produced LRE that uses regenerative cooling assisted by film cooling.

After World War II, LRE development continued mainly in two countries, the USA and USSR. Unfortunately, access to USSR/Russian efforts is almost non-existent. The USSR literature is almost entirely in Russian and it is difficult to understand the chronological development due to the limited references to the USSR literature. After the second half of 1960s, German/EU and Japan started to develop LREs while China and India showed interest in the field after 1980s.

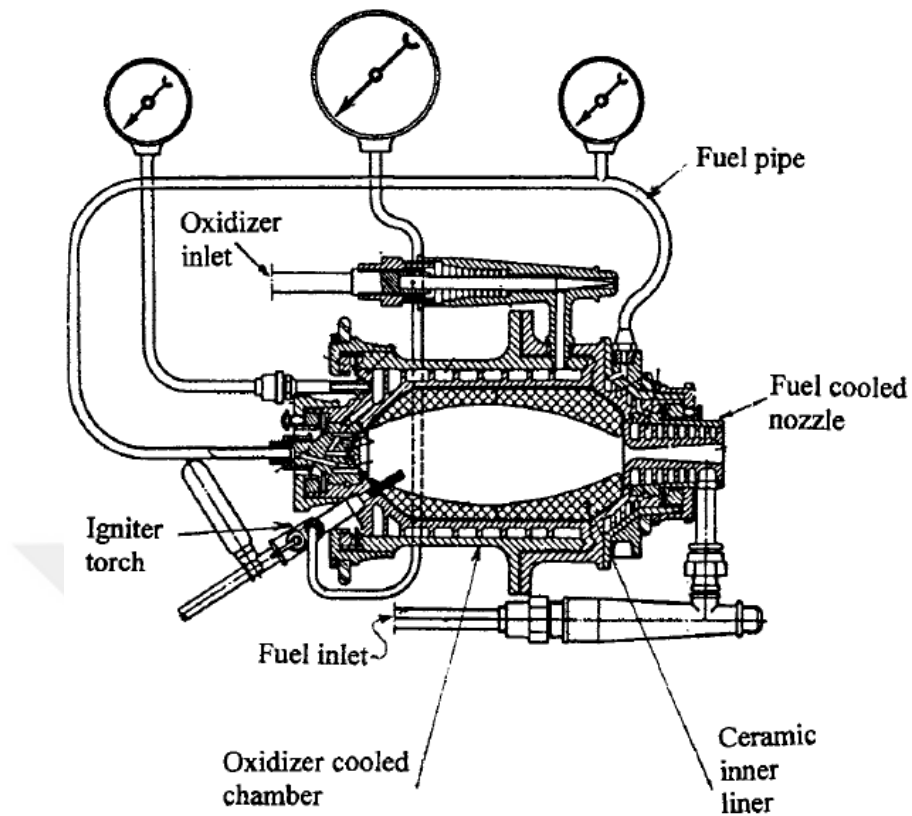


Figure 2.1. First regeneratively cooled thrust chamber (Crocco, 1967)

Most of the experimental efforts in 1950s and 1960s were directed towards finding Nusselt correlations or convective heat transfer coefficients for the hot gas and coolant sides. The most widely used hot gas side correlations were introduced in 1957 by Bartz (1957) and 1960 by Cinjarew (Froehlich, Popp, Schmidt & Thelemann, 1993). For the coolant side, pipe flow correlations (Sieder & Tate, 1936) were adapted. But later, studies were conducted to determine correlations, specifically for rocket propellants and LRE cooling channel geometries (Taylor, 1970; McCarthy & Wolf, 1960). Burnout (onset of film boiling) information has been studied in experiments by NASA for common LRE propellants (Huff & Fairchild, 1972). In these experiments, circular tubes are heated until failure while the heat load is measured. Starting from early 1970s, the heat transfer from the hot gas to the coolant has been modeled numerically. The first models used experimentally determined correlations for hot gas-to-solid and solid-to-coolant heat

transfers and solved for conduction through a solid wall in 2D. These early models done by Ishimoto and Fink (1971) and Gerstley and Tobin (1975) considered the coolant flow as a 1D bulk motion. Such approximations gave fair enough results and were used until late 1980s because of insufficiency of computational sources. In 1988, Naraghi (Naraghi, 2002) published the first version of Rocket Thermal Evaluation (RTE) program using a quasi-3D approach. The idea was similar to the previous work, i.e. the engine is divided into stations and the program repeatedly sweeps all the stations until convergence is achieved. Figure 2.2 shows an example result of the temperature distribution around the cooling channel obtained by the RTE program. The RTE code coupled with TDK (Two-Dimensional Kinetics code for hot gas side heat transfer) is still in use at NASA.

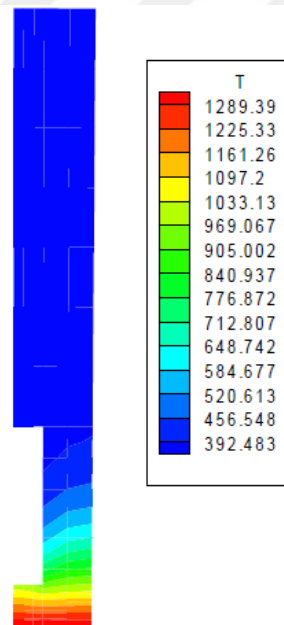


Figure 2.2. A sample 2D temperature distribution on a cross section of a LRE wall (Naraghi, 2002)

After high aspect ratio cooling channels (HARCC) (height/width of the channel > 4 , (Boysan & Ulas, 2013)), which are superior to low ratio ones, started to be produced, the assumption of bulk fluid motion became insufficient. With HARCC, secondary

flow and stratified flow phenomena gained importance. The first 3D CFD simulation for regenerative cooling channels was done by Froelich et. al in 1991 (Froelich, Immich, Lebail, Popp & Scheuerer, 1991). In this study, a code developed by Deutsche Aerospace solved Reynolds-Averaged Navier-Stokes (RANS) equations with the $k-\varepsilon$ turbulence model. The coolant H_2 was in the supercritical phase and the aspect ratio of the channel was between 4.62 and 8.46. The solution at the channel exit (just before the injector) is shown in Fig. 2.3. It was found that there was flow stratification at the end of channels, which was also seen in the experiments. This study was followed by Yagley, Feng and Merkle (1993), Parris and Landrum (2005), Torres, Stefanini and Suslov (2009) and Wennerberg, Jung, Schuff, Anderson and Merkle (2006). During the same period, experimental studies for HARCC also became popular (Carlile & Quentmeyer, 1992).

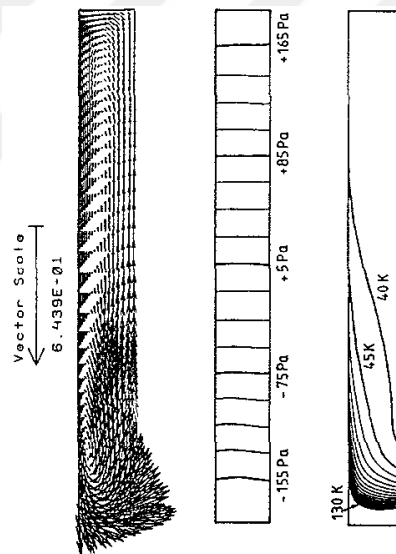


Figure 2.3. A sample result from 3D regenerative cooling channel simulation (from left to right, velocity vector, pressure, temperature distribution of the coolant) (Froelich et al., 1991)

With the spread and development of commercial CFD software, researchers have performed 3D simulations (Parris & Landrum, 2005; Kang & Sun, 2011; Boysan &

Ulas, 2013; Pizzarelli, 2007). Parris and Landrum (2005) studied flows with turns for different aspect ratios from 1.5 to 10 with supercritical H₂ as the coolant. Kang and Sun (2011) coupled hot gas side with the coolant (supercritical H₂) side and solved a 0.6° slice of the full geometry in the circumferential direction. Boysan and Ulas (2013) used the Bartz correlation for the hot gas side and focused on the cooling channel flow. They investigated the effects of the number of channels and their aspect ratio (see Fig. 2.4). One of the important details of this study was the choice of coolant. Unlike many other studies, not only supercritical H₂ but also RP-1 (Rocket Propellant-1, Kerosene) was considered.

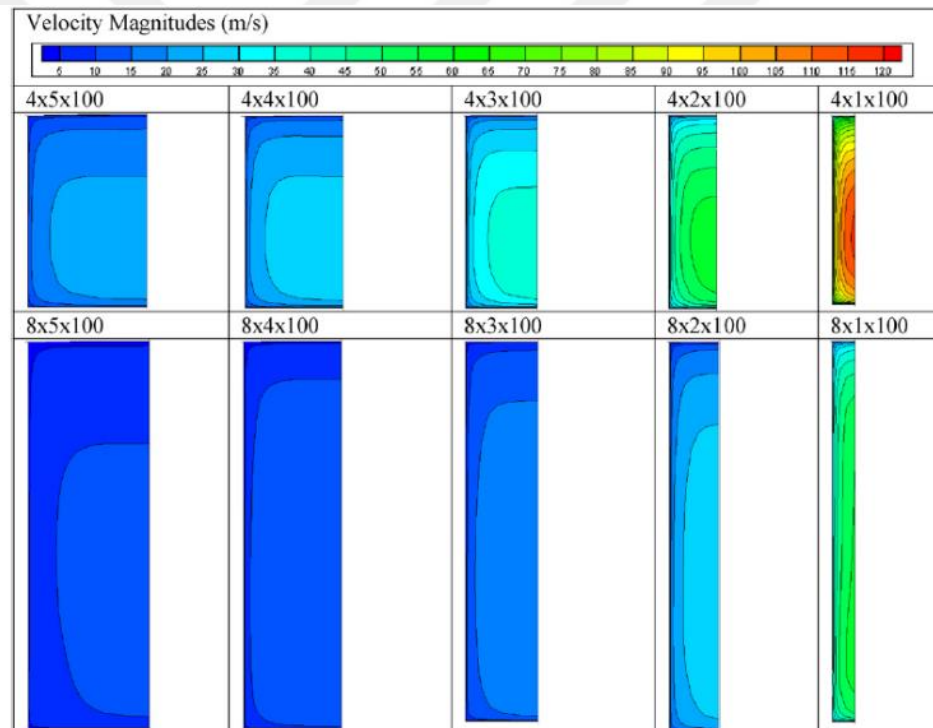


Figure 2.4. Velocity profiles of coolant for different channel aspect ratios (Boysan, 2008)

Beside researchers using of commercial CFD software, others like Pizzarelli (Pizzarelli, 2007; Pizzarelli, Nasuti & Onofri, 2012) have developed their own codes

for regenerative cooling channel analyses. In their studies, they investigated the performance of transcritical and supercritical methane as coolant.

Torres and Desmet (2008) and Meyer (1995) investigated the heat transfer in regenerative cooling by focusing only on a single channel. Torres (Torres & Desmet, 2008) used “thermal nozzle” approach. In this method, the heat fluxes of the actual nozzle are supplied to a single regenerative cooling channel by multiple cartridge heaters. As can be seen in Fig. 2.5, the cross-section of the test specimen grows across the heaters in order to reach required heat flux values. Meyer (1995) used simply electrically heated tubes, but this method does not allow for variable heat flux through the tube. There is no experimental work on flow boiling in regenerative cooling channels in the open literature.

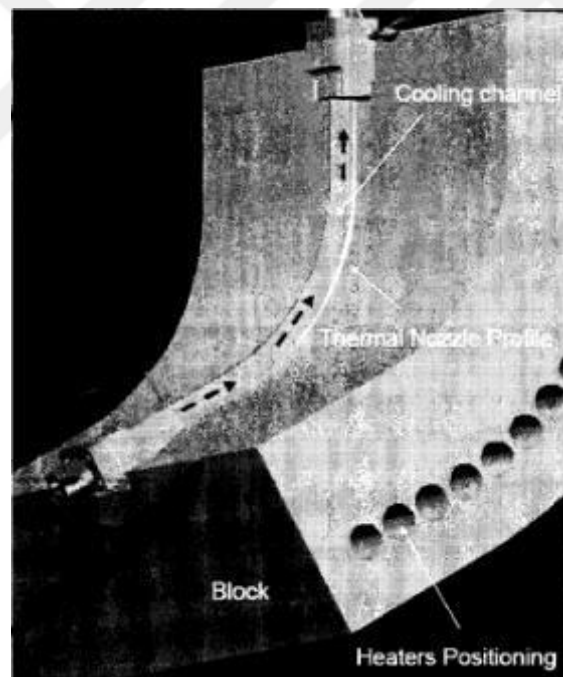


Figure 2.5. Thermal nozzle test specimen (Torres & Desmet, 2008)

2.2 Modeling of Boiling

Numerical modeling studies of boiling started in 1990s and have accelerated in the last 20 years. Table 2.1 summarizes the work of the major numerical simulation research groups interested in boiling. None of these have worked on LRE applications.

The studies of Stephan (Stephen & Hammer, 1994), Son and Dhir (1997), Juric and Tryggvason (Juric & Tryggvason, 1998) and Welch (1998) are the pioneers of numerical simulation of boiling flows. Nearly all groups followed the same steps, starting from 2D single bubble simulations to 3D multi-bubble simulations in complex geometries (Kunkelmann, Stephan & Jakirlic, 2011; Esmareli & Tryggvason, 2004a; Son & Dhir, 2007). However, single bubble simulations have sometimes been revisited (Li & Dhir, 2007) in order to investigate the effect of specific properties such as the contact angle (Mukherjee & Kandlikar, 2007).

For capturing the interface of two phases, Tryggvason and his group used the front tracking technique, which is very accurate in terms of curvature calculations, which is important for the simulation of small bubbles. They worked on film boiling extensively (Juric & Tryggvason, 1998; Esmareli & Tryggvason, 2004a, 2004b, 2004c; Tryggvason, 2001). The first 3D boiling simulation was performed by them in 2001 (Tryggvason et al., 2001). They didn't consider 3-phase contact line known as the microlayer, but this has little impact on film boiling.

Dhir and his group mainly used the level set method (LSM) to capture the interface. His group has done the most extensive work from single bubble (Li & Dhir, 2007; Wu & Dhir, 2007; Son, Dhir & Ramanujapu, 1999) to bubble mergers (Mukherjee & Dhir, 2004), from film boiling (Son & Dhir, 1997, 2007) to nucleate boiling (Son & Dhir, 2008; Wu, Dhir & Qian, 2007) and even nucleate flow boiling (Li & Dhir, 2007). Their models also account for microlayer heat transfer.

Table 2.1. Comparison of existing numerical simulation of boiling studies

Group	Type of Boiling	Interface Capturing Method	Micro-layer Treat.	3D Sim.
<u>G. Tryggvason</u> (Juric & Tryggvason, 1998; Esmaeeli & Tryggvason, 2004a, 2004b, 2004c; Tryggvason et al., 2001)	Film Boiling	Front Tracking	No	Yes
<u>V.K. Dhir</u> (Dhir, 1998, 2001; Son & Dhir, 1997, 2008; Mukherjee & Dhir, 2004; Wu, Dhir & Qian, 2007; Dhir, Warriar & Aktinol, 2013; Wu & Dhir, 2007)	Nucleate Boiling, Film Boiling	Level Set Method, LSM + Ghost Fluid, LSM + Moving Mesh	Yes	Yes
<u>P. Stephan</u> (Stephan & Hammer, 1994; Kunkelmann et al., 2011; Kern & Stephan, 2003a, 2003b; Fuchs, Kern & Stephan, 2006)	Nucleate Boiling	Moving Mesh, Volume of Fluid	Yes	Yes
<u>S.W.J. Welch</u> (Welch, 1998; Welch & Wilson, 2000; Welch & Rachidi, 2002)	Film Boiling	Moving Mesh, Volume of Fluid	No	No
<u>Mukherjee & Kandlikar</u> (Mukherjee & Kandlikar, 2005, 2007; Mukherjee, Kandlikar & Edel, 2011)	Nucleate Boiling, Flow Boiling	Level Set Method	Yes	Yes

After 2004, Mukherjee, one of Dhir's coworkers, started to work with Kandlikar who is a famous figure in experimental boiling studies. They worked on the model developed by Mukherjee and Dhir (2004) and studied microchannel flow boiling (Mukherjee & Kandlikar, 2005; Mukherjee et al., 2011).

Stephan and his colleagues have both numerical (Stephan & Hammer, 1994; Kern & Stephan, 2003b; Fuchs et al., 2006) and analytical (Kern & Stephan, 2003b) work related to nucleate boiling. They developed a finite element model with a moving mesh approach. However, later, they adopted OpenFOAM ("OpenFOAM", n.d.) which is an open source CFD code based on the finite volume method (FVM) and makes use of the volume of fluid (VOF) technique for interface capturing. Welch also used the moving mesh method in his early work (Welch, 1998). But then they switched to VOF and worked on film boiling with conjugate heat transfer.

The noticeable difference between the post-2010 studies compared to the previous literature is the diversity of the studies and researchers. With the help of increasing computational power and knowledge over the years, a wider community started to work on boiling simulations. Contrary to previous works, over the past decade, most of the new studies use already developed codes like ANSYS Fluent and OpenFOAM. On the other hand, solving boiling problems with Lattice Boltzmann Methods has also become popular, especially after 2010. Numerical simulation of condensation which is not much seen in previous works because it is not involved in pool boiling where the vapor leaves from the top of the domain, is being studied in order to completely understand subcooled nucleate boiling and flow boiling. Flow boiling is another hot topic, especially in micro channels. Some of the fundamental researches about nucleate boiling, such as numerical simulation of microlayer region, is ongoing in recent studies. Also, all of the know-how on numerical simulation of boiling has paid off and some real-life applications have been solved, like cooling of internal combustion engine (Punekar & Das, 2013; E, Zhang, Tu, Zuo, Hu, Han & Jin, 2018) and power electronics device (Pettersen, 2014).

This literature review shows that

- other than Ulas and Boysan (2013), all CFD studies used cryogenic coolants (H_2 and methane). The possible reason behind this is that cryogenic fuels are used mostly in civilian rockets such as launch vehicles. There is a huge gap in the literature on simulation of cooling performance of storable fuels like unsymmetrical dimethylhydrazine (UDMH), Monomethylhydrazine (MMH), RP-1 etc.
- all CFD studies given above deal with coolants at high pressure resulting in supercritical fluids. There is no boiling or condensation physics for a supercritical fluid. For pressure-fed systems, the chamber pressures are much lower compared to pump-fed systems (usually between 10 to 20 bar for pressure-fed and more than 60 bar for pump-fed) so the coolant is in liquid phase with possibility of boiling. In this case, as mentioned before, only burnout heat flux values have been determined by NASA studies (Huff & Fairchild, 1972). Detailed nucleate boiling studies for LRE propellants is another gap seen in the literature for LRE regenerative cooling.
- flow boiling studies in the literature have concentrated on microchannels, but the cooling channels of LREs are not microchannel. The geometries of the cooling channels are on the order of millimeters, while the microchannels are on the order of 10 to 100 micrometers.

2.3 Experimental Studies on Flow Boiling

The flow boiling phenomenon has been studied with experimental methods for years. Lin, Kew and Cornwell (2001) published a study on the experimental investigation of flow boiling on several sizes of circular and rectangular tubes. Qu and Mudawar studied the effects of flow boiling on microchannels in terms of flow instability and pressure drop (Qu & Mudawar, 2002b). Another study carried out by Qu and Mudawar on the microchannels showed that boiling incipience heat flux becomes higher when the channel becomes smaller (Qu & Mudawar, 2002a). They also

revealed that for channels smaller than the conventional ones, nucleated bubbles can grow to channel size contrary to bigger channels where the bubbles nucleate, grow, and collapse. Another study on the characterization of flow boiling was conducted by Steinke and Kandlikar (2004). In the same year, Wen, Yan and Kenning (2004) investigated the saturated flow boiling of water in a rectangular channel and found correlations that can be used to calculate the heat transfer coefficient. Liu, Lee and Garimella (2005) developed an analytical model in order to predict the onset of nucleate boiling in a microchannel using experimental data they obtained. Figure 2.6 shows one of their test results obtained with high-speed camera, which captures the evolution of the bubble from nucleation to departure.

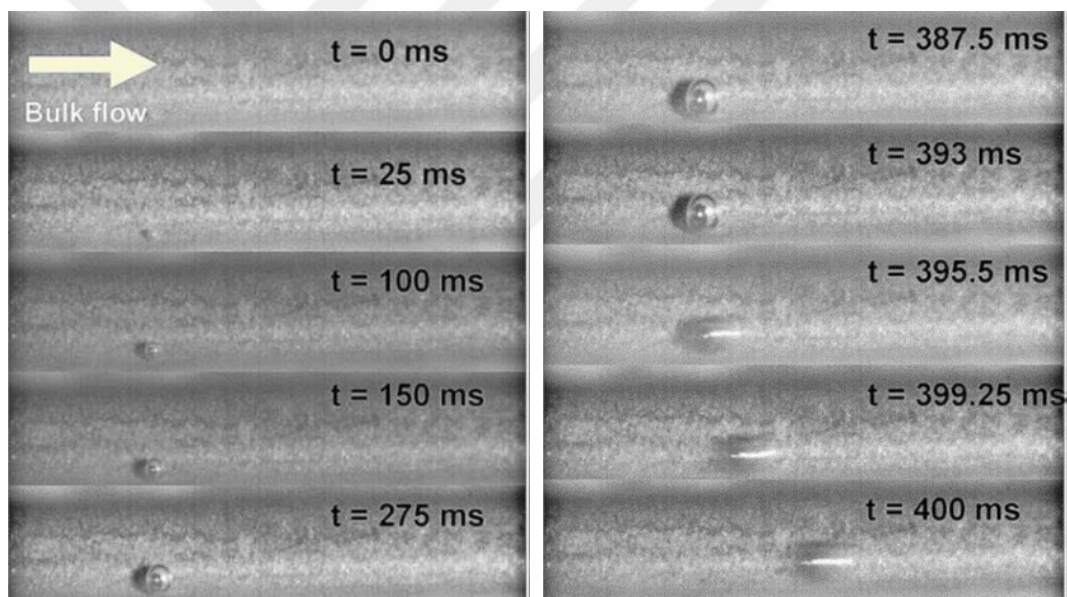


Figure 2.6. Nucleate boiling process in a microchannel retrieved from the study of Liu, Lee and Garimella (2005)

Chen, Tian and Karayiannis (2006) investigated the effects of channel diameter on the boiling phenomena, visually. Yang, Peng and Ye (2008) studied the flow boiling along a coiled circular channel both experimentally and numerically. Zou used a large square channel of 12.7 mm × 12.7 mm to investigate the effects of thermal conductivities on subcooled flow boiling (Zou, 2011). In 2011, flow boiling in

mini/microchannels was studied in order to investigate the effects of multichannel on the heat transfer coefficient by Liu, Weng and Xu (2011). Galvis and Culham (2012) focused on the heat transfer and pressure drop characteristics in different boiling regimes with two different rectangular microchannels whose areas are $0.198 \text{ mm} \times 0.241 \text{ mm}$ and $0.378 \text{ mm} \times 0.471 \text{ mm}$ (Galvis & Culham, 2012). Images from the middle section of the channel at different boiling regimes can be seen in Fig. 2.7 which also shows the versions edited with Matlab in order to analyze the flow characteristics better.

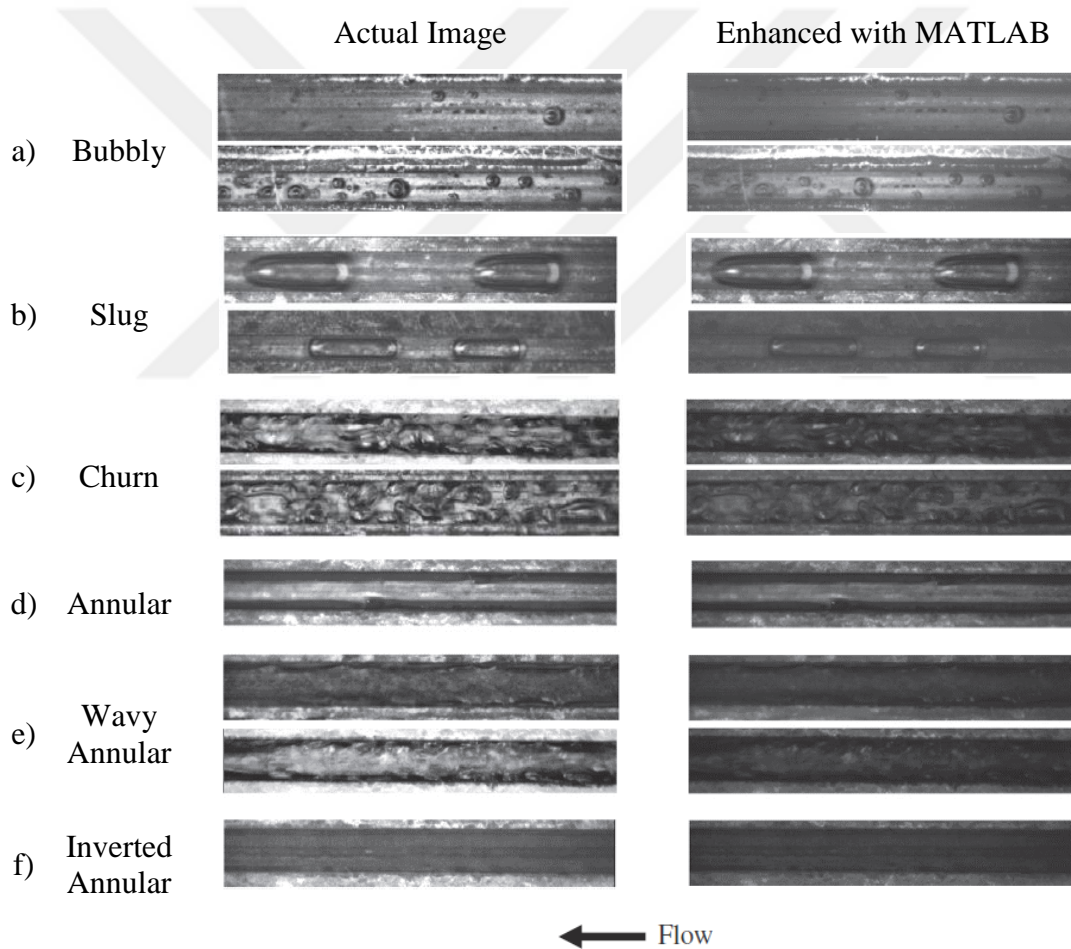


Figure 2.7. Flow patterns taken from the study of Galvis and Gulham (2012)

Yang, Guo and Liu (2014) studied subcooled vertical upward flow boiling in a narrow channel in terms of the onset of nucleate boiling, active nucleation site

density, bubble departure size and frequency. To analyze the effects of geometry, in 2016, another study on flow boiling was conducted by Özdemir by using different rectangular metallic microchannels with widths of 0.39 mm, 0.34 mm, 0.84 mm and heights of 1 mm, 1.68 mm and 0.42 mm, respectively (Özdemir, 2016). Later, Özdemir, Mahmoud and Karayiannis (2020) compared experimental data with analytical models. Diani, Mancin, Balcon, Savio and Rossetto (2017) used a channel of 10 mm × 20 mm in their experiments in order to investigate heat transfer in the flow boiling regime. Visual investigation on flow boiling of deionized water along the channel was done by Huang, Jia, Dang and Yang (2018) to identify flow regime transitions.



CHAPTER 3

EXPERIMENTAL STUDY

This chapter reports the results of a series of experiments performed on the regenerative cooling channel test rig developed at Roketsan Inc. The tests were conducted on a straight cooling channel using water as the coolant.

3.1 Test Setup

In order to verify the solvers developed within the scope of this thesis, a test setup was designed and then the basic requirements of the components detailed below were determined and procured. After that, the feeding system was installed and hydraulic characterization tests were carried out to determine the pressure losses. In addition, a test specimen including a cooling channel was designed, analyzed, manufactured and used in the tests. Details of the feeding system and the test specimen are discussed in this section.

3.1.1 Feeding System

The piping and instrumentation diagram (P&ID) of the test rig is given in Fig. 3.1. Industrial nitrogen tanks are used for pressurization. The fuel and storage tanks have a volume of 1 gallon (~3.8 liters). This provides test durations of more than 450 seconds for an average water mass flow rate of 8.2 g/s through a cooling channel with a cross-section of 1.5 mm × 2 mm.

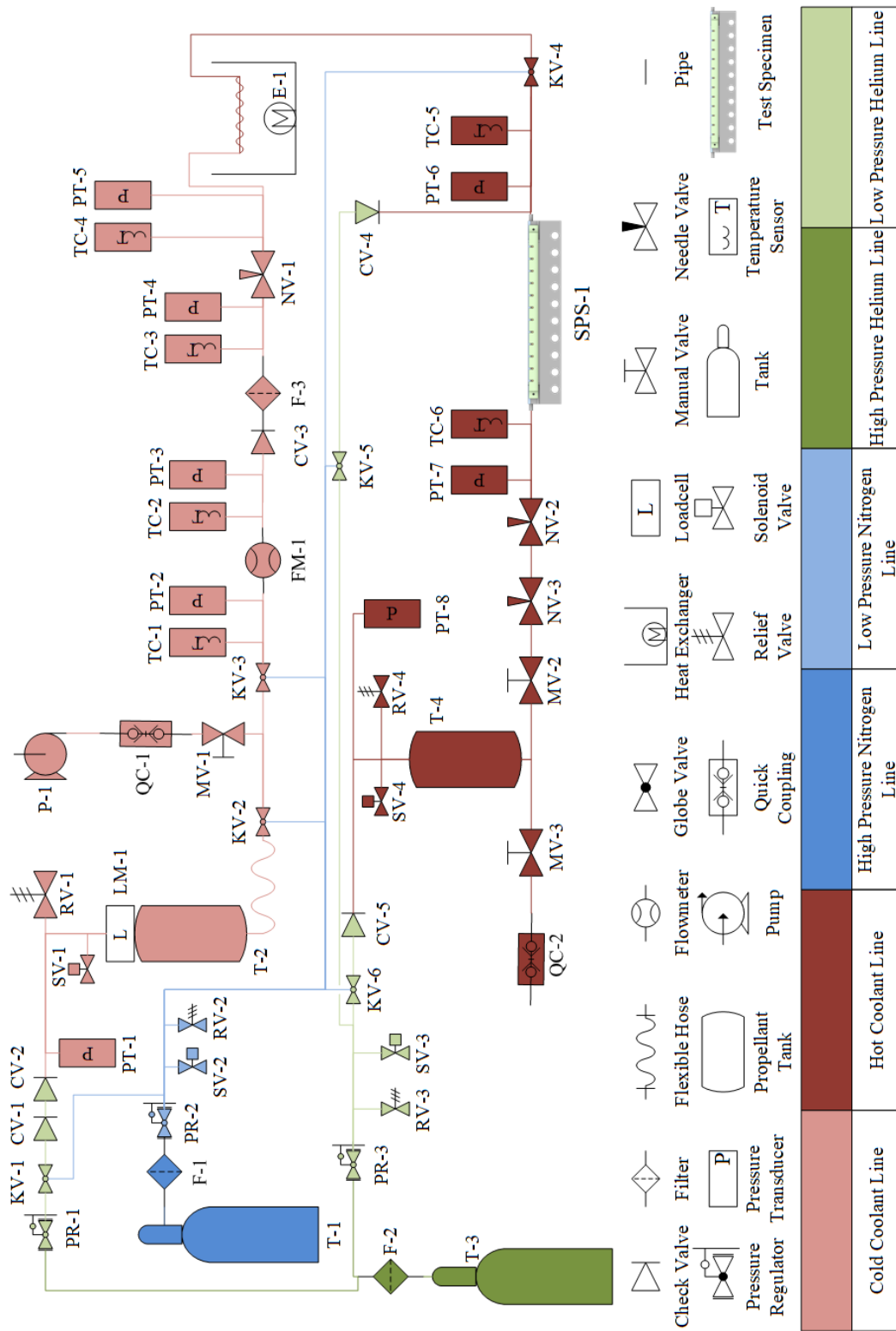


Figure 3.1. Piping and instrumentation diagram of the test setup

The dark and light red lines carry the hot and cold coolant respectively. The coolant is filled into the propellant tank, T-2 via the quick coupling. The pneumatic globe valve is located at the bottom of the propellant tank to isolate it from the rest of the feeding system which includes flow meter, check valve, filter and needle valve.

The heat exchanger is used to heat the coolant and is located close to the inlet of the cooling channel to minimize heat losses through the tubes. Throughout the feeding system, temperature and pressure measurements are taken at various stations, especially at the inlet and outlet of the test sample, to evaluate its performance of the channel.

Another storage tank, T-3 is placed below the channel to store the wasted coolant and also to maintain the channel outlet at the pressure level specified for the test. A manual valve and quick coupling are installed to empty the storage tank. Instead of using a level meter to measure the propellant level in T-2, the propellant tank is hanged on a load cell that measures the mass of the propellant in the tank.

The same type of high-pressure gas tank filled with Nitrogen is used to pressurize both the propellant and the storage tanks. The lines in contact with the pressurizing gas are shown in green in Fig. 3.1. The pressure in the gas tank is reduced to the desired level through a pressure regulator to achieve the mass flow rate of the test being conducted. The second regulator provides the pressure required for the test in the storage tank. Both tanks are separated from the pneumatic part of the system by pneumatic globe valves, while the high-pressure tank and the regulators are protected against coolant backflow by one-way check valves. Relief valves, which open when a certain pressure level is reached, are located above the tanks so that a pressure higher than the design value can be avoided. The blue lines represent the pressure feeding system of the pneumatic globe valves.

The component list of the test setup is given in Table 3.1. In addition, a data acquisition system is used, consisting of three panels and several cables connecting the sensors to the panels. The first panel is used to control the pneumatic and solenoid valves. It also collects data from the pressure transducers and RTD type temperature

sensors. The data acquisition rate of this system is 5 kHz. The second panel is used for the thermocouple measurements of the test specimen. Its data acquisition rate is 100 Hz. The last panel is used to control the heat flux provided by the test specimen cartridges.

The test setup can be seen in Fig. 3.2. Apart from the data acquisition system, the test setup covers an area of 2 m × 2 m. The fluid flow in this figure is in the clockwise direction. The propellant tank is hanged on the right side. The fluid reaches the heat exchanger after passing through two globe valves, a flow meter, filter, needle valve and several pressure transducers and RTDs. In order to obtain the desired fluid temperature at the inlet, the required heat exchanger pipe length is calculated and the pipe with an outer diameter of 1/4" is bent to fit into the heat exchanger cavity. After the heat exchanger, the fluid passes through a globe valve before reaching the test specimen. There is also a purge line in front of the test specimen to clean the wasted coolant after each test. After that, the wasted coolant reaches the storage tank. The storage tank can be pressurized to change the outlet pressure of the test specimen by nitrogen depending on the test requirements.

The test procedure can be summarized as follows:

- First, the test specimen is preheated to 100 °C to reach the steady-state regime faster.
- Next, a regenerative turbine pump, P-1 installed in the feeding system is operated until the temperature differences across the test specimen drop to 0.1 °C for a period of 2 minutes.
- Finally, the regenerative turbine pump, P-1 is switched off and the fluid is fed from the propellant tank.
- The test continues until the coolant in the fuel tank is exhausted to ensure that steady state test condition is reached.

For this test series, the steady state test condition is specified as temperature differences of less than 0.1 °C across the system thermocouples over a 2-min. period.

Table 3.1. Component list of the test setup

Component	Code	Brand	Product Code	Details
Check Valve	CV	Hamlet	H-400-SS-L-1/4-1/3	Crack pressure: 1/3 psi (~0.02 bar)
Filter	F	Hamlet	H-600R-SS-L-1/4-15	Filtration level: 15 μ m
Flowmeter	FM	Omega	FLR1013ST-I	Flow Range: 1– 10 L/min (16.67 – 166.67 ml/s)
Globe Valve	KV	SMS Tork	Tork-PAV 903.SR	-
		Norton	70008302 + SWBOX	-
Heat Exchanger	E	JSR	JSRC-22CL	Adjustable Temperature Range: -40 °C to 120 °C (233 K – 393 K)
Loadcell	LM	ESIT	MSP-40	Range: 0 – 40 kg
Manual Valve	MV	Hamlet	H68-00-SS-L-1/4-PSS	-
Needle Valve	NV	Hamlet	H99-S-00-SS-L-R-1/4	-
Pressure Regulator	PR	BOS	BOS-15420-4	Range: 0 – 40 bar Fluid: Helium
		BOS	BOS-15420-2	Range: 0 – 40 bar Fluid: Nitrogen
Pressure Transducer	PT	Keller	PAA-23SY / 40bar / 81594.55/ PTFE	Range: 0 – 40 bar
Propellant Tank	T-2, T-4	Swagelok	304L-HDF4-1GAL	Volume: 1 gallon (~ 3.79 L)
Quick Coupling	QC	Staubli	HCB 05.1101/IC/JK/6/KB/BM HCB 05.7101/IC/JK/6/KB/BM	-
Regenerative Turbine Pump	P-1	Greenpumps	GPT 202	-
Relief Valve	RV	Hamlet	H-900-HP-SS-L-1/4-B-550psi	Cracking pressure: 550 psi (~ 37.9 bar)
Solenoid Valve	SV	SMS Tork	S6013.02	-
Tank	T-1, T-3	Linde	Helium Tank Nitrogen Tank	- -
Temperature Sensor	TC	Elimko	RT06-2-P-10-05-E1-K10-SS-1/4 NPT	Range: –100°C to 800°C (173K – 1073K)
Test Specimen Cartridges	N/A	Isiform	Ø12.5 x 80 220 V 450 W Watt-Flex Cartridge Heater	Diameter: 12.5 mm Length: 80 mm

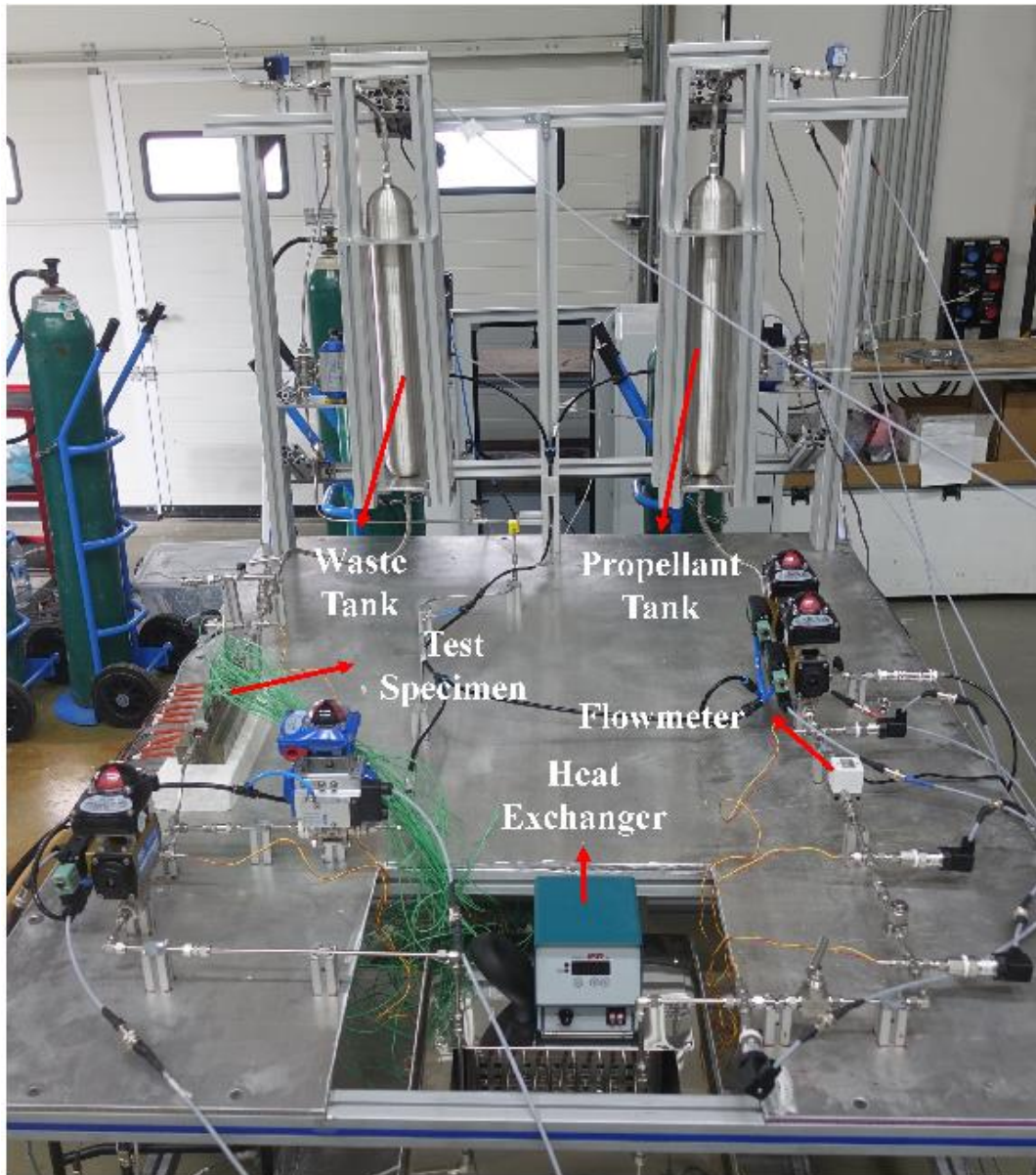


Figure 3.2. Test setup

3.1.2 Test Specimen

A 3D model of the test specimen design and a photograph of the actual manufactured part can be seen in Fig. 3.3.

It is not possible to manufacture a rocket engine with cooling channels from a single piece using conventional methods. In general, the cooling channels are formed on a metal liner that matches the internal contour of the engine and then these channels are sealed by coating them with different methods. The test specimen used in this study was also manufactured in the similar way. First, the test specimen cooling channel, cartridge ports and connection interfaces were conventionally machined on a stainless-steel body. Then, a stainless-steel coating layer was welded over the cooling channel. After welding, the thermocouple ports were machined on the body to obtain accurate temperature measurement positions.

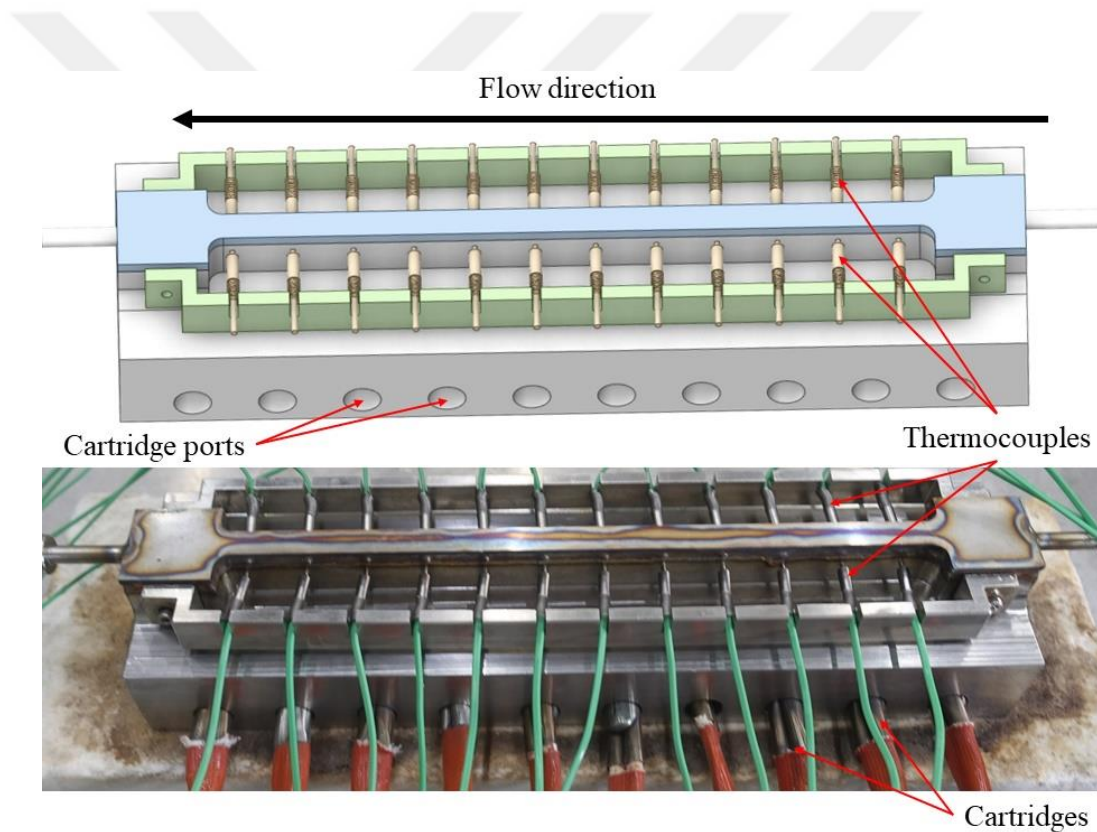


Figure 3.3. 3D model of the test specimen design and a photograph of the actual manufactured part

The test specimen consists of a metal body with a single cooling channel and two thermocouple holders, 24 thermocouples and 10 cartridges. The length of the cooling channel is 30 mm with a cross section of 1.5 mm × 2 mm.

Figure 3.4 shows a top view of the test specimen, showing that 24 thermocouples in 2 groups are installed on both sides of the metal part to determine the onset of boiling.

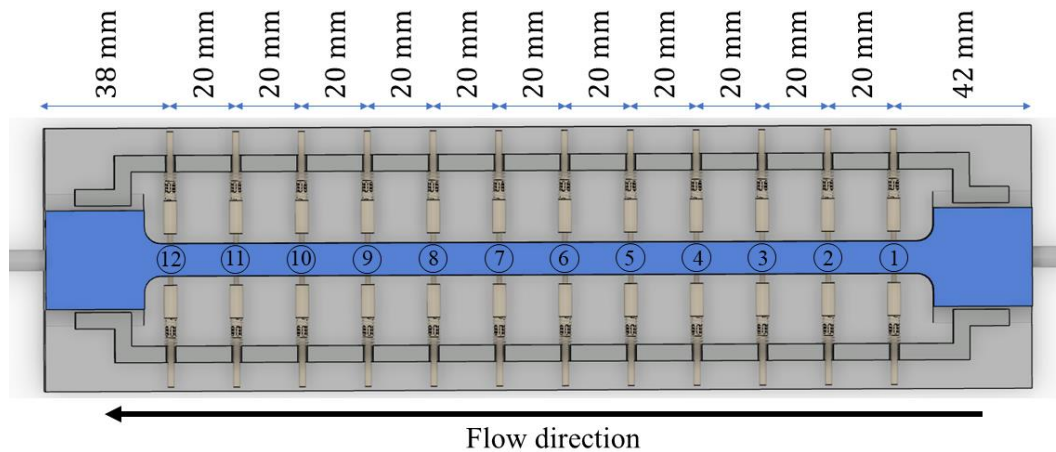


Figure 3.4. Top view showing thermocouple port distances and numbering of stations

As can be seen in the figure, the measuring stations are numbered on the flow direction. The number of stations and their locations were determined by considering manufacturability. The aim of this design is to find the heat flux using the temperature readings from two thermocouples at different depths located under the cooling duct at each station.

The cross-sectional view of the test specimen given in Fig. 3.5 indicates that the thermocouples on both sides are aligned with a certain distance from the center of the cooling channel. The thermocouples on the left side are 1.6 mm lower than the cooling channel, while those on the right side are 2.4 mm lower than the others, making a total of 4 mm with respect to bottom face of the cooling channel.

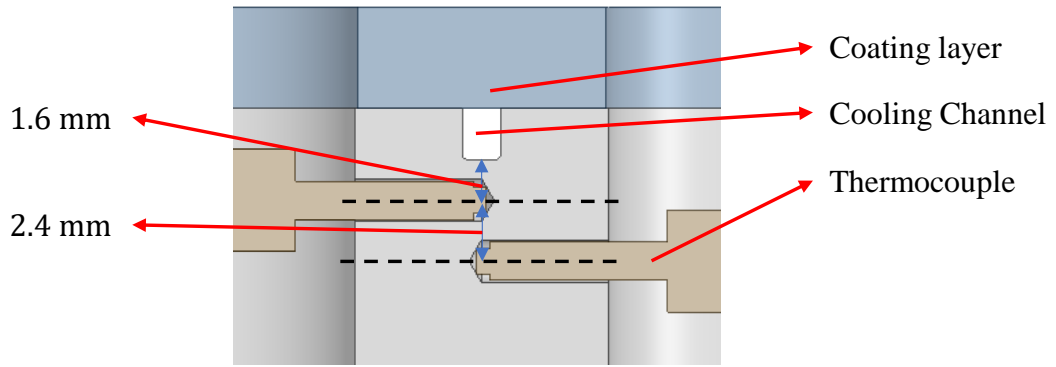


Figure 3.5. Cross-sectional view showing thermocouple port distances

3.2 Uncertainty Analysis

In this part, bias uncertainty of the wall heat flux and convective test heat transfer coefficient are calculated. Random uncertainties are not taken into account. The uncertainty of the pressure sensor used is 0.25% of its full scale, which corresponds to ± 0.1 bar. The uncertainty of the type K thermocouple used is either ± 2.2 °C or 0.75% of the measured temperature values, whichever is greater. In this work, the uncertainty of the temperature measurements is ± 2.2 °C because the highest temperature measurement is much lower than 294 °C. The uncertainty of the flow meter is 1% of its full scale, which corresponds to 0.167 ml/s. All tests were started at the room temperature of 20 °C, where the density of the water is 998.2 kg/m³.

Uncertainty calculations were performed using the error propagation technique described by Kline and McClintock (1953) given in Equation (3.1):

$$\omega_R = \sqrt{\left(\frac{\partial R}{\partial x_1} \omega_{x_1}\right)^2 + \left(\frac{\partial R}{\partial x_2} \omega_{x_2}\right)^2 \dots + \left(\frac{\partial R}{\partial x_n} \omega_{x_n}\right)^2} \quad (3.1)$$

where R is a function of n independent variables, ω_x represents the uncertainty range of independent variables and ω_R shows the overall uncertainty of the R function.

The mass flow rates of the tests performed can be calculated as follows:

$$\dot{m} = \rho \dot{V} \quad (3.2)$$

where \dot{m} , ρ and \dot{V} are mass flow rate, density and measured volumetric flowrate respectively. The uncertainty of the mass flow rate can be formulated as follows:

$$\omega_{\dot{m}} = \sqrt{\left(\frac{\partial \dot{m}}{\partial \rho} \omega_{\rho}\right)^2 + \left(\frac{\partial \dot{m}}{\partial \dot{V}} \omega_{\dot{V}}\right)^2} \quad (3.3)$$

The density of the fluid is a function of temperature and is read from the NIST database, there is no uncertainty. Therefore, the mass flow rate uncertainty becomes:

$$\omega_{\dot{m}} = \sqrt{\left(\frac{\partial \dot{m}}{\partial \dot{V}} \omega_{\dot{V}}\right)^2} \quad (3.4)$$

Equation (3.4) can be simplified as follows:

$$\omega_{\dot{m}} = \rho \omega_{\dot{V}} \quad (3.5)$$

Using $\omega_{\dot{V}} = 0.167$ ml/s, the mass flow rate uncertainty can be calculated as follows:

$$\omega_{\dot{m}} = 998.2 \frac{\text{kg}}{\text{m}^3} \times 0.167 \frac{\text{ml}}{\text{s}} \cong 0.167 \frac{\text{g}}{\text{s}} \quad (3.6)$$

The heat transfer rate on the metal body of the test specimen can be calculated as follows:

$$q'' = -k \frac{\Delta T}{\Delta x} \quad (3.7)$$

where k is the thermal conductivity of the material (calculated using mean temperature of the two thermocouples), ΔT represents the temperature difference between the measurement locations and Δx is the axial distance between the measurement locations. Sample calculation for the heat transfer rate at Station 6 of the Test-9 can be seen below.

$$q'' = -k \frac{\Delta T}{\Delta x} = -17.07 \frac{\text{W}}{\text{mK}} * \frac{422.3 \text{ K} - 485.7 \text{ K}}{0.0024 \text{ m}} = 4.51 \times 10^5 \frac{\text{W}}{\text{m}^2} \quad (3.8)$$

The uncertainty of the heat transfer rate can be found using:

$$\omega_{q''} = \sqrt{\left(\frac{\partial q''}{\partial k} \omega_k\right)^2 + \left(\frac{\partial q''}{\partial \Delta T} \omega_{\Delta T}\right)^2 + \left(\frac{\partial q''}{\partial \Delta x} \omega_{\Delta x}\right)^2} \quad (3.9)$$

Since the thermal conductivity is not a measured quantity but is found from the correlation given in the work of Graves, Kollie, McElroy and Gilchrist (1991) and the uncertainty of the axial distance between two measurement locations is too small, those terms can be cancelled in the uncertainty equation:

$$\omega_{q''} = \sqrt{\left(\frac{\partial q''}{\partial \Delta T} \omega_{\Delta T}\right)^2} \quad (3.10)$$

Equation (3.10) can be rewritten as follows:

$$\omega_{q''} = \sqrt{\left(-k \frac{1}{\Delta x} \omega_{\Delta T}\right)^2} \quad (3.11)$$

and can be arranged as:

$$\omega_{q''} = k \frac{1}{\Delta x} \omega_{\Delta T} \quad (3.12)$$

The highest thermal conductivity used during this test series was 17.07 W/(m · K) at Station 6 of the Test-9. The test conditions can be seen in Table 3.2. The distance between two thermocouples at each station was constant and equals 0.0024 m. Hence, the highest uncertainty of the heat transfer rate calculations can be found as follows:

$$\omega_{q''} = \left(17.07 \frac{\text{W}}{\text{mK}}\right) \cdot \left(\frac{1}{0.0024 \text{ m}}\right) \cdot (2.2 \text{ K}) \cong 15.7 \times 10^3 \frac{\text{W}}{\text{m}^2} \quad (3.13)$$

This corresponds to 3.5% of the calculated heat transfer rate, which shows that the maximum uncertainty of the heat transfer rates found in this test series is less than 5%.

The convective test heat transfer coefficient calculated at each station, h_{test} can be calculated as follows:

$$h_{test} = \frac{q''L}{(2 \cdot ch \cdot \eta + cw)\Delta T} \quad (3.14)$$

where L is the total width under the cooling channel (10 mm) where the heat flux is applied, ch and cw are the cooling channel height and width, η is the fin efficiency used as a constant value of 0.3. The fin efficiency is low compared to common practices because the fin thickness ($L - cw = 8.5$ mm) is comparable to fin width (20 mm). ΔT is the temperature difference between the bottom wall of the cooling channel and the coolant temperature at the specified station. Sample calculation for the heat transfer coefficient at Station 6 of the Test-9 can be seen below.

$$\begin{aligned} h_{test} &= \frac{q''L}{(2 \cdot ch \cdot \eta + cw)\Delta T} \\ &= \frac{4.51 \times 10^5 \frac{\text{W}}{\text{m}^2} \cdot 0.1 \text{ m}}{(2 \cdot 0.002 \text{ m} \cdot 0.3 + 0.0015 \text{ m}) \cdot (380.1 \text{ K} - 346.9 \text{ K})} \\ &= 4.89 \times 10^4 \frac{\text{W}}{\text{m}^2\text{K}} \end{aligned} \quad (3.15)$$

The uncertainty of the heat transfer coefficient calculation is as follows:

$$\begin{aligned} \omega_{h_{test}} &= \left(\left(\frac{\partial h_{test}}{\partial q''} \omega_{q''} \right)^2 + \left(\frac{\partial h_{test}}{\partial L} \omega_L \right)^2 + \left(\frac{\partial h_{test}}{\partial ch} \omega_{ch} \right)^2 \right. \\ &\quad \left. + \left(\frac{\partial h_{test}}{\partial cw} \omega_{cw} \right)^2 + \left(\frac{\partial h_{test}}{\partial \Delta T} \omega_{\Delta T} \right)^2 \right)^{0.5} \end{aligned} \quad (3.16)$$

Assuming the negligible uncertainty in the L , cw and ch measurements, the above equation can be simplified into the following:

$$\begin{aligned}\omega_{h_{test}} &= \sqrt{\left(\frac{\partial h_{test}}{\partial q''} \omega_{q''}\right)^2 + \left(\frac{\partial h_{test}}{\partial \Delta T} \omega_{\Delta T}\right)^2} \\ &= \sqrt{\left(\frac{L}{(2 \cdot ch \cdot \eta + cw)\Delta T} \omega_{q''}\right)^2 + \left(\frac{-q''L}{(2 \cdot ch \cdot \eta + cw)\Delta T^2} \omega_{\Delta T}\right)^2}\end{aligned}\quad (3.17)$$

which can be reformulated like this:

$$\omega_{h_{test}} = \frac{L}{(2 \cdot ch \cdot \eta + cw)\Delta T} \sqrt{\omega_{q''}^2 + \frac{q''^2}{\Delta T^2} \omega_{\Delta T}^2} \quad (3.18)$$

When maximum heat transfer coefficient rate conditions are applied to the equation, the uncertainty becomes:

$$\begin{aligned}\omega_{h_{test}} &= \frac{0.01 \text{ m}}{(2 \cdot 0.002 \text{ m} \cdot 0.3 + 0.0015 \text{ m}) \cdot (33.13 \text{ K})} \\ &\quad \times \sqrt{\left(15.7 \times 10^3 \frac{\text{W}}{\text{m}^2}\right)^2 + \frac{\left(4.51 \times 10^5 \frac{\text{W}}{\text{m}^2}\right)^2}{(33.13 \text{ K})^2} (2.2 \text{ K})^2} \\ &\cong 3664 \frac{\text{W}}{\text{m}^2\text{K}}\end{aligned}\quad (3.19)$$

This corresponds to 7.5% of the calculated heat transfer coefficient at Station 6 of Test-9, which means that the maximum uncertainty of the heat transfer coefficients calculated in this test series is less than 10% for each result given in the following sections.

3.3 Test Matrix

The purpose of this series of tests is to investigate the effect of heat input on the coolant temperature distribution and to use it to infer the boiling of the coolant. Apart from the heat input, the mass flow rate of the coolant and inlet coolant temperature are controllable parameters and are kept almost constant around 8.2 g/s and 59 °C respectively.

Test matrix is given in Table 3.2. The working fluid in these tests was water. The heat input was adjusted by controlling the heater voltage through the test control program and given as the heater input rate here.

Since the heat lost to the environment varies with each test, there was no linear relationship between the power supplied to the heaters and the power supplied to the test specimen. For this reason, the power inputs to the heater were not shared. The heat transfer rate to the cooling channel was calculated with Equation (3.7) by using the temperature readings at each station.

Table 3.2. Test matrix with water being the coolant

No	Heater Input Rate (%)	\dot{m} (g/s)	T_{inlet} (°C)	V (m/s)	Re
1	25	8.23	59.9	2.79	11506
2	28	8.19	58.8	2.78	11456
3	30	8.18	58.5	2.77	11437
4	33	8.15	59.1	2.76	11395
5	35	8.21	58.7	2.78	11479
6	38	8.15	59.2	2.76	11388
7	40	8.14	58.8	2.76	11381
8	43	8.14	59.3	2.76	11382
9	45	8.24	59.6	2.79	11520

3.4 Test Results

Figure 3.6 shows the variation of the wall heat flux with wall superheat. Using data from two thermocouples at different depths at each station, the temperature at the bottom wall of the cooling channel and the heat flux acting at each station were calculated. The figure shows the wall superheat and heat flux values obtained at first 6 stations in 9 tests. During the tests, it was observed that the temperature increase gradient started to decrease after the 6th station and after a while the temperature started to decrease. For this reason, the data after the 6th station in all tests are not

shared in this graph. In the graph, tests are coded with different colors and stations with different signs. Station locations can be seen in Fig. 3.4.

As can be seen from the figure, there is an almost linear trend between temperature and heat flux in the section where the wall temperature is below the saturation temperature. It is also observed that the same heat flux occurs at the same wall temperature regardless of the changes in the test conditions and the station where the measurement was taken. In the region where the wall superheat exceeds 2 °C, a significant increase in the slope of the curve is observed. This trend change indicates that subcooled flow boiling starts around this point. After this point, it is considered that there is two-phase flow in the channel. In this region, the wall heat flux shows a change correlated with the wall temperature. The change of heat flux as a function of wall temperature and the increase in slope after the saturation temperature are similar to results obtained by Liu and Garimella (2007).

The heat transfer coefficient was calculated at each station for all tests by using Equation (3.14). The heat transfer coefficient values calculated by using test data are compared with the correlations in the literature in Fig. 3.7. In the region below the saturation temperature, single-phase Sieder-Tate correlation for circular ducts was applied by using the hydraulic diameter of the rectangular cooling channel. The correlation gives results in agreement with the test data. In the region above the saturation temperature, the single-phase Sieder-Tate correlation given in Equation (1.5) is modified according to the subcooled boiling correlation proposed by Mohammed (1977) as follows:

$$h_{tp} = h_{sp} \left[1 + (\psi_0 - 1) \frac{T_w - T_{sat}}{T_w - T_f} \right] \quad (3.20)$$

where T_f , T_{sat} and T_w stand for coolant temperature, saturation temperature of coolant and wall temperature respectively.

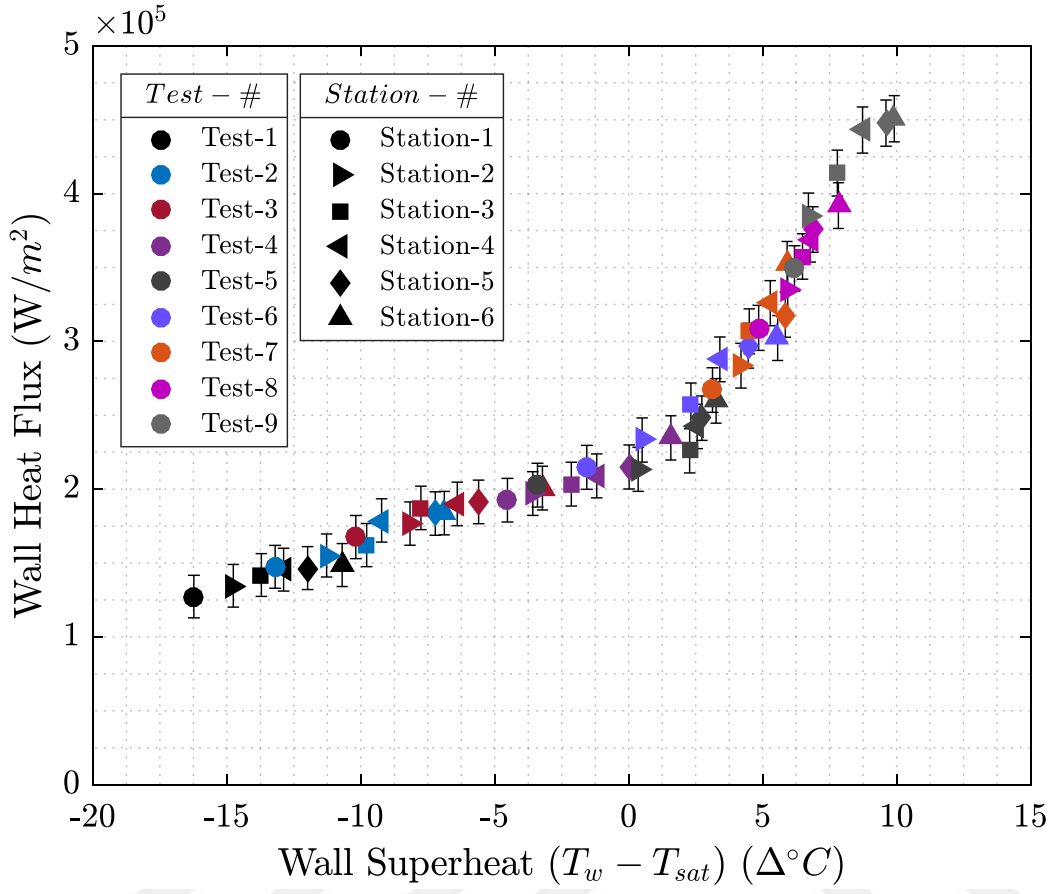


Figure 3.6. Change in wall temperature with respect to heat input (black horizontal lines denotes uncertainty of each wall heat flux value)

ψ_0 is a parameter that is related to saturated boiling with zero subcooling and can be found by using the following equation:

$$\psi_0 = \begin{cases} 230Bo^{0.5} & \text{if } Bo > 3 \times 10^{-5} \\ 1 + 46Bo^{0.5} & \text{else} \end{cases} \quad (3.21)$$

where Bo is the boiling number calculated as follows:

$$Bo = \frac{q_w''}{Gh_{fg}} \quad (3.22)$$

with q_w'' , G and h_{fg} being the wall heat flux, mass flux and latent heat respectively.

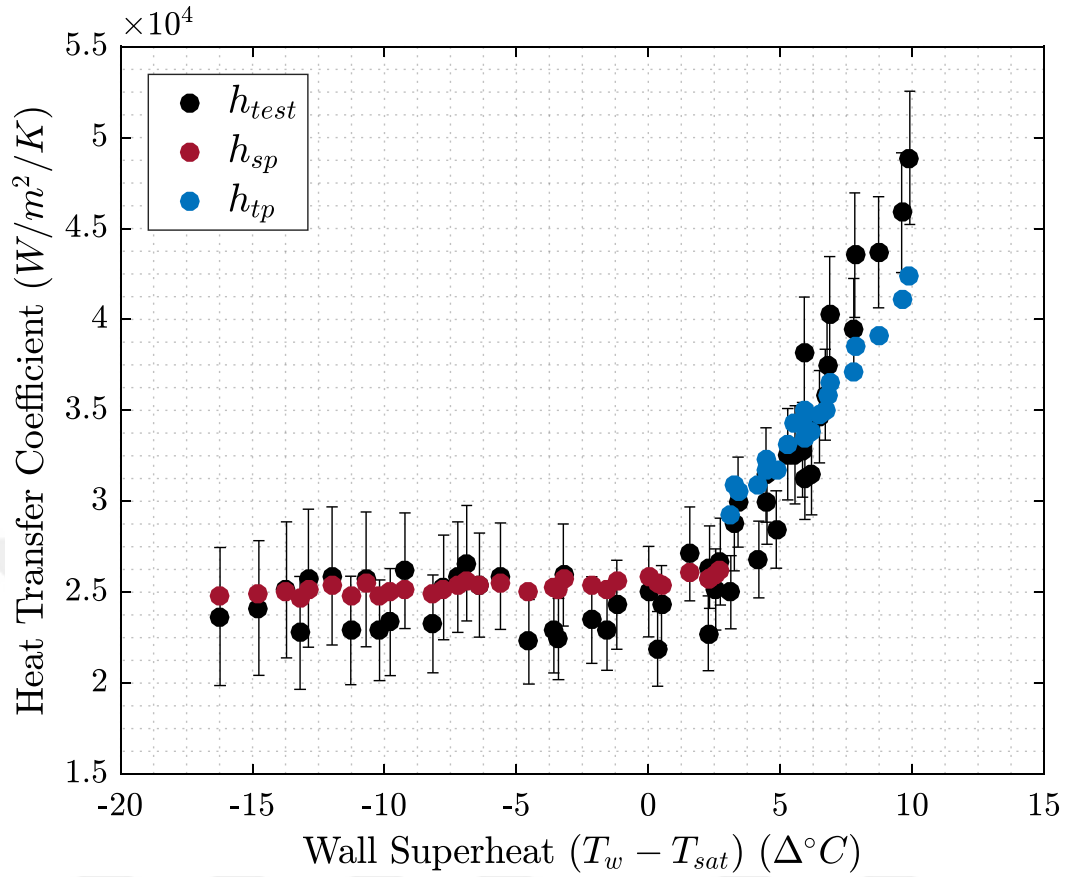


Figure 3.7. Change in heat transfer coefficient with respect to wall superheat (black horizontal lines denotes uncertainty of each value)

An average error for model heat transfer coefficient values predictions with respect to test values was calculated by using the formulation defined in the study of Liu & Garimella (2007).

$$MAE = \left(\frac{1}{N}\right) \sum \frac{|h_{test} - h_{pred}|}{h_{test}} \quad (3.23)$$

Here, MAE is the mean absolute error, N is the total test number of test points, h_{test} is the calculated heat transfer rates using experimental data and h_{pred} denotes the predicted heat transfer rates (h_{sp} and h_{tp}). In this study, Equation (1.5) and Equation (3.20) are used for theoretical heat transfer rate predictions. As a result, the mean

absolute error and maximum error ($|h_{test} - h_{pred}|/h_{test}$) are found as 6.24% and 17.06% which are considered to be acceptable.

After calculation the error values, by changing the coefficients in the ψ_0 parameter (Equation (3.21)) in Mohammed's equation, it is tried whether a better approximation could be made for the heat transfer coefficient. Under the conditions of present experiments, Bo remained above 3×10^{-5} values, so ψ_0 is calculated as $230Bo^{0.5}$. The ψ_0 values is modelled with a similar equation to original one.

$$\psi_0 = a + b \cdot Bo^c \quad (3.24)$$

By using Matlab's genetic optimization algorithm (The MathWorks Inc. (2016)), a , b , and c are optimized. When the optimized values ($a = 2.8$, $b = 585$, and $c = 1.15$) are used, the mean absolute error and maximum error for heat transfer coefficient are calculated as 6.21% and 16.45%. The new Equation (3.24) resulted in a slight decrease in error compared to the original equation. Since the newly calculated h values are similar to the old ones, Figure 3.7 does not need to be recreated.

The Mohammed's correlation predicts similar results to the test data, especially in the region between $0 - 8$ °C wall superheat. After this point, the correlation predicts slightly lower heat transfer coefficients than the test data. According to Kakaç, Bergles and Fernandes (1988), when the correlations derived for the circular ducts are applied to rectangular ducts, 10 – 15% of error can be seen. This result shows that for the single-phase region Sieder-Tate correlation and for the two-phase region modified Sieder-Tate correlations with Mohammed's equation (The original equation is preferred due to of its broad range of applicability.) can predict the test data with high accuracy and can be used for the design tools of rectangular cooling channels.

CHAPTER 4

ONE- AND TWO-DIMENSIONAL DESIGN TOOLS

The regenerative cooling channel design is mainly based on 4 parameters; liner thickness (t), cooling channel height (ch), cooling channel width (cw) and number of cooling channels (N_{cc}). These parameters are shown in Fig. 4.1. A simpler and faster 1D tool is used to narrow down the solution space for these 4 channel parameters mentioned above.

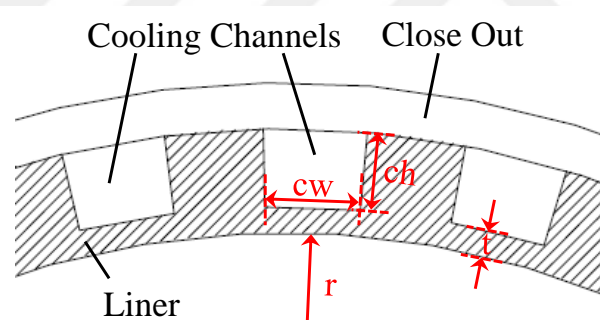


Figure 4.1. Main regenerative cooling channel design parameters

The 2D FDM solver is a thermal analysis code for regeneratively cooled LREs. It is a fast tool (5-10 minutes per run/channel geometry on serial process) and will be used to investigate the channel design. Using the finite difference technique, it solves for heat transfer through the solid part of the engine (liner and close-out) to predict wall temperatures in both radial and circumferential directions. It uses semi-empirical convective heat transfer correlations to determine the heat flux values from hot gas and coolant sides. A similar approach (RTE) was developed by Naraghi (Naraghi, 1987) in late 80s and is still used today as a paid service (Rocket Thermal Evaluation (RTE), n.d.). The functionality of the solver is extended for use in

modeling nucleate boiling for the designs of the current work by locating the subcooled nucleate boiling and varying the heat transfer rates accordingly.

4.1 One Dimensional (1D) Design Tool

The one-dimensional regenerative cooling channel design tool is an analytical tool developed using thermal circuit methodology (Fig. 4.2, left). The LRE is divided into stations in the longitudinal direction and each station is solved individually, starting from the coolant inlet until the coolant leaves the channels (Fig. 4.2, right). A similar tool was created and validated by Naraghi (Naraghi & Foulon, 2008) who also developed the previously mentioned RTE (Rocket Thermal Evaluation) program. In this solver, semi-empirical Nusselt number correlations are used to determine heat transfer rates on both the hot gas and coolant side. The assumptions for this solver are as follows;

- The coolant mass flow rates of all cooling channels are equal.
 - The coolant mass flow distribution is controlled by coolant inlet manifolds. Only a few percent difference among channels is usually allowed in the designs.
- There is no heat diffusion in the longitudinal direction.
 - Even though, neglecting the longitudinal heat conduction through the cooling channel wall produces errors, heat conduction in radial direction is one order of magnitude higher than circumferential and longitudinal directions in most of the LRE's.
- The wall temperature does not change in the circumferential direction in the same cross section.
- The coolant is well mixed, so the bulk coolant temperature is valid for calculations.
 - Bulk coolant approach is mostly utilized method for 1D and 2D models. Caution should be exercised when using in high aspect ratio cooling channels where stratification may occur.

- All of the heat is transferred from hot gases to the engine walls and then from the engine walls to the coolant.
- All of the heat transferred to the coolant comes from the side wall and bottom of the cooling channel.

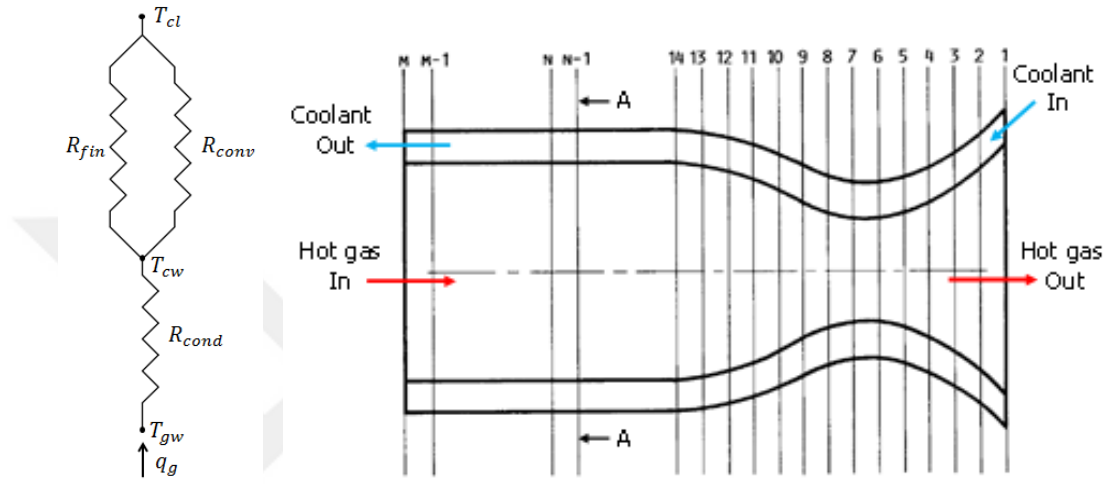


Figure 4.2. 1D design tool; an equivalent thermal resistances (left), an engine subdivided into stations (right) (Naraghi, 2002)

4.1.1 Equivalent Thermal Resistance

As can be seen from Fig. 4.2, there are three main resistances. Equation (4.1) gives the thermal resistance for the liner section due to conduction. Equation (4.2) represents the thermal resistance due to convection at the base of the fin. Finally, the wall between the two cooling channels is considered as fins with adiabatic tips and the thermal resistance can be calculated by Equation (4.3).

$$R_{cond} = \frac{\ln\left(1 + \frac{2t}{D}\right)}{2\pi k_w L} \quad (4.1)$$

where D and L are the inner diameter of the engine at the current station and the length of the channel respectively. k_w is the thermal conductivity of the engine liner.

$$R_{conv} = \frac{1}{h_{cl}cwLN_{cc}} \quad (4.2)$$

Here, N_{cc} is the number of cooling channels and h_{cl} is the convective heat transfer coefficient of the coolant side. The third resistance (R_{fin}) can be found as follows:

$$R_{fin} = \frac{1}{h_{cl}2chL\eta_f N_{cc}} \quad (4.3)$$

where η_f is the fin efficiency calculated using Equation (4.4):

$$\eta_f = \frac{\tanh(mch)}{mch} \quad (4.4)$$

m in Equation (4.4) is found as follows:

$$m = \sqrt{\frac{h_{cl}2(L + \delta)}{k_w L \delta}} \quad (4.5)$$

Here, δ is the fin thickness (i.e. distance between two channels). Since, $L \gg \delta$ (total channel length is much longer than distance between two channels) in Equation (4.5), m can be further simplified as follows:

$$m = \sqrt{\frac{2h_{cl}}{k_w \delta}} \quad (4.6)$$

The equivalent resistance is calculated using Equation (4.7) and the overall thermal resistance between the wall and the coolant is expressed by Equation (4.8).

$$R_{eq} = R_{cond} + \frac{1}{\frac{1}{R_{fin}} + \frac{1}{R_{conv}}} \quad (4.7)$$

$$R_{eq} = \frac{1}{N_{cc}h_{cl}L(2\eta_f ch + cw)} + \frac{\ln\left(1 + \frac{2t}{D}\right)}{2\pi k_w L} \quad (4.8)$$

Once the equivalent wall thermal resistance is obtained, the hot gas side wall temperature at the current station can be determined by Equation (4.9).

$$T_{wg} = T_{cl} + R_{eq}q_g \quad (4.9)$$

4.1.2 Hot Gas Side Heat Transfer

The convective heat flux from the hot gas is calculated using Equation (1.1). The hot gas flow slows down near the wall and consequently heats up. When it reaches the engine wall, the hot gas flow becomes almost stagnant, causing its temperature to increase. At the insulated (adiabatic) wall, the temperature of the hot gas is called adiabatic wall temperature, T_{aw} . The adiabatic wall temperature is not equal to the stagnation temperature because it is not fully recovered in the engine wall. A recovery factor (rf) is used to determine the adiabatic wall temperature. The calculation of T_{aw} and rf is given in Equation (4.10) and (4.11), assuming the hot gas flow is turbulent.

$$T_{aw} = T_c \left[\frac{1 + rf \left(\frac{\gamma - 1}{2} \right) M^2}{1 + \left(\frac{\gamma - 1}{2} \right) M^2} \right] \quad (4.10)$$

$$rf = (Pr_g)^{0.33} \quad (4.11)$$

where T_c is the stagnant combustion chamber temperature. γ and Pr_g are the ratio of the specific heats and Prandtl Number of the hot combustion gases. M is the Mach number in the current cross section.

The convective heat transfer coefficient, h_g , can be determined using the semi-empirical Bartz correlation (Bartz, 1957) developed especially for rocket engines. The Bartz correlation and its correction factor are given in Equation (4.12) and (4.13).

$$h_g = \frac{0.026}{d_t^{0.2}} \left(\frac{\mu_g^{0.2} c_{p,g}}{Pr_g^{0.6}} \right) \left(\frac{P_c}{C^*} \right)^{0.8} \left(\frac{d_t}{R_{tc}} \right)^{0.1} \left(\frac{A_t}{A} \right)^{0.9} \sigma \quad (4.12)$$

$$\sigma = \left[0.5 \frac{T_{wg}}{T_c} \left(1 + \left(\frac{\gamma - 1}{2} \right) M^2 \right) + 0.5 \right]^{-0.68} \left(1 + \left(\frac{\gamma - 1}{2} \right) M^2 \right)^{-0.12} \quad (4.13)$$

where P_c is combustion chamber pressure, C^* is characteristic velocity. d_t and R_{tc} are the diameter and curvature of nozzle throat respectively. A_t and A are the cross-sectional area of the throat and the station considered. It should be noted that the correction factor, σ includes T_{wg} , which requires implicit calculations.

4.1.3 Coolant Side Heat Transfer

The calculation of the coolant side convective heat transfer coefficient uses the well-known Nusselt number correlation, namely Sieder and Tate, as given in Equation (1.5). The Sieder and Tate formulation is used for non-cryogenic coolants such as RP-1 and MMH. The Nusselt correlation (Equations (4.14) - (4.16)) given by Hendricks and coworkers (Hendricks et al., 1986; Kumakawa, Niino, Hendricks, Giarratano & Arp, 1986) is used to calculate the convective heat transfer coefficient between cooling channel wall and cryogenic coolants.

$$\frac{Nu}{Nu_r} = 0.023 Re^{0.8} Pr^{0.4} \quad (4.14)$$

$$Nu_r = \left(1 + \beta(T_{wc} - T_{cl}) \right)^{-0.55} \quad (4.15)$$

$$\beta = \left| \frac{1}{\rho} \frac{\partial \rho}{\partial T} \right| \quad (4.16)$$

The properties required for correlation are taken from the static coolant temperature, T_{cl} and pressure, P_{cl} . T_{wc} is the cooling channel wall temperature.

4.1.4 Verification and Results

To verify the solver, the results from the 1D solver are compared with 3D CFD analysis presented in Boysan's work (Boysan, 2008) and current experimental results.

4.1.4.1 300 kN LOX/RP-1 Engine Cooled by RP-1

For the regenerative cooling channel calculations, Boysan designed a generic LOX/RP-1 engine with 300 kN thrust utilizing RP-1 as coolant. In his study, the effect of aspect ratio (ch/cw), channel height (ch) and number of cooling channels (N_{cc}) were investigated. Chamber geometry, coolant mass flow rate and inlet temperature can be found in his work. Nozzle efficiency is not given. Efficiency values ranging from 85% to 98% have been reported in the literature (Huzel et al., 1992). In order to find the appropriate nozzle efficiency value, wall temperature values are compared for a sample channel design ($ch = 4$ mm, $cw = 4$ mm, and $N_{cc} = 100$). In Fig. 4.3, the wall temperatures for 4 different nozzle efficiency values (from 80% to 95%) are shown. In the vicinity of the throat region, which needs to be taken into consideration due to the high temperature values, temperature values for both 80% and 85% nozzle efficiency are in good agreement with Boysan's results. From then on, between these two values, 85% nozzle efficiency is used because it is the lower limit for nozzle efficiency reported in the literature.

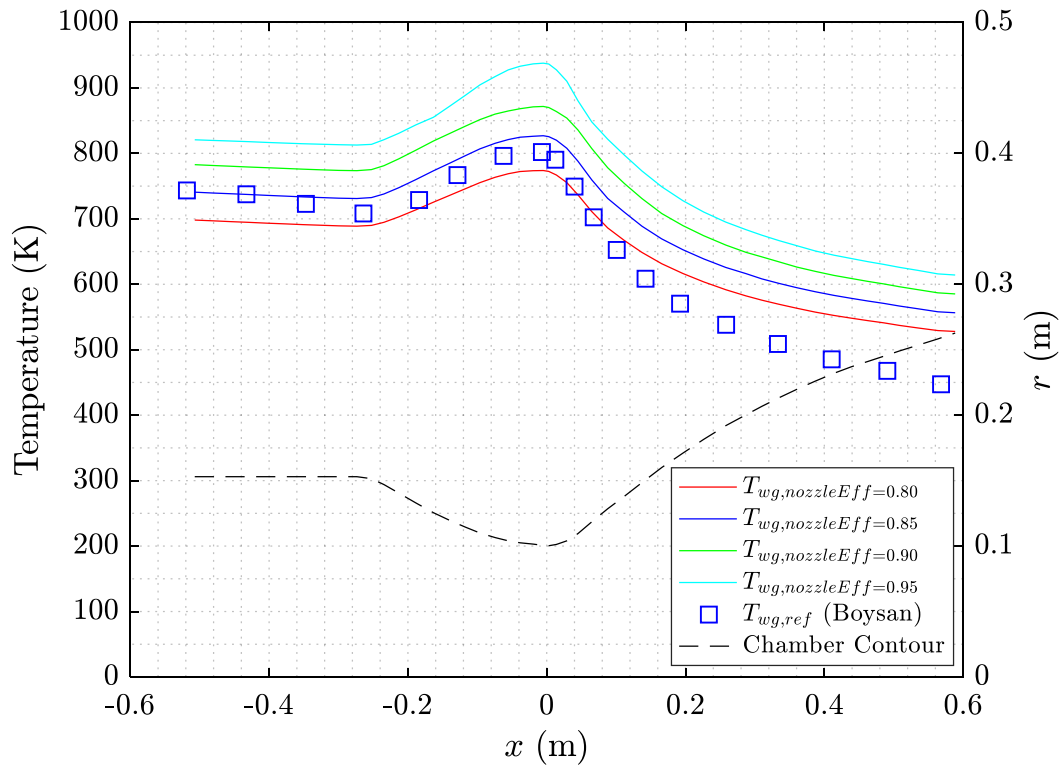


Figure 4.3. Hot gas side wall temperature change along Boysan's engine (Boysan, 2008) for 4 different nozzle efficiency values (channel geometry: $ch = 4$ mm, $cw = 4$ mm, $N_{cc} = 100$)

In order to investigate the effect of channel height and aspect ratio, two different channel height values (4 mm and 8 mm) and 5 different aspect ratio values are investigated. The predictions of the maximum wall temperature values on gas side values are compared and presented in Fig. 4.4. The trends of the results of 1D tool are similar to Boysan's work, but for two cases; $ch = 4$ mm, $ch/cw = 4$ and $ch = 8$ mm, $ch/cw = 8$, the difference is more than 10%. Because of the constant mass flow rate and channel height, an increase in aspect ratio leads to an increase in the Reynolds Number, therefore the Nusselt number ($Re^{0.8}$). This means that lower temperature values are expected with the 1D tool. After that, the newer the Gnielinski correlation (Incropera, 2007) for the Nusselt Number (Equation (4.17)) was also applied, but the results were not any better, so they are not presented.

$$Nu = \frac{(f/8)(Re - 1000)Pr}{1 + 12.7(f/8)^{1/2} (Pr^{2/3} - 1)} \quad (4.17)$$

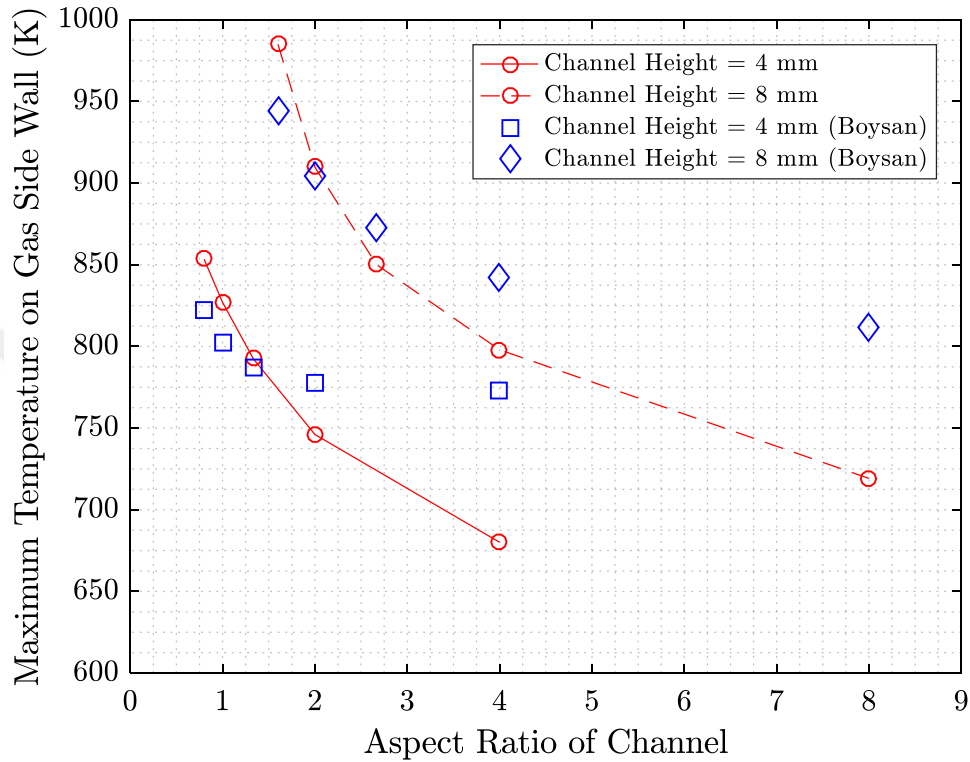


Figure 4.4. Effect of channel height and aspect ratio on maximum gas side wall temperature

The effect of the number of cooling channels on the wall temperature was also examined with $ch = 4$ mm, $cw = 2$ mm channel. In Fig. 4.5, the maximum gas side wall temperatures are compared with Boysan's results for the number of cooling channels between 50 to 300. The trends of the two sets of temperatures are similar. Only for the number of channels 50 the difference between temperature values is greater than 5%. The channel velocity for this case is extremely high (94.8 m/s), similar to the previous discussion. For a coolant like RP-1, it is probably not applicable to a real-life situation.

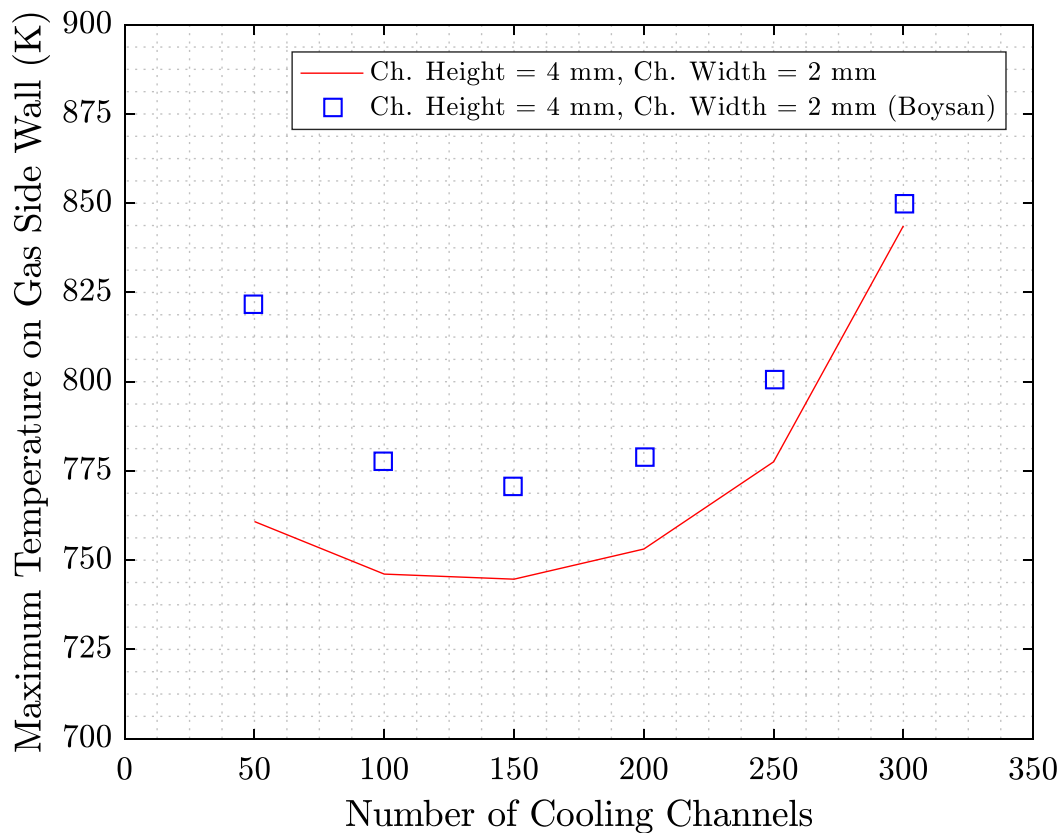


Figure 4.5. Effects of number of channels on maximum gas side wall temperature (channel geometry: $ch = 4$ mm, $cw = 2$ mm)

4.1.4.2 Comparison with Current Experiments

The experimental data obtained in the current study is also used to verify the 1D tool. One of the tests without boiling (Test-2) was chosen because the 1D tool doesn't have the ability to simulate boiling. The details of the test case can be seen in CHAPTER 3. Wall heat flux values are taken from experiments and used as input to the 1D tool. Calculated coolant wall temperatures are compared with measurements in Fig. 4.6. The 1D tool predicts slightly lower (max. difference is 3.8%) temperatures, with an acceptable overall trend.

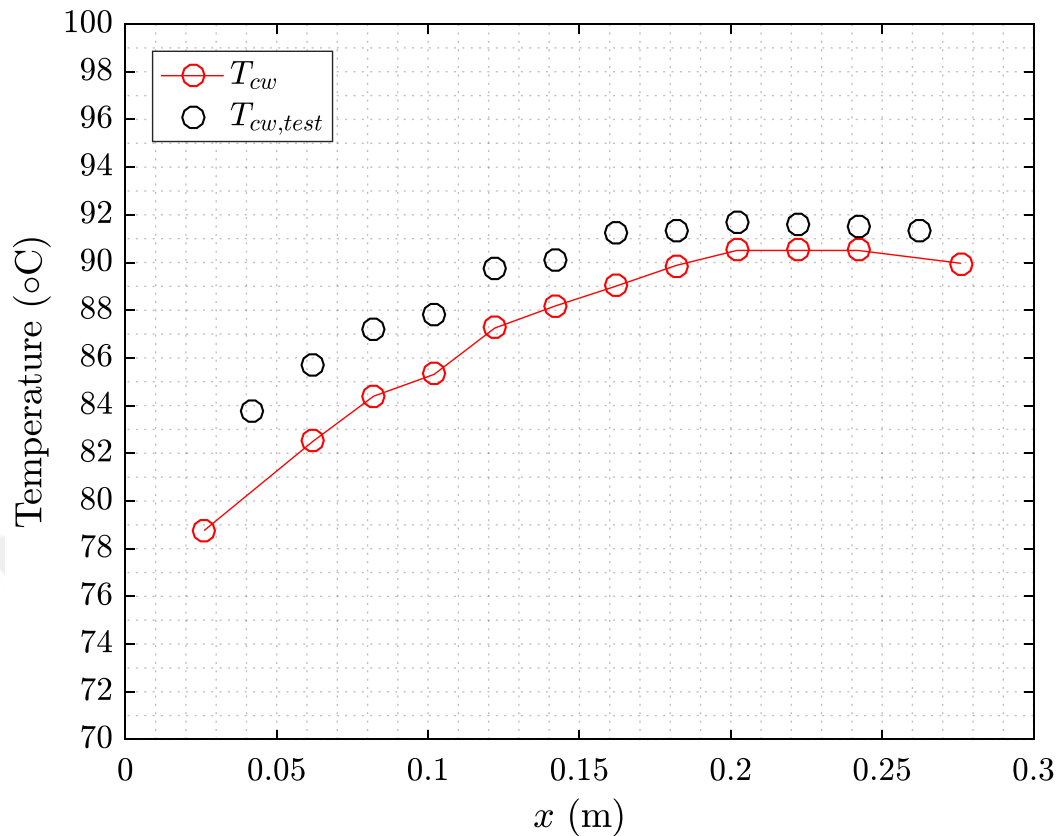


Figure 4.6. Comparison of coolant wall temperature change along the test specimen for Test-2

4.2 Two-dimensional Design Tool

4.2.1 Theoretical Background

The input to the 2D FDM solver consists of coolant inlet properties, cooling channel dimensions, number of cooling channels, map of hot gas side heat flux values with respect to wall temperatures, contour of the engine and chamber materials. The solver can calculate the temperature variation in the axial, radial and circumferential directions on the engine and the bulk coolant temperature and pressure variation in the axial direction. As shown in Fig. 4.2 (right), the LRE is divided into a predefined number of stations along the longitudinal direction and all stations are solved one by

one starting from the coolant inlet until the coolant leaves the cooling channels. The number of stations should be determined according to the required temperature distribution resolution. This procedure (sweeping all stations) continues until convergence of the temperature field is achieved.

Semi-empirical Nusselt number correlations are used to determine both the hot gas and coolant side heat transfer rates. Only half of a cooling channel cell (see Fig. 4.7) is considered because of the symmetry of the engine geometry and the fact that the side walls of the domain are assumed to be insulated/adiabatic. A finite difference grid, given in Fig. 4.7 is superimposed on the computational domain. The assumptions for the 2D FDM solver are as follows;

- The coolant mass flow rates of all cooling channels are equal.
 - The coolant mass flow distribution is controlled by coolant inlet manifolds. Only a few percent difference among channels is usually allowed in designs.
- The coolant is well mixed, so the bulk coolant temperature is valid for calculations.
 - The bulk coolant approach is the most commonly used method for 1D and 2D models. Caution should be exercised when using it in high aspect ratio channels with cryogenic coolants where stratification may occur.
- All of the heat is transferred from hot gases to the engine walls, and from the engine walls to the coolant.

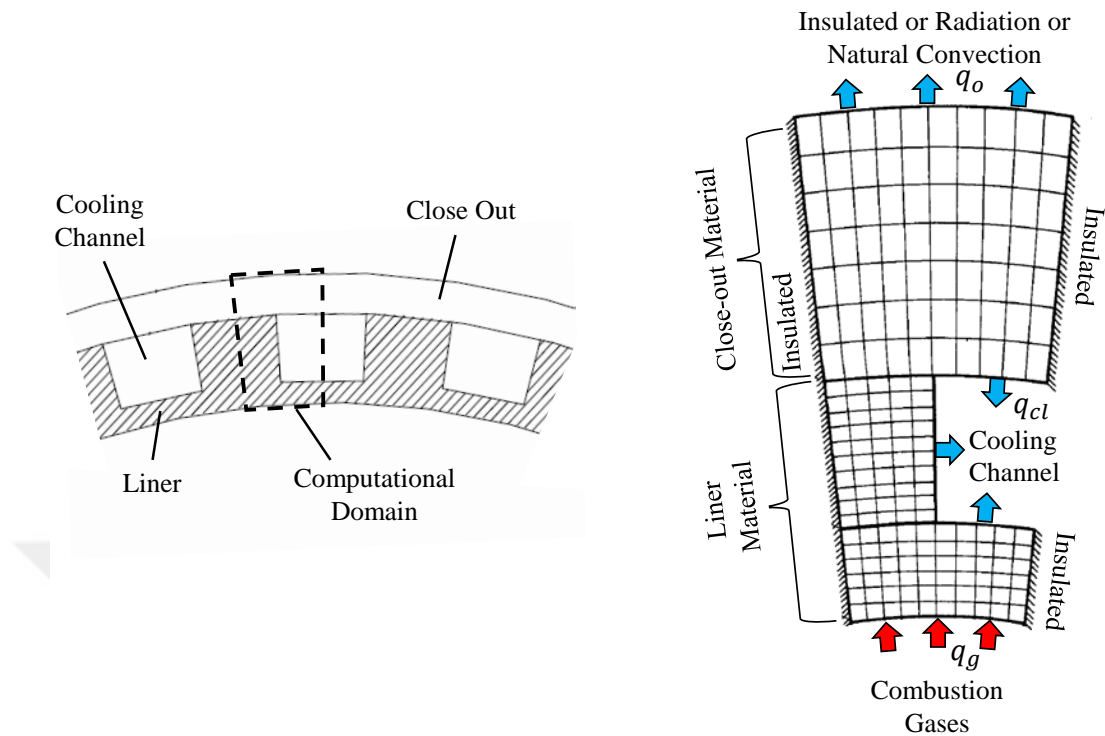


Figure 4.7. Detailed view of a station (left) and finite difference grids and boundary conditions superimposed on computational domain (right)

4.2.2 Governing Equations

For the grid that specified in Fig. 4.7, each node is connected to four nodes at the same station and is also connected to its counterpoints at the previous (n-1) and next (n+1) stations. The energy balance is written for each node cell without heat generation or storage. Only conduction heat transfer takes place between nodes and convective and radiative heat transfers are considered at boundary nodes. A typical interior node is shown in Fig. 4.8.

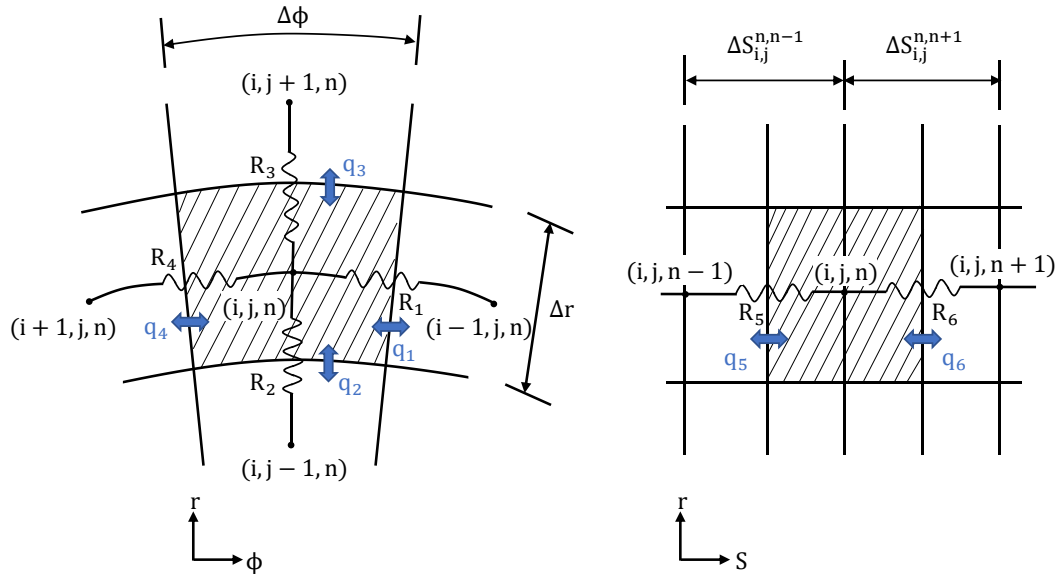


Figure 4.8. Resistances and heat fluxes of a typical interior node (Reproduced from Naraghi, 1987)

The energy balance for the interior node in Fig. 4.8 is given in Equations (4.18) and (4.19). q_1 (heat flux) is given in Equation (4.20) where T denotes nodal temperature value. Subscripts i and j are node indices and subscript n denotes the station number. k is the conductivity and is a function of temperature, i.e., $k = k(T)$. Δr and $\Delta\phi$ are the radial and angular distance between the nodes and r is the radial distance of the node from the centerline of the chamber and finally, ΔS is the distance between two stations.

$$\dot{E}_{in} - \dot{E}_{out} + \dot{E}_{gen} = \dot{E}_{st} \quad (4.18)$$

$$q_1 + q_2 + q_3 + q_4 + q_5 + q_6 = 0 \quad (4.19)$$

$$q_1 = \frac{k_{i-1,j,n} + k_{i,j,n}}{2} * \left(\Delta r * \frac{\Delta S_{i,j}^{n,n-1} + \Delta S_{i,j}^{n,n+1}}{2} \right) * \frac{(T_{i-1,j,n} - T_{i,j,n})}{r * \Delta\phi} \quad (4.20)$$

The finite difference equation for the interior node is given in Equation (4.21). The six resistances (R) are defined in Equations (4.22) - (4.27). Similarly, the area values (A) are given in Equations (4.28) and (4.29).

$$T_{i,j,n}^l = \frac{\frac{T_{i-1,j,n}^{l-1}}{R_1} + \frac{T_{i,j-1,n}^{l-1}}{R_2} + \frac{T_{i,j+1,n}^{l-1}}{R_3} + \frac{T_{i+1,j,n}^{l-1}}{R_4} + \frac{T_{i,j,n-1}}{R_5} + \frac{T_{i,j,n+1}}{R_6}}{\frac{1}{R_1} + \frac{1}{R_2} + \frac{1}{R_3} + \frac{1}{R_4} + \frac{1}{R_5} + \frac{1}{R_6}} \quad (4.21)$$

$$R_1 = \frac{r\Delta\phi}{\Delta r(\Delta S_{i,j}^{n,n-1} + \Delta S_{i,j}^{n,n+1})} \left(\frac{1}{k_{i,j,n}^{l-1}} + \frac{1}{k_{i-1,j,n}^{l-1}} \right) \quad (4.22)$$

$$R_2 = \frac{\Delta r}{(r - \Delta r/2)\Delta\phi(\Delta S_{i,j}^{n,n-1} + \Delta S_{i,j}^{n,n+1})} \left(\frac{1}{k_{i,j,n}^{l-1}} + \frac{1}{k_{i,j-1,n}^{l-1}} \right) \quad (4.23)$$

$$R_3 = \frac{\Delta r}{(r + \Delta r/2)\Delta\phi(\Delta S_{i,j}^{n,n-1} + \Delta S_{i,j}^{n,n+1})} \left(\frac{1}{k_{i,j,n}^{l-1}} + \frac{1}{k_{i,j+1,n}^{l-1}} \right) \quad (4.24)$$

$$R_4 = \frac{r\Delta\phi}{\Delta r(\Delta S_{i,j}^{n,n-1} + \Delta S_{i,j}^{n,n+1})} \left(\frac{1}{k_{i,j,n}^{l-1}} + \frac{1}{k_{i+1,j,n}^{l-1}} \right) \quad (4.25)$$

$$R_5 = \frac{\Delta S_{i,j}^{n,n-1}}{2A_{i,j,n-1}} \left(\frac{1}{k_{i,j,n}^{l-1}} + \frac{1}{k_{i,j,n-1}} \right) \quad (4.26)$$

$$R_6 = \frac{\Delta S_{i,j}^{n,n+1}}{2A_{i,j,n+1}} \left(\frac{1}{k_{i,j,n}^{l-1}} + \frac{1}{k_{i,j,n+1}} \right) \quad (4.27)$$

$$A_{i,j,n-1} = \frac{(r\Delta\phi\Delta r)_n + (r\Delta\phi\Delta r)_{n-1}}{2} \quad (4.28)$$

$$A_{i,j,n+1} = \frac{(r\Delta\phi\Delta r)_n + (r\Delta\phi\Delta r)_{n+1}}{2} \quad (4.29)$$

The semi-3D finite difference discretization is given in the set of equations, (4.22) - (4.29). In the equations, l represents the Gauss-Seidel iteration index performed at

n'th station. Values for (n-1)'th iteration are taken from the current sweep and values for (n+1)'th station are from the previous sweep. A similar set of equations is applied for the boundary nodes, with the only difference being the convective or radiative terms appearing in the nodal energy balance. The set of boundary equations for a node on the hot gas side is given in Equations (4.30) - (4.37).

$$T_{i,j,n}^l = \frac{\frac{T_{i-1,j,n}^{l-1}}{R_1} + q_g'' r \Delta\phi \frac{\Delta S_{i,j}^{n,n-1} + \Delta S_{i,j}^{n,n+1}}{2} + \frac{T_{i,j+1,n}^{l-1}}{R_3} + \frac{T_{i+1,j,n}^{l-1}}{R_4} + \frac{T_{i,j,n-1}}{R_5} + \frac{T_{i,j,n+1}}{R_6}}{\frac{1}{R_1} + \frac{1}{R_3} + \frac{1}{R_4} + \frac{1}{R_5} + \frac{1}{R_6}} \quad (4.30)$$

$$R_1 = \frac{2r\Delta\phi}{\Delta r(\Delta S_{i,j}^{n,n-1} + \Delta S_{i,j}^{n,n+1})} \left(\frac{1}{k_{i,j,n}^{l-1}} + \frac{1}{k_{i-1,j,n}^{l-1}} \right) \quad (4.31)$$

$$R_3 = \frac{\Delta r}{(r + \Delta r/2)\Delta\phi(\Delta S_{i,j}^{n,n-1} + \Delta S_{i,j}^{n,n+1})} \left(\frac{1}{k_{i,j,n}^{l-1}} + \frac{1}{k_{i,j+1,n}^{l-1}} \right) \quad (4.32)$$

$$R_4 = \frac{2r\Delta\phi}{\Delta r(\Delta S_{i,j}^{n,n-1} + \Delta S_{i,j}^{n,n+1})} \left(\frac{1}{k_{i,j,n}^{l-1}} + \frac{1}{k_{i+1,j,n}^{l-1}} \right) \quad (4.33)$$

$$R_5 = \frac{\Delta S_{i,j}^{n,n-1}}{2A_{i,j,n-1}} \left(\frac{1}{k_{i,j,n}^{l-1}} + \frac{1}{k_{i,j,n-1}} \right) \quad (4.34)$$

$$R_6 = \frac{\Delta S_{i,j}^{n,n+1}}{2A_{i,j,n+1}} \left(\frac{1}{k_{i,j,n}^{l-1}} + \frac{1}{k_{i,j,n+1}} \right) \quad (4.35)$$

$$A_{i,j,n-1} = \frac{\left(\left(r + \frac{\Delta r}{4} \right) \Delta\phi \frac{\Delta r}{2} \right)_n + \left(\left(r + \frac{\Delta r}{4} \right) \Delta\phi \frac{\Delta r}{2} \right)_{n-1}}{2} \quad (4.36)$$

$$A_{i,j,n+1} = \frac{\left(\left(r + \frac{\Delta r}{4} \right) \Delta\phi \frac{\Delta r}{2} \right)_n + \left(\left(r + \frac{\Delta r}{4} \right) \Delta\phi \frac{\Delta r}{2} \right)_{n+1}}{2} \quad (4.37)$$

The heat flux q_g'' that appears in Equation (4.30) is actually a function of wall temperature, hence it is calculated for the $T_{i,j,n}^{l-1}$. A map of the heat flux values for the range of possible wall temperature values is generated beforehand by another function using the Bartz's equation. This procedure will be described in detail in Section 4.1.2. The set of equations for a node in the upper wall of the cooling channel is given in Equations (4.38) - (4.46).

$$T_{i,j,n}^l = \frac{\frac{T_{i-1,j,n}^{l-1}}{R_1} + \frac{T_{cl,n}}{R_2} + \frac{T_{i,j+1,n}^{l-1}}{R_3} + \frac{T_{i+1,j,n}^{l-1}}{R_4} + \frac{T_{i,j,n-1}}{R_5} + \frac{T_{i,j,n+1}}{R_6}}{\frac{1}{R_1} + \frac{1}{R_2} + \frac{1}{R_3} + \frac{1}{R_4} + \frac{1}{R_5} + \frac{1}{R_6}} \quad (4.38)$$

$$R_1 = \frac{2r\Delta\phi}{\Delta r(\Delta S_{i,j}^{n,n-1} + \Delta S_{i,j}^{n,n+1})} \left(\frac{1}{k_{i,j,n}^{l-1}} + \frac{1}{k_{i-1,j,n}^{l-1}} \right) \quad (4.39)$$

$$R_2 = \frac{2}{h_{cl}r\Delta\phi(\Delta S_{i,j}^{n,n-1} + \Delta S_{i,j}^{n,n+1})} \quad (4.40)$$

$$R_3 = \frac{\Delta r}{(r + \Delta r/2)\Delta\phi(\Delta S_{i,j}^{n,n-1} + \Delta S_{i,j}^{n,n+1})} \left(\frac{1}{k_{i,j,n}^{l-1}} + \frac{1}{k_{i,j+1,n}^{l-1}} \right) \quad (4.41)$$

$$R_4 = \frac{2r\Delta\phi}{\Delta r(\Delta S_{i,j}^{n,n-1} + \Delta S_{i,j}^{n,n+1})} \left(\frac{1}{k_{i,j,n}^{l-1}} + \frac{1}{k_{i+1,j,n}^{l-1}} \right) \quad (4.42)$$

$$R_5 = \frac{\Delta S_{i,j}^{n,n-1}}{2A_{i,j,n-1}} \left(\frac{1}{k_{i,j,n}^{l-1}} + \frac{1}{k_{i,j,n-1}} \right) \quad (4.43)$$

$$R_6 = \frac{\Delta S_{i,j}^{n,n+1}}{2A_{i,j,n+1}} \left(\frac{1}{k_{i,j,n}^{l-1}} + \frac{1}{k_{i,j,n+1}} \right) \quad (4.44)$$

$$A_{i,j,n-1} = \frac{\left(\left(r + \frac{\Delta r}{4} \right) \Delta\phi \frac{\Delta r}{2} \right)_n + \left(\left(r + \frac{\Delta r}{4} \right) \Delta\phi \frac{\Delta r}{2} \right)_{n-1}}{2} \quad (4.45)$$

$$A_{i,j,n+1} = \frac{\left(\left(r + \frac{\Delta r}{4} \right) \Delta \phi \frac{\Delta r}{2} \right)_n + \left(\left(r + \frac{\Delta r}{4} \right) \Delta \phi \frac{\Delta r}{2} \right)_{n+1}}{2} \quad (4.46)$$

where $T_{cl,n}$ is the coolant static temperature at station n. h_{cl} is the convective heat transfer coefficient which can be calculated from an appropriate Nusselt number correlation given in Section 4.1.3.

4.2.3 Prediction of the Onset of Nucleate Boiling (ONB)

In two separate studies (Davis & Anderson, 1966; Liu et al., 2005), two very similar correlations (Equations (4.47) and (4.48)) were derived to calculate the wall temperature values at which ONB occurs.

$$T_{wc,ONB} = T_{sat} + 2\sqrt{T_{sat}} \sqrt{\frac{2\sigma C q''_{cl}}{\rho_v h_{fg} k_{cl}}} \quad (4.47)$$

$$T_{wc,ONB} = T_{sat} + 2\sqrt{T_{sat}} \sqrt{\frac{2\sigma C q''_{cl}}{\rho_v h_{fg} k_{cl}}} + \frac{2\sigma C q''_{cl}}{\rho_v h_{fg} k_{cl}} \quad (4.48)$$

where $T_{wc,ONB}$ is the minimum wall temperature of the channel where ONB occurs and T_{sat} is the saturation temperature of the coolant. q''_{cl} is the wall heat flux. ρ_v , h_{fg} , k_{cl} and σ are the vapor density, latent heat, fluid conductivity and surface tension. Finally, C is the shape factor, and its formula is given in Equation (4.49), where θ is the contact angle of the vapor bubble with the surface and is taken as 90 degrees in both studies (Davis et al., 1966; Liu et al., 2005). This value is supported by Shakir and Thome's (1986) measurement of 86 degrees for water/copper contact. Liu and others (2005) also stated that the selection greater than 90 degrees adequately represents the boiling physics at bubble inception in the absence of accurate measurements of the contact angle. Therefore, C equals 1.

$$C = 1 + \cos\theta \quad (4.49)$$

Both authors (Davis et al., 1966; Liu et al., 2005) made the same important assumptions;

1. The bubble nucleus that develops at a surface cavity takes the shape of a truncated sphere.
2. The vapor and liquid phases are in equilibrium under saturated conditions.
3. The bubble nucleus does not change the temperature profile of the surrounding fluid.

As can be followed, Equations (4.47) and (4.48) are very similar. Only the third term on the right-hand side of Equation (4.48) is different from Equation (4.47). Liu, Lee and Garimella (2005) noted that this term acts as correction for Equation (4.47), with the extra term making only 0.2 °C difference on $T_{wc,ONB}$ over a wide range of wall heat fluxes.

4.2.4 Coolant Side Heat Transfer for Subcooled Flow Boiling Regime

There are several subcooled boiling heat transfer correlations in literature (Shakir & Thome, 1986; Mohammed, 1977; Kandlikar, 1998). Among others, Mohammed's correlation (Mohammed, 1977) stands out for the following two reasons. First, it is not a heat transfer correlation but a correction (Equation (4.50)) to the single-phase convective heat transfer coefficient ($h_{cl,sp}$). In this way, the correlations already used for different fluids will continue to be used. Secondly, Liu, Lee and Garimella (2005) also used Mohammed's model and compared their own experimental results of subcooled flow boiling in mini-channel with the model. They obtained a good agreement between experiments and the model.

$$h_{cl,tp} = h_{cl,sp} \left[1 + (\psi_0 - 1) \frac{T_{wc} - T_{sat}}{T_{wc} - T_{cl}} \right] \quad (4.50)$$

where $h_{cl,tp}$ is the subcooled boiling heat transfer coefficient, the subscript tp stands for two-phase. T_{cl} , T_{sat} and T_{wc} stand for coolant temperature, saturated boiling temperature and coolant wall temperature respectively. ψ_0 comes from saturated boiling with zero subcooling and indicates that the coolant temperature, T_{cl} is equal to the saturated boiling temperature, T_{sat} , and can be found by using the following equation:

$$\psi_0 = \begin{cases} 230Bo^{0.5} & (Bo > 3 * 10^{-5}) \\ 1 + 46Bo^{0.5} & (Bo < 3 * 10^{-5}) \end{cases} \quad (4.51)$$

where Bo represents the boiling number, which is defined as follows:

$$Bo = \frac{q''_{cl}}{Gh_{fg}} \quad (4.52)$$

In this equation, q''_{cl} , G and h_{fg} are wall heat flux, mass flux and latent heat respectively.

The prediction of the ONB and subcooled boiling heat transfer coefficient is implemented in the 2D FDM code as follows;

1. Calculate $T_{wc,ONB}$ at coolant wall nodes using Equation (4.48). (q''_{cl} is calculated using the values obtained from the previous Gauss-Seidel iteration.)
2. If $T_{wc} > T_{wc,ONB}$, calculate $h_{cl,tp}$ and change ONB flag from 0 to 1.
3. Display and update ONB location at the user interface at each sweep.

4.2.5 Coolant Pressure Loss

P_{cl} decreases along the cooling channel and needs to be calculated at each station using Equations (4.53) and (4.54).

$$P_{cl_n} = P_{cl_{n-1}} - \Delta P_{cl_{n-1,n}} \quad (4.53)$$

$$\Delta P_{cl_{n-1,n}} = \frac{1}{2} f \frac{\Delta S_{n,n-1}}{0.5 * (D_{h_{n-1}} + D_{h_n})} \frac{(\rho_{cl_n} + \rho_{cl_{n+1}})}{2} \frac{(V_{cl_n}^2 + V_{cl_{n+1}}^2)}{2} \quad (4.54)$$

where f is the Darcy friction factor. D_h is the hydraulic diameter of the cooling channel. ρ_{cl} is the coolant density and V_{cl} is the coolant velocity.

The coolant static temperature is a function of the coolant static pressure and coolant static enthalpy (i_{cl}), i.e., $T_{cl} = f(P_{cl}, i_{cl})$. At the first station, the stagnation enthalpy is calculated using the coolant inlet temperature and pressure. The enthalpy increases along the cooling channel and can be calculated using Equation (4.55).

$$i_{c0_n} = i_{c0_{n-1}} + \frac{0.5(q_n + q_{n-1})\Delta S_{n,n-1}}{\dot{m}_{cl}} \quad (4.55)$$

where q_n is the heat transferred from the hot gases to the coolant per unit nozzle length at station n . \dot{m}_{cl} is the coolant mass flow rate. The static enthalpy is then calculated using the following equation.

$$i_{cl_n} = i_{cl_n} - \frac{V_{cl_n}^2}{2} \quad (4.56)$$

4.2.6 Solution Procedure

The inputs of the solver are listed below;

- Contour of the engine,
- Mass flow rate of coolant,
- Coolant temperature and pressure at the cooling channel inlet,
- Thermodynamic properties of coolant,
- Number and geometry of cooling channels,
- Map of hot gas side heat flux values versus temperatures,
- The name of liner and close-out materials.

After reading the inputs, the solver divides the nozzle into stations and creates the FDM mesh for each station. Then, the code sweeps all stations axially from one station to next. At each station, the coolant properties are updated and then the Gauss-Seidel iterative method is used to achieve convergence for the temperature distribution along the radial and circumferential directions. When the axial sweep is complete, a comparison is made between the results of the current sweep and the previous one to see if the convergence criteria in the axial direction have been met. If the criteria are not met, the code starts again at the first station and performs another sweep. The process continues until convergence is achieved. Flow chart of the code is presented in Fig. 4.9.



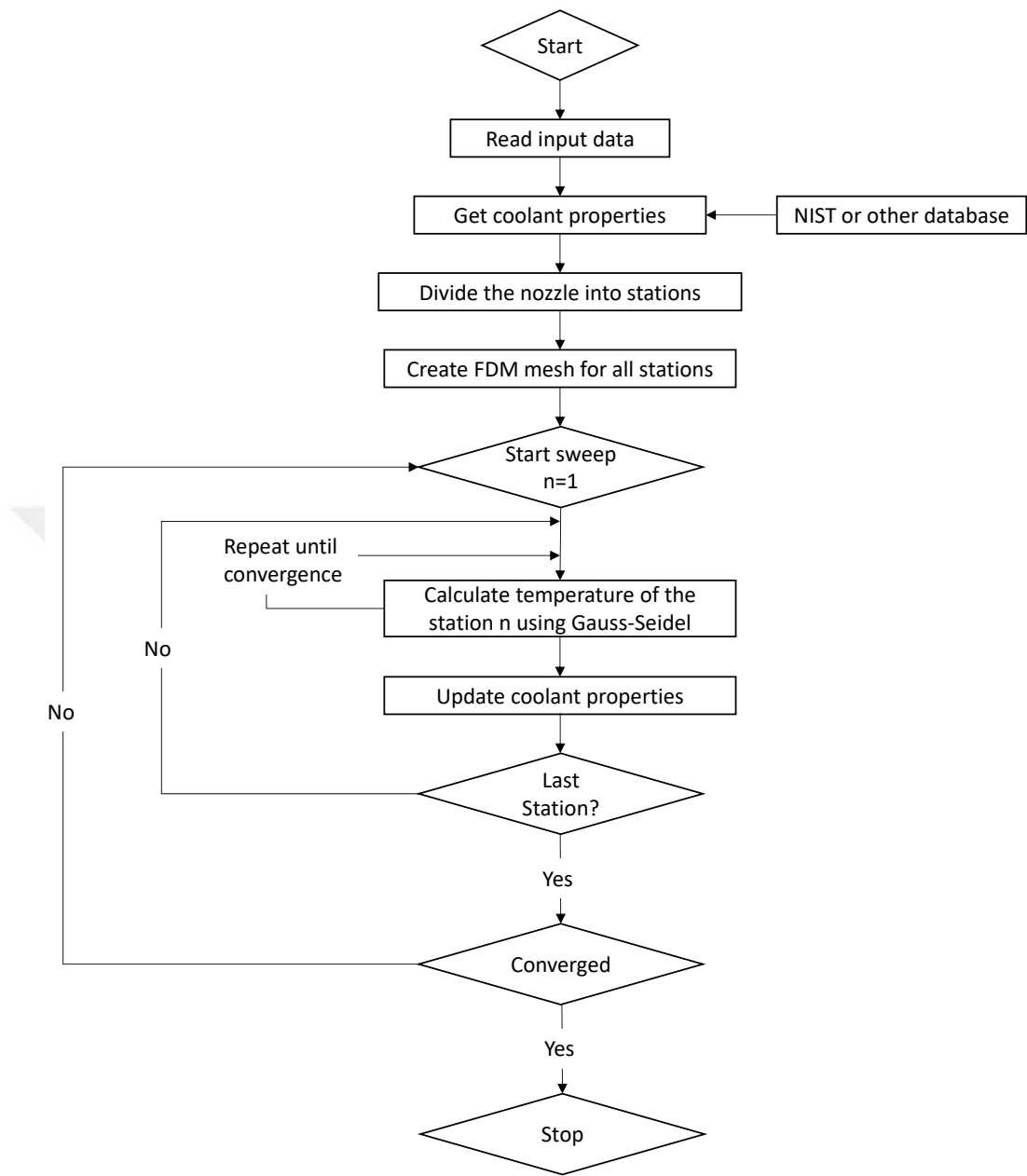


Figure 4.9. 2D FDM solver algorithm

4.3 Verification and Validation

Several validation cases in literature are performed to ensure that the governing equations and boundary conditions are correctly implemented and that the 2D FDM solver provides accurate solutions for the temperature distribution. In this section, the results of these studies are discussed.

4.3.1 89 kN LRE Cooled by Liquid Hydrogen

As a first verification and validation case, Wadel and Meyer's study on regenerative cooling channels (Wadel & Meyer, 1996) is selected. The reference work covers experiments and analyses using a liquid oxygen/gaseous hydrogen rocket engine with ~89 kN thrust. The first analysis method independently uses a three-dimensional rocket thermal evaluation code (RTE). The RTE code requires a correlation coefficient, C_g (determined by the authors based on previous experience) for the hot gas side heat transfer. The second technique uses an iteration of the heat transfer rate and hot gas side wall temperature between RTE and two-dimensional kinetics (TDK), a nozzle analysis code that uses an inviscid, boundary layer analysis technique. For both methods, a rocket combustion analysis code (ROCCID) was used by the authors to obtain an axial profile of the mixture ratio in the chamber upstream of the throat. The thrust chamber consisted of an oxygen-free high conductivity copper (OFHC) liner with nickel close-out. The coolant for this engine was liquid hydrogen, but the coolant was supplied separately to the cooling channels and did not return to the combustion chamber to burn. There were 100 cooling channels with an aspect ratio of ~2.5 across the chamber. The cooling channels were bifurcated (the channels were split into two channels and combined back into a single channel) and the aspect ratio was increased to 5 near the throat area to able to cool the throat section. The bifurcated region can be seen in Fig. 4.10. The size of the cooling channel geometry is not specified in this paper but can be found in another paper by the same author (Wadel, 1997).

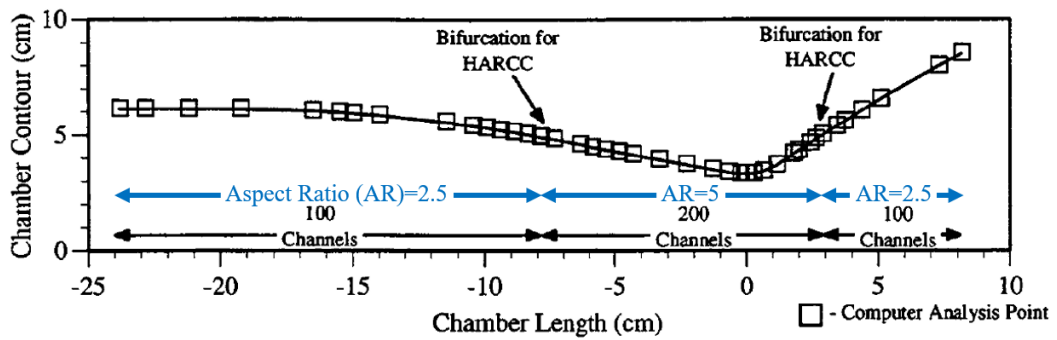


Figure 4.10. Combustion chamber contour with bifurcation regions indicated (Wadel, 1997)

In this study, the materials used in the analysis were liquid hydrogen (“Thermophysical Properties of Fluid Systems”, 2021) for the coolant, oxygen-free high conductivity copper (OFHC) for the inner wall and nickel for the close-out (Boysan, 2008).

A mesh independence study using 4 different grids (Table 4.1) is conducted to choose the computational grid. As can be seen in Fig. 4.11, wall temperature values almost don't change after fine grid (7x14), so it is chosen.

Table 4.1. Grids used in mesh independence study

Grid Name	Number of grids in circumferential direction	Number of grids in radial direction
Coarse	3	8
Medium	5	11
Fine	7	14
Very Fine	9	17

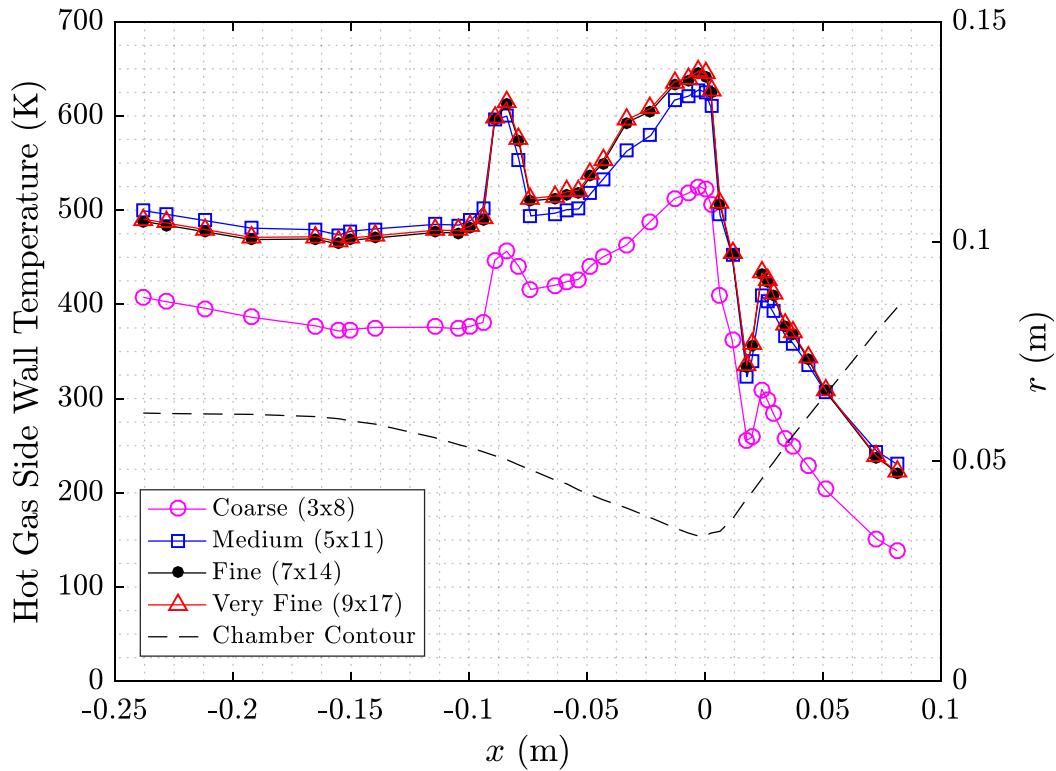


Figure 4.11. Wall temperature values with grids used in mesh independence study (hot gas side wall temperature on the left axis and chamber radius on the right axis)

The analyses are stopped after each station and a sweep-to-sweep accuracy (temperature change at each iteration) of 0.1% is obtained. The comparison of the hot gas side wall temperature obtained with the developed code with the analysis results of three reference studies (Wadel & Meyer, 1996; Boysan, 2008; Suer, Cenik & Uslu, 2019) along the nozzle can be seen in Fig. 4.12. Both Boysan and Suer et al. (2019) solved the problem using CFD software. Compared to Wadel and Meyer, the trend of hot gas side wall temperatures is very similar and the numerical results are in very good agreement except immediately before and after the bifurcation, whereas Suer et al. predicted similar temperature jump at the beginning of the bifurcation, but the sudden temperature change at the end of the bifurcation in both Boysan and Suer et al. is small. Some corrections can be made on these points for Wadel and Meyer's method, but currently there is no special treatment for the beginning and end of bifurcation in the current code. Also, the current code overestimates the wall

temperature at the very beginning of the cooling channels (at the end of divergent part) compared to Wadel and Meyer. However, this part is not critical for a rocket nozzle and can be corrected by considering the entrance effect.

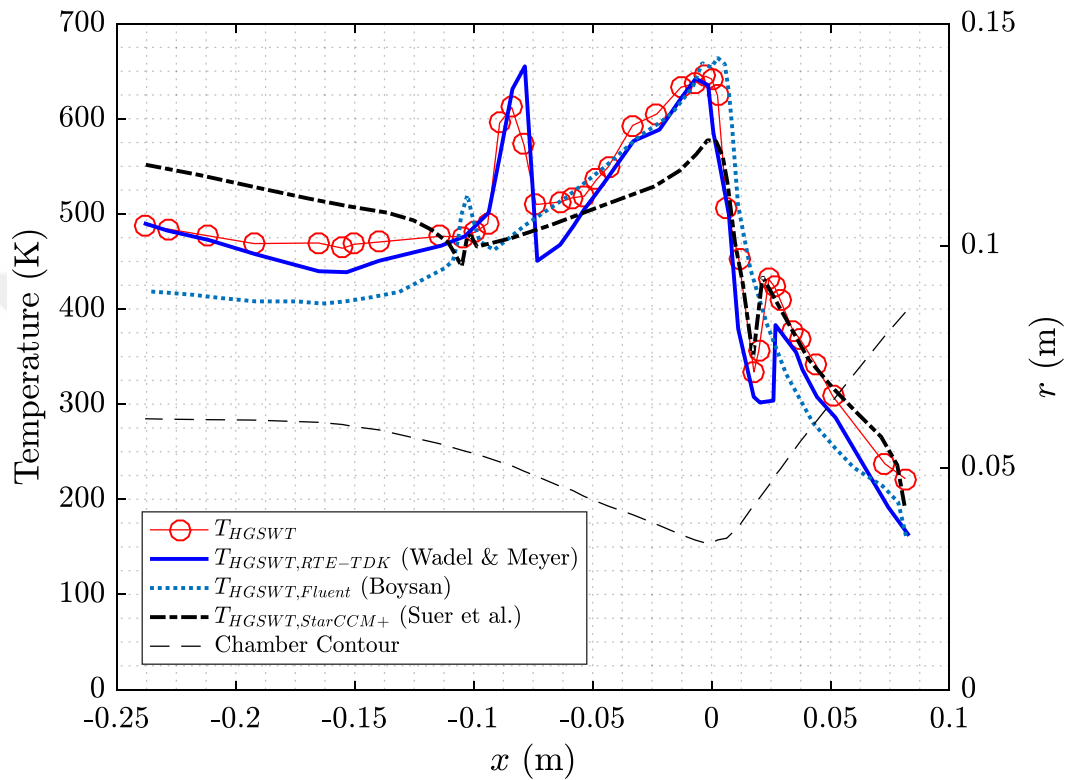


Figure 4.12. Comparison of hot gas side wall temperature along the nozzle with the reference studies (Wadel & Meyer, 1996; Boysan, 2008; Suer et al., 2019) (hot gas side wall temperature on the left axis and chamber radius on the right axis)

In the reference study, a set of rib thermocouples (see Fig. 4.13) was placed in three different axial positions in hot firing tests. Figure 4.14 presents a comparison of the rib temperature obtained with the currently developed code with Wadel and Meyer’s analysis and experimental results. The rib temperature predictions in Suer’s study are also shown in the figure.

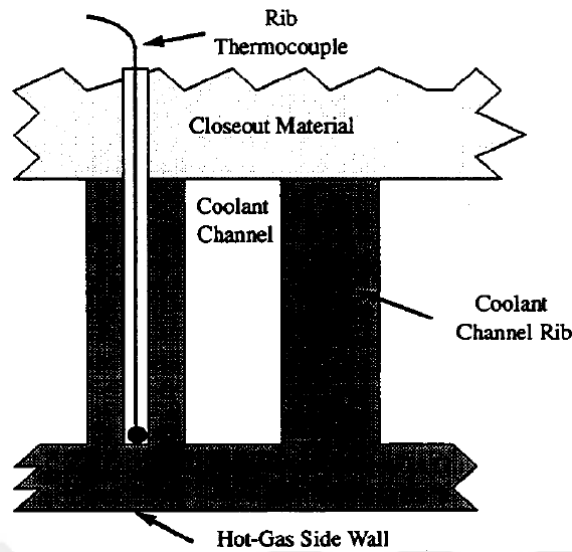


Figure 4.13. Ideal rib thermocouple placement (Wadel & Meyer, 1996)

As can be seen in Fig. 4.14, there is more than one temperature value for the results of Wadel and Meyer's analysis. Some thermocouples depths differed from the ideal placements and these different depths were taken into account for the reference analysis. However, these non-nominal locations are not specified, so there is only one temperature value to compare with the current analysis. With this information considered, it can be said that the results are in good agreement with test data. The rib temperature prediction of the current code differs from the test data by ~15% in the convergent section. The predictions for the combustion chamber and the convergent section are at the upper limit of the test data. The rib temperature results of the current analysis are more close to the RTE-TDK coupled method between the two different analysis methods in the reference study. In addition, except for the location $x = -0.15$ m, the current predictions are in good agreement with the CFD study of Suer et al.

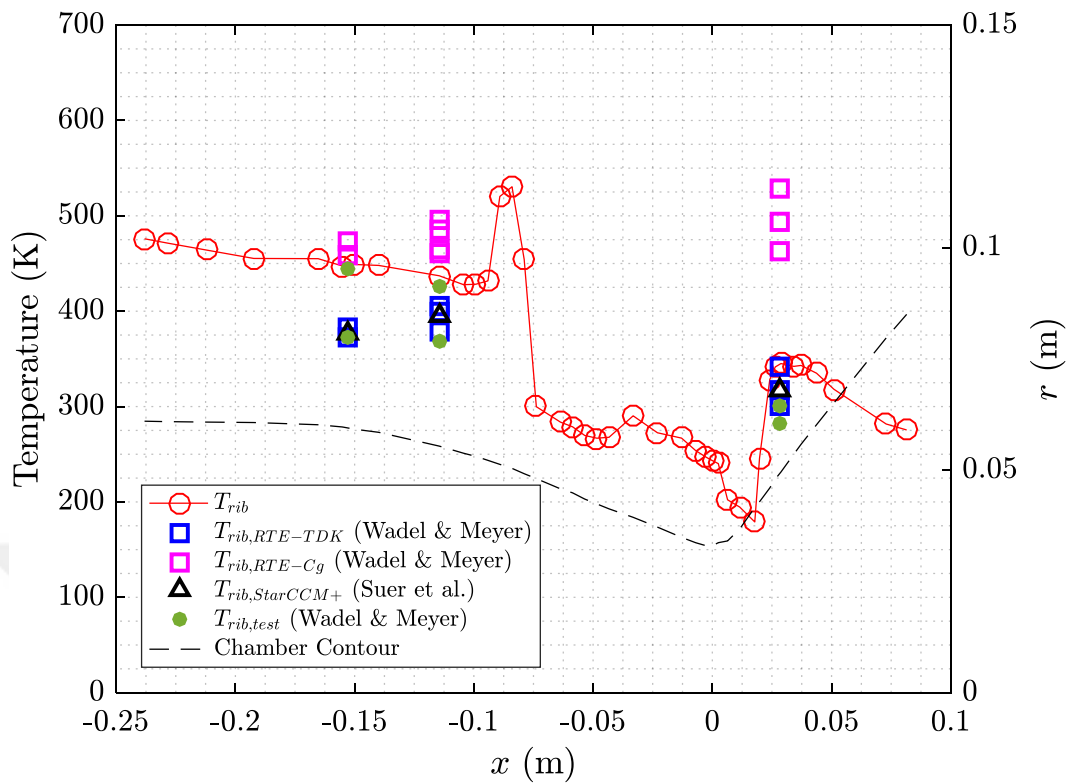


Figure 4.14. Rib thermocouple temperature comparison of reference experimental and analysis (Wadel & Meyer, 1996; Suer et al., 2019) versus current analysis results (rib thermocouple temperature on the left axis and chamber radius on the right axis)

4.3.2 100 kN LRE Cooled by Liquid Oxygen

Naraghi's work (Naraghi & Armstrong, 1988) is chosen as the second validation case. The reference study also used a 2D FDM solver coupled with a 2D kinetics code to predict temperature distribution of a ~100 kN liquid oxygen/kerosene rocket engine. This engine uses liquid oxygen (LOX) as the coolant. The cooling channel geometry varies throughout the engine to cool critical sections such as the throat. Further details of the engine can be found in Naraghi's work (Naraghi & Armstrong, 1988).

The same computational grid (7 x 14) as the previous validation was used. The comparison of coolant and inner wall temperature along the nozzle and can be seen in Fig. 4.15.

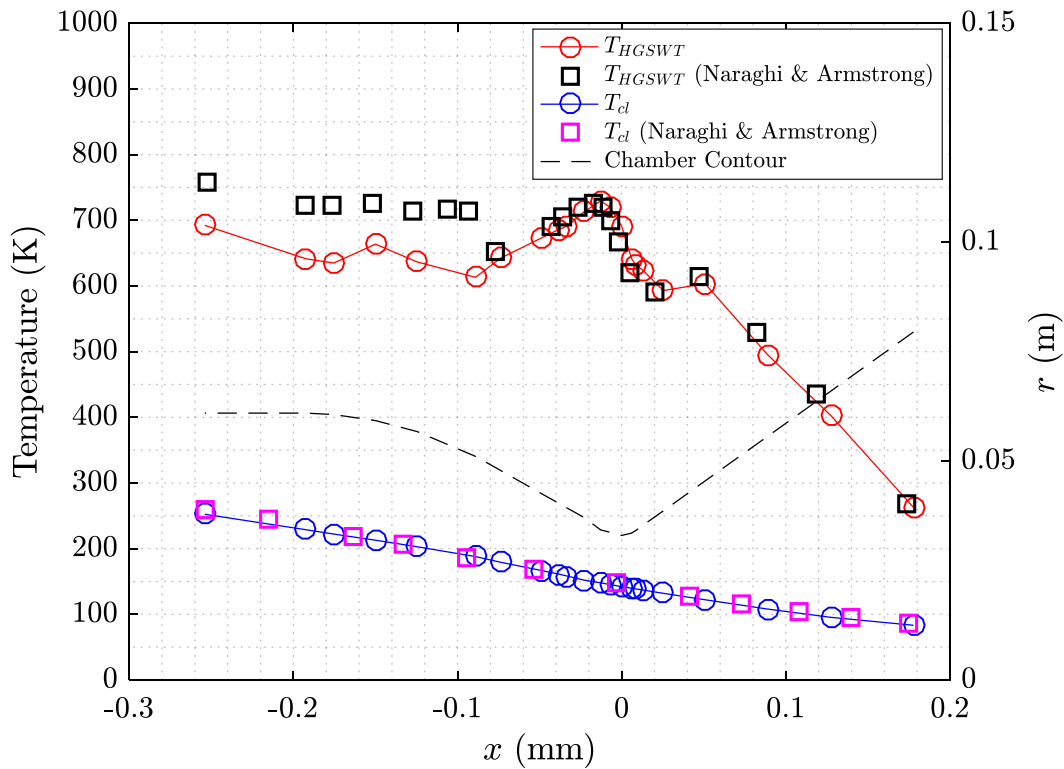


Figure 4.15. Comparison of the inner wall and coolant temperature along the nozzle with the reference study (Naraghi & Armstrong, 1988) (temperature on the left axis and chamber radius on the right axis)

As can be seen from Fig. 4.15, the inner wall and coolant temperatures are in good agreement in the converging section, the diverging section and throat. However, there is a ~80 K difference in the inner wall temperatures in the combustion chamber part of the nozzle. This difference could be the result of the difference in the hot gas side heat flux calculation methods between two approaches. Similar to the wall temperatures, the coolant temperature distribution in the reference study is slightly higher in the combustion chamber than in the current study. A possible explanation

for this difference could be the use of a different hot gas side heat transfer method than the reference study. In the present study, the semi-empirical Bartz equation developed specifically for rocket engine applications was used. The Bartz equation assumes constant fluid (hot gas) properties in the combustion chamber and utilizes these properties throughout the nozzle. The effect of the nozzle geometry is taken into account by adding the parameters throat diameter, throat curvature and area ratio (A/A_t) to the Nusselt number. Naraghi, on the other hand, calculates the fluid properties at each station using the enthalpy change of the hot gas along the nozzle. He uses a Nusselt number correlation based only on Reynolds and Prandtl Numbers.

4.3.3 ONB on a Rectangular Channel Cooled by Water

The experimental results of Liu et al.'s (Liu, Lee & Garimella, 2005) were also used to validate the 2D FDM code. In their study, the onset of nucleate boiling in water flow through a mini-channel heat sink was investigated. The test section in Liu's study consists of 25 parallel-cut mini-channels measuring 275 μm in width, 636 μm in height and 25.4 mm in length. The test setup can be seen in Fig. 4.16.

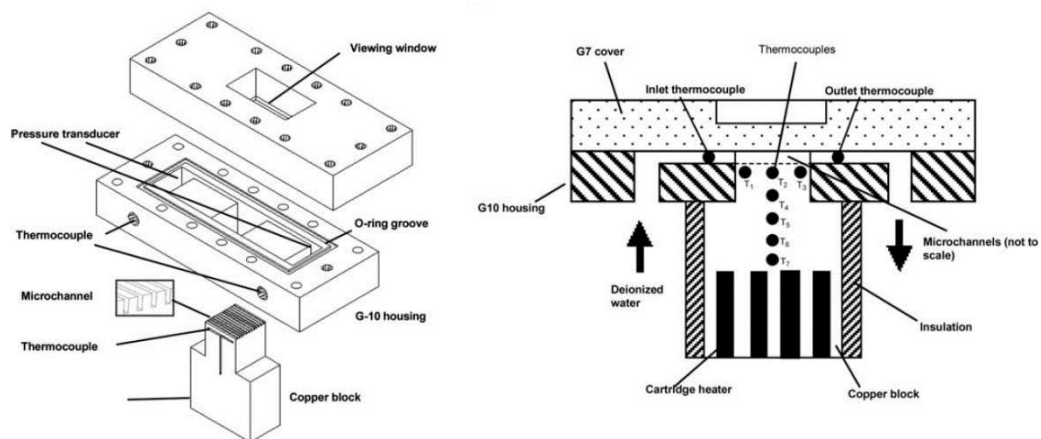


Figure 4.16. a) 3-D view of test section and right, b) cross section of test section (Liu et al., 2005)

With the high-speed imaging system, the authors provided incipient heat flux values where a single bubble or several bubbles can be observed (see Fig. 4.17). They measured ONB heat fluxes for various fluid inlet velocities and temperatures. Two of the selected validation cases are presented in Table 4.2.

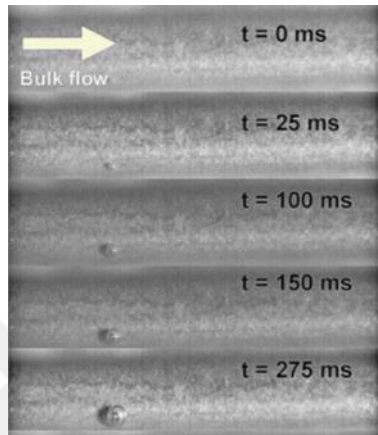


Figure 4.17. Visualization of validation Case-1 by Liu et al. (Liu et al., 2005)

Table 4.2. Selected cases from experimental study (Liu et al., 2005) for validation of the 2D FDM Solver

Case	$u_{f,in}$ (m/s)	Re	G (kg/(m ² s))	$T_{f,in}$ (°C)	P_{exit} (Pa)	$q''_{ONB,exp}$ (W/m ²)
1	0.65	731	626	86.5	103393	15.80×10^4
2	0.63	572	610	71.1	102387	27.92×10^4

Channel geometry and flow data (Liu et al., 2005) are used as input to the 2D FDM solver. As the heat flux is slowly increased, boiling is expected to be first observed at the end of the channel. For 2D FDM analyses, the heat flux is increased from zero until ONB is observed at the last computational station, that is, at the exit of the mini-channel. These heat flux values and their comparison with experimental values are

presented in Table 4.3. The 2D FDM solver predictions agree well with the experiments. The solver predictions exceed the measured values (Liu et al., 2005) by a small margin. This can be explained by the fact that the local heat flux is not uniformly distributed along the channel surface as predicted by the model (Equation (4.48)).

Table 4.3. Comparison of the 2D FMD solver predictions of incipient heat flux against experimental results (Liu et al., 2005)

Case	$q''_{ONB,exp}$ (W/m ²)	$q''_{ONB,solver}$ (W/m ²)	Error (%)
1	15.80×10 ⁴	16.71×10 ⁴	5.7
2	27.92×10 ⁴	29.93×10 ⁴	7.2

Figure 4.18 shows the coolant and channel bottom wall temperature variation along the channel for Case-1 with the 2D FDM solver. Unfortunately, no experimental data is available to compare these results. As expected, both temperature values increase from the inlet ($x = 25.4$ mm) to the outlet ($x = 0$ mm). The ONB can be seen at the last station (outlet), which is marked with filled black circle. At ONB the water temperature is below the saturation temperature, indicating subcooled boiling.

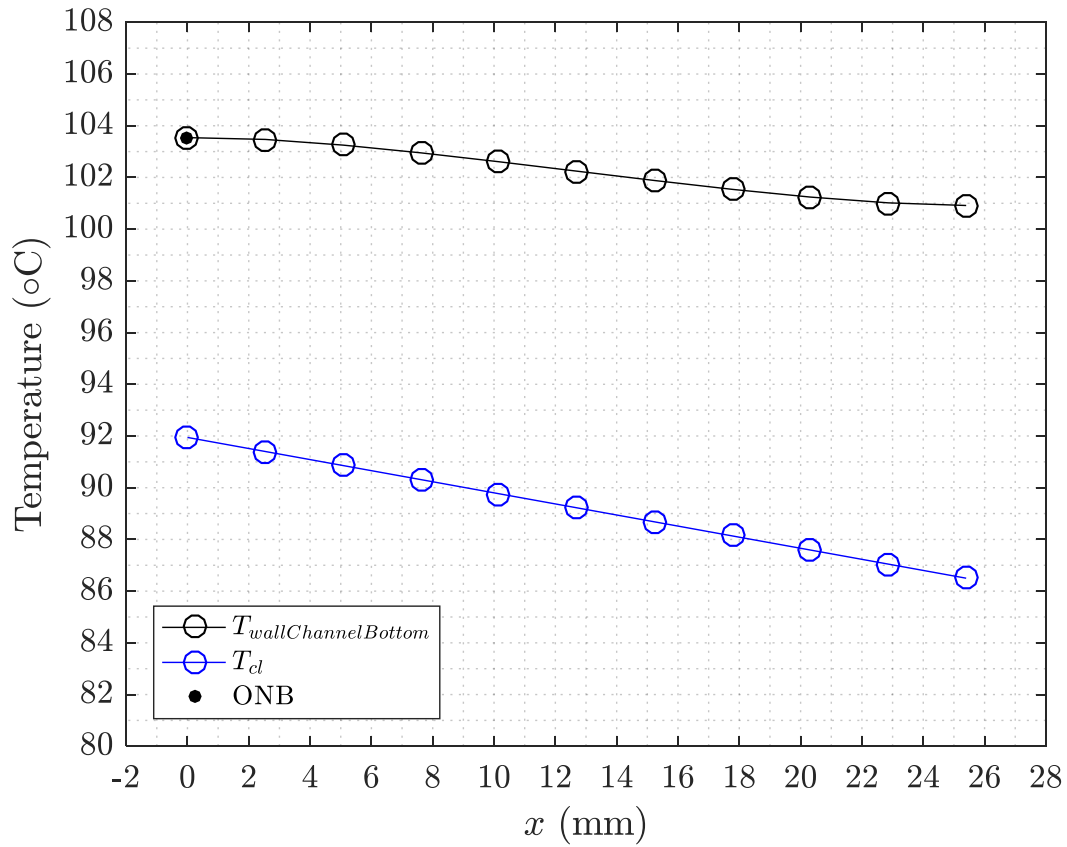


Figure 4.18. The coolant and channel bottom wall temperature change across the channel ($x_{inlet} = 25.4$ mm and $x_{outlet} = 0$ mm) for of Case-1 (calculated by the 2D FDM solver)

The temperature distribution at the channel outlet for Case-1 is presented in Fig. 4.19. As expected, the solver predicts the ONB at the bottom of the channel wall.

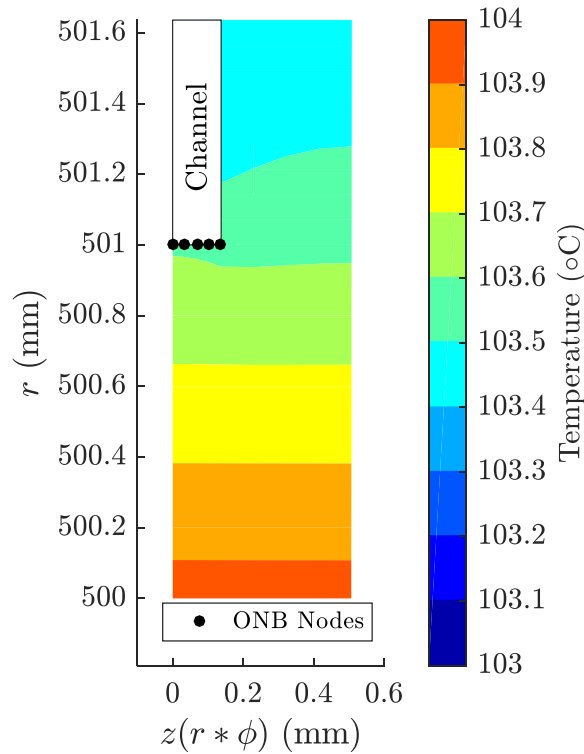


Figure 4.19. Temperature distribution at the outlet of the channel for Case-1 (calculated by the 2D FDM solver)

4.3.4 23 kN Demonstration Thrust Chamber Cooled by MMH

The demonstration thrust chamber (DTC) was one of the development engines of the Space Shuttle's Orbital Maneuvering Engine. The cooling performance of the original engine was also investigated in this chamber. The DTC is a 23 kN MMH/N₂O₄ engine. It is cooled by the fuel, MMH. Both the width and the height of the cooling channel vary throughout the engine to better cool critical sections such as throat and to reduce the pressure loss in the channel. The thrust chamber consisted of stainless-steel liner (321 CRES) with electroformed nickel close-out. Further details of the engine can be found in a NASA report (Pauckert & Tobin, 1975). The authors also published the hot gas side heat flux values along the channel. These fluxes were used in the current analysis in order to allow better comparison between results. The same computational grid, 7×14 , as the previous validation and

verification was also used for this analysis. Figure 4.20 shows the hot gas side wall temperature (T_{HGSWT}) values along the nozzle. It can be seen that the current predictions are in very good agreement with the reference data. There are two reasons for this similarity; both the current study and reference study use the 2D conduction method and the hot gas side heat flux values are the same as mentioned before. The only slight difference is observed at $x = 0.075$ m where there is a sudden change in channel width. There may be a special implementation for this station at the reference study. The pressure drop of the cooling channel is also calculated and compared with the reference study. The difference is only 9%.

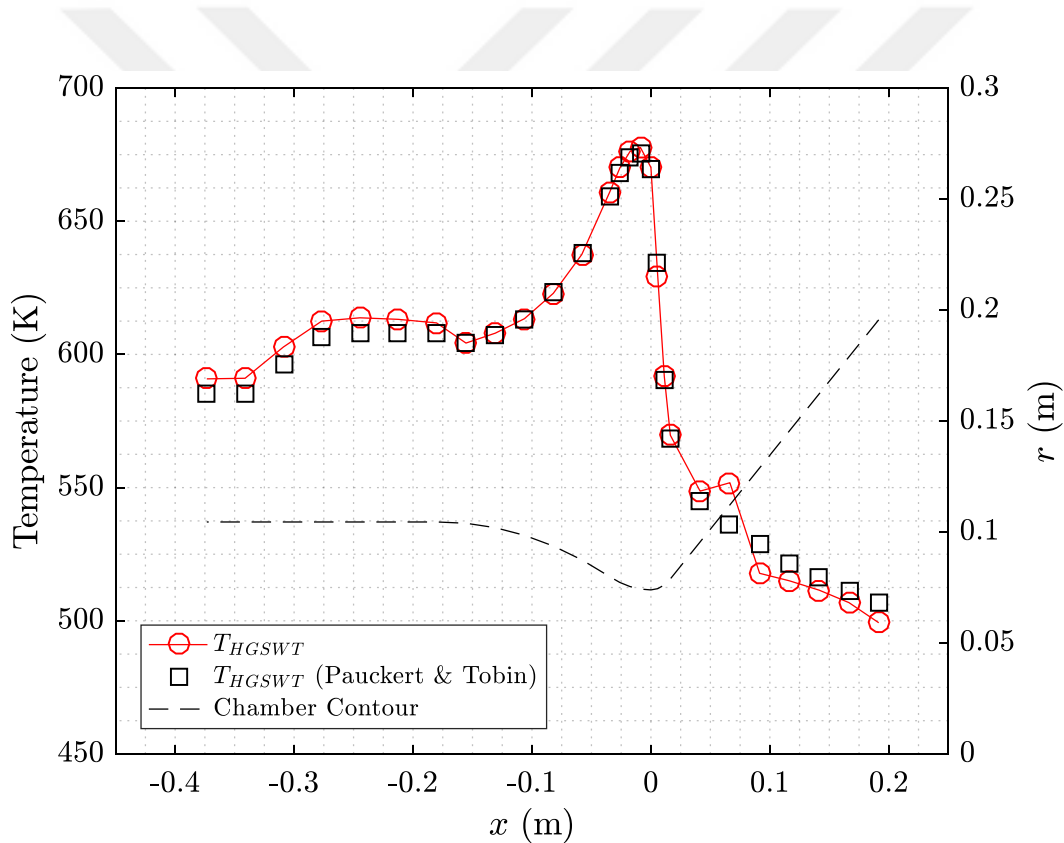


Figure 4.20. Change of hot gas side wall temperature along the DTC nozzle compared to the reference study (Pauckert & Tobin, 1975)

Pauckert and Tobin (1975) also investigated the factor of safety (FoS) of the design based on hot gas side and coolant burnout heat flux. They determined the FoS value

to be 2, which indicates that the liquid will not burnout until twice the nominal heat flux applied. Applying the same methodology, the FoS of 2.3 was calculated by 2D FDM solver. Figure 4.21 illustrates the comparison of hot gas wall temperatures with nominal wall heat flux for FoS values of 1.25, 1.5 and 2. It can be seen that for FoS of 1.5 a temperature of more than 800 K is obtained. For FoS values 1.5 and 2, boiling occurs almost throughout the chamber which can cause problems by partially or completely blocking the channel. This shows the importance of locating the boiling.

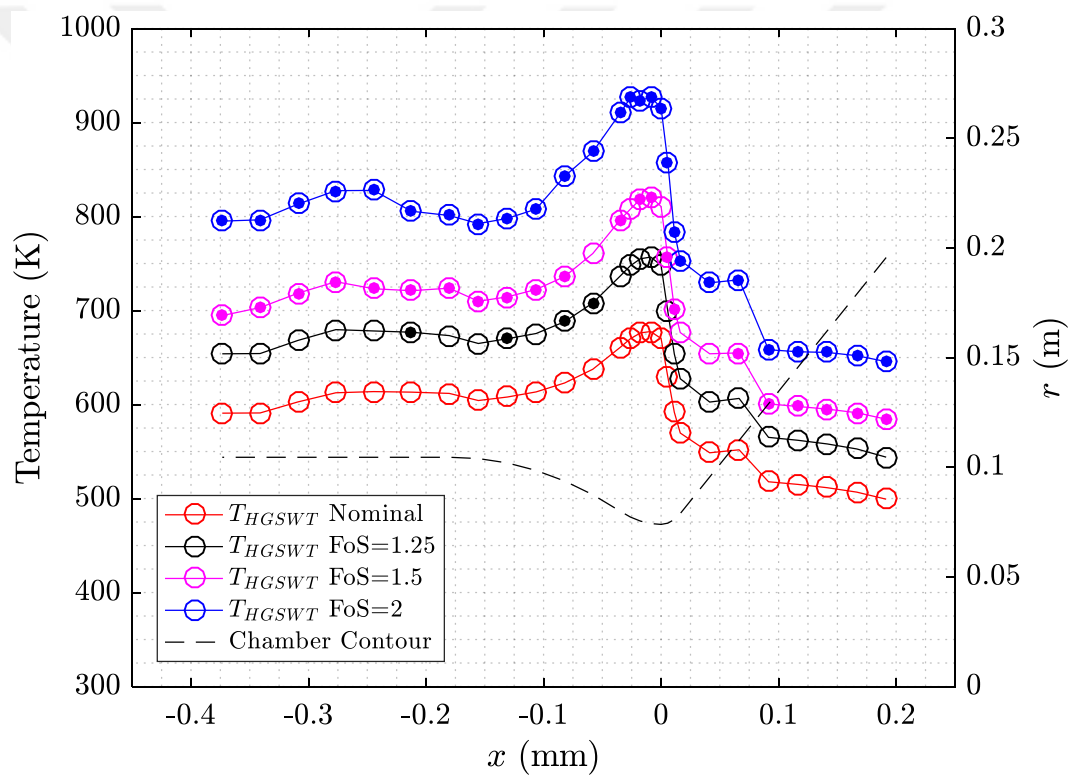


Figure 4.21. Change of hot gas side wall temperature along the DTC nozzle for different FoS values (filled circles indicates locations of boiling)

4.3.5 Comparison with Current Experiments

Lastly, experimental data obtained in the current study is also used to verify the 2D FDM tool. Two tests, one without boiling (Test-2) and the other with boiling (Test-7) are chosen for this purpose. Details of these test cases can be found in CHAPTER 3. Wall heat flux values used in the experiments are supplied as input to the 2D tool and coolant bottom wall temperatures are calculated and compared with measurements. Maximum and mean absolute errors are given in Table 4.4. According to the table, the maximum temperature difference is below 4%, indicating excellent prediction of temperature values by 2D FDM solver. The calculated channel bottom wall temperature change across the test specimen for Test-2 and Test-7 are presented in Fig. 4.22. The temperature profiles are in very good agreement with the test data. The 2D FDM solver also located the boiling region correctly. Boiling stops at the end of the channel because the wall temperature values and heat flux values are both reduced.

Table 4.4. Maximum and mean absolute error values for 2D FDM solver's coolant bottom wall temperature predictions

	Max Error	Mean Absolute Error
Test-2	3.6%	1.4%
Test-7	1.8%	0.9%

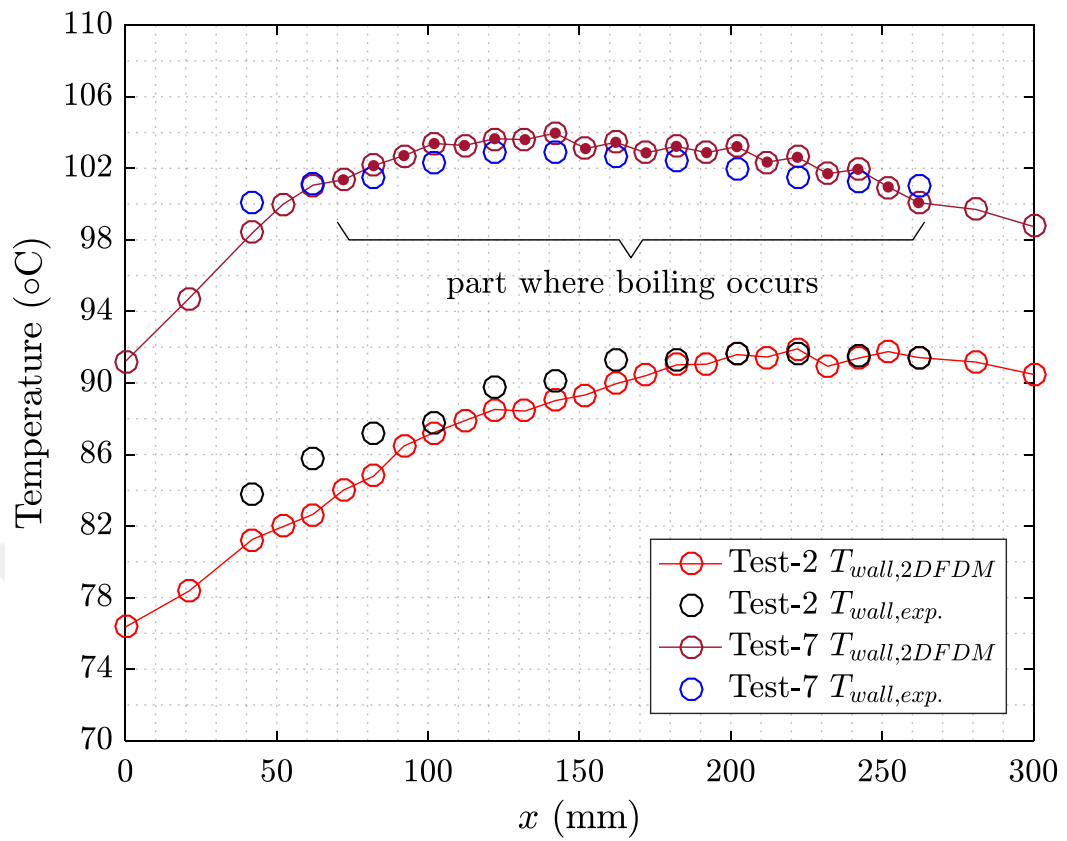


Figure 4.22. Comparison of experimental (Test-2 and Test-7) cooling channel bottom wall temperature with 2D FDM solver across the test specimen (dark red dots in dark circles denotes the part of the specimen where boiling occurs)

CHAPTER 5

3D CFD SOLVER

The most demanding part of the current work was to develop an accurate and efficient 3D two-phase flow solver with conjugate heat transfer capability. The free and open source CFD framework OpenFOAM was chosen to develop the desired 3D solver. OpenFOAM (“OpenFOAM”, n.d.) is a C++ library developed to solve continuum mechanics problems using the finite volume method. It is a popular library in CFD studies due to its wide range of readily available solvers and its open source nature. The currently available VOF-based two-phase solvers and support for adaptive mesh refinement (AMR) make OpenFOAM a good candidate for efficient and accurate 3D two-phase simulations. Numerous models and algorithms for phase change modeling are available in the literature. During the current study, comparisons were made among these models and algorithms in order to determine the optimal combination for regenerative cooling channel simulations with nucleate boiling.

The developed solver is based on the adiabatic two-phase flow code *interFoam* using VOF as the interface capturing method. The accuracy of the interface location calculated by the VOF method depends on the local cell size at the interface. Accurate estimation of the interface location is crucial for accurate calculation of the local phase change rate (Kunkelmann et al., 2011). When the VOF method fails to provide satisfactory results for interface tracking, a local reconstruction technique can provide more detailed information about the location of the interface within the cells. One of the local reconstruction methods, Piecewise Linear Interface Calculation (PLIC) developed by Rider and Kothe (1998), has already been implemented in OpenFOAM. The most obvious other solution is to use a fine mesh,

constrained by the computational resources. However, this constrain can be overcome by using AMR. In the current study, AMR is used for increasing the resolution in the interface.

First, a preliminary review of the off-the-shelf OpenFOAM solvers *interCondensatingEvaporatingFoam* and *reactingTwoPhaseEulerFoam*, as well as two solvers developed separately by Samkhaniani & Ansari (2016) and Nabil & Rattner (2016) was performed. Among these four solvers, Nabil and Rattner's *interThermalPhaseChangeFoam* (iTPCF) solver was successfully used to simulate the evaporation and condensation of a single bubble. Although a promising solver, iTPCF lacks adaptive mesh refinement (AMR) functionality as it is built using an old and outdated version of OpenFOAM. A significant amount of time was spent updating this solver to a newer version of OpenFOAM (version 8) and applying AMR capabilities to it, before delving deeper into the capabilities of the solver. The new solver is called iTPCF_OF8.

5.1 Theoretical Background

In this section, the conservation equations, VOF method and phase change models are explained in detail.

5.1.1 Mass, momentum and energy conservation

The basis of a 3D solver for the simulation of boiling phenomena are the continuity, linear momentum and conservation of energy equations. Under the assumptions of negligible viscous dissipation, negligible power supply or release due to volumetric forces, incompressible flow and Newtonian fluid, these equations can be simplified to the following set of equations.

$$\nabla \cdot \vec{u} = 0 \tag{5.1}$$

$$\frac{\partial(\rho\vec{u})}{\partial t} + \nabla \cdot (\rho\vec{u}\vec{u}) = -\nabla p + \nabla \cdot [\mu(\nabla\vec{u} + (\nabla\vec{u})^T)] + \rho\vec{g} \quad (5.2)$$

$$\frac{\partial(\rho c T)}{\partial t} + \nabla \cdot (\rho c T \vec{u}) = \nabla \cdot (k \nabla T) \quad (5.3)$$

where ρ is the density, μ is the viscosity, c is the specific heat capacity, k is the thermal conductivity and \vec{g} is the gravitational acceleration. \vec{u} , p and T are the velocity, pressure and temperature fields, respectively. The flow domain is divided into two subdomains, liquid and vapor, and Equations (5.1) to (5.3) apply to each subdomain.

5.1.2 Interface tracking with volume of fluid method (VOF)

The volume of fluid (VOF) method was developed by Hirt and Nichols (1981). It is one of the most widely used methods among researchers to capture sharp interfaces between the phases. Compared to level set and front tracking techniques, it conserves mass better but captures the interface less sharply. In the VOF method, the mass, momentum and energy equations are solved according to the volume fraction of the phases in each computational cell, and the sum of the volume fractions of the liquid and vapor phases is unity in each cell (Ramiar & Ranjbar, 2015).

$$\alpha_l + \alpha_v = 1 \quad (5.4)$$

$$\alpha_l(x, y, z, t) = \frac{\forall_l}{\forall} = \begin{cases} 1 & \text{liquid} \\ 0 < \alpha_l < 1 & \text{interface} \\ 0 & \text{vapor} \end{cases} \quad (5.5)$$

where α_l and α_v are the volume fractions of the liquid and vapor phases, \forall_l and \forall are the volume of liquid in a cell and the total cell volume. $\alpha_l = 0$ and $\alpha_l = 1$ represent completely vapor and completely liquid cells. The range $0 < \alpha_l < 1$ represents a cell filled with both vapor and liquid phases, i.e. the interface region between the phases. The average density of the vapor-liquid mixture in these cells can be defined as

$$\rho = \alpha_l \rho_l + (1 - \alpha_l) \rho_v \quad (5.6)$$

The same equation can be used to calculate the average viscosity, thermal conductivity and specific heat capacity. The set of governing equations for a two-phase flow with source terms related to phase change is given below

$$\nabla \cdot \vec{u} = \dot{m} \left(\frac{1}{\rho_v} - \frac{1}{\rho_l} \right) \quad (5.7)$$

$$\frac{\partial(\rho \vec{u})}{\partial t} + \nabla \cdot (\rho \vec{u} \vec{u}) = -\nabla p + \nabla \cdot [\mu(\nabla \vec{u} + (\nabla \vec{u})^T)] + \rho \vec{g} + \vec{f}_{st} \quad (5.8)$$

$$\frac{\partial(\rho c T)}{\partial t} + \nabla \cdot (\rho c T \vec{u}) = \nabla \cdot (k \nabla T) + \dot{m} h_{lv} \quad (5.9)$$

where \dot{m} is mass change between the phases and h_{lv} is the latent heat. $\dot{m} h_{lv}$ term represents the heat transferred between phases. \vec{f}_{st} is the volumetric surface tension force in the vicinity of the interface. It is shown as follows:

$$\vec{f}_{st} = \sigma \left[\nabla \left(\frac{\nabla \alpha}{|\nabla \alpha|} \right) \right] \nabla \alpha \frac{2\rho}{\rho_v + \rho_l} \quad (5.10)$$

where σ is the surface tension coefficient. With the addition of \vec{f}_{st} in the momentum equation, interaction between the phases are fully defined.

5.1.3 Phase change models

In the literature, various researchers such as Hardt and Wondra (2008), Schrage (1953), Tanasawa (1991), Lee (2013) and Nabil and Rattner (2016) proposed different phase change models. The ones proposed in the last two references which are the mostly employed model in literature, are analyzed in this study.

Lee (2013) developed the following equations to determine the phase change heat rate in each cell using empirical rate parameters

$$\dot{q}_{pc} = \begin{cases} r_l \alpha \rho_l \frac{(T - T_{sat})}{T_{sat}} & \text{if } T \geq T_{sat} \\ r_v (1 - \alpha) \rho_v \frac{(T - T_{sat})}{T_{sat}} & \text{else} \end{cases} \quad (5.11)$$

where \dot{q}_{pc} is the phase change heat rate, subscripts l , v , sat denote liquid, vapor and saturation. r_l and r_v are empirical rate parameters that control how much liquid evaporates to vapor and vice versa. This method has the advantages of being conceptually straightforward and resulting in a smooth source term field. However, it applies phase change effects to the entire problem domain, not just at the liquid-vapor interface.

The interface equilibrium model of Nabil and Rattner's (Nabil & Rattner, 2016) performs a graph scan over the cells of the mesh and applies phase change to the two-cell-thick interface layer using a user-specified threshold value based on α . There are two thresholds, `CondThresh` and `EvapThresh`, to control condensation and evaporation. In order to maintain thermal equilibrium at the interface at each time step, the model forces the interface cells to recover their saturation temperature.

5.2 Verification and Validation Simulations

Six test cases are used to verify and validate the updated solver. The problems used are;

- i) horizontal film condensation on an isothermally subcooled surface (Stefan problem),
- ii) gravity-driven smooth falling film condensation (Nusselt problem),
- iii) condensation of a small vapor bubble in a quiescent subcooled liquid environment,
- iv) a single bubble rising under the influence of buoyancy forces,
- v) subcooled flow boiling in a rectangular channel,

- vi) current experiments with subcooled flow boiling in a rectangular channel.

The first 3 cases are also used by Nabil and Rattner's (Nabil & Rattner, 2016) in order to verify and validate the base solver, iTPCF. Mesh and solver parameters are used directly from their work.

5.2.1 Horizontal Film Condensation (Stefan Problem)

The one-dimensional Stefan problem is a classical benchmark problem for two-phase flow with phase change. It concerns horizontal film condensation on an isothermal subcooled surface. Stagnant vapor at saturation temperature, T_{sat} , condenses to form a liquid film on the top surface of an isothermal plate at wall temperature, T_w . The analytical solution for liquid-vapor interface position (same as the film thickness) is available (Nabil & Rattner, 2016) and is given in Equation (5.12).

$$\delta_{analytical}(t) = \left(2t \left(\frac{k_l}{\rho_l c_{p,l}} \right) \left(\frac{1}{2} + \frac{h_{lv}}{c_{p,l}(T_{sat} - T_w)} \right)^{-1} \right)^{1/2} \quad (5.12)$$

where t is time, δ , k_l , ρ_l and $c_{p,l}$ are film thickness, liquid conductivity, density and specific heat and h_{lv} is latent heat.

The problem domain is given in Fig. 5.1. The analysis is performed with isobutene at 25 °C. The properties of the medium are given in Table 5.1 and analysis properties are given in Table 5.2. The change of the interface location (or growth of the film thickness) compared to the analytical solution is shown in Fig. 5.2. The time-averaged ($t = 0 - 1000$ ms) interface location difference between the current simulation and the analytical result is about 1.9%.

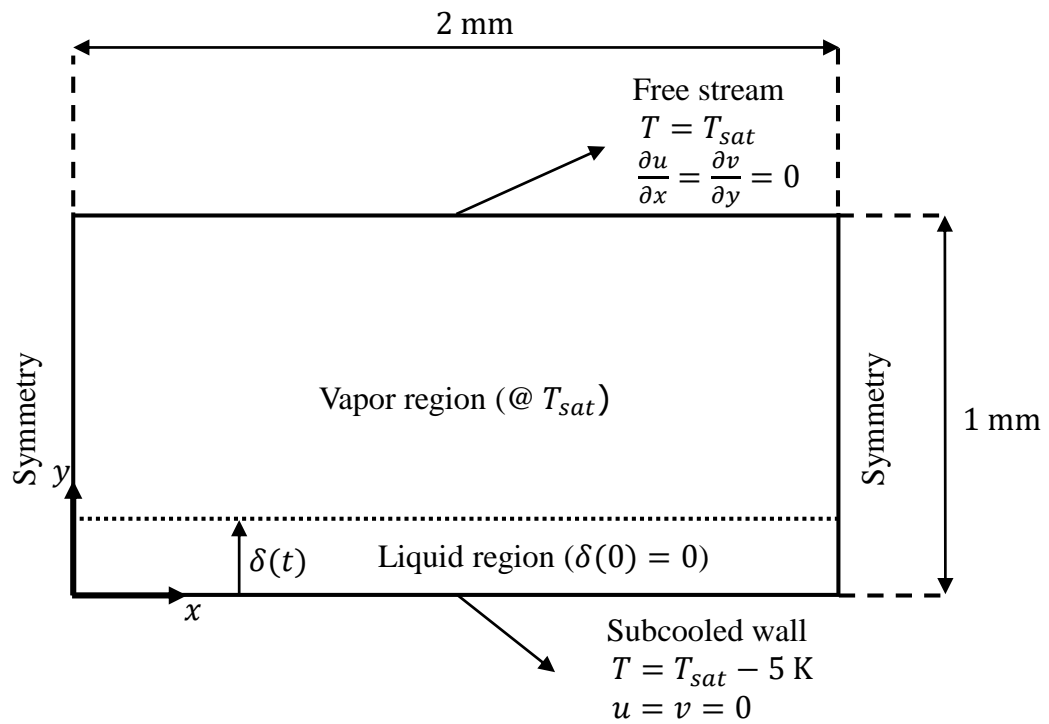


Figure 5.1. Problem domain for horizontal film condensation (Stefan Problem)

Table 5.1. Fluid properties for isobutene at 25 °C

Fluid property	Liquid phase	Vapor phase
Dynamic viscosity (μ , kg/m/s)	1.5×10^{-4}	7.7×10^{-6}
Density (ρ , kg/m ³)	550.6	9.1
Thermal conductivity (k , W/m/K)	0.089	0.017
Specific heat (c_p , kJ/kg/K)	2.45	1.82
Surface tension (σ , kg/s ²)	0.01	
Enthalpy of phase change (h_{LV} , kJ/kg)	329.4	
Saturation temperature (T_{sat} , K)	298	

Table 5.2. Analysis details horizontal film condensation problem

Surface Tension Model	CSF (Brackbill)
Phase Change Model	Empirical Rate Parameter ($r_l = 1, r_v = 1$) & Interface Equilibrium
Time Step	Variable (limited by Courant Number = 0.5)
Mesh Size	$1 \times 220 \times 1$

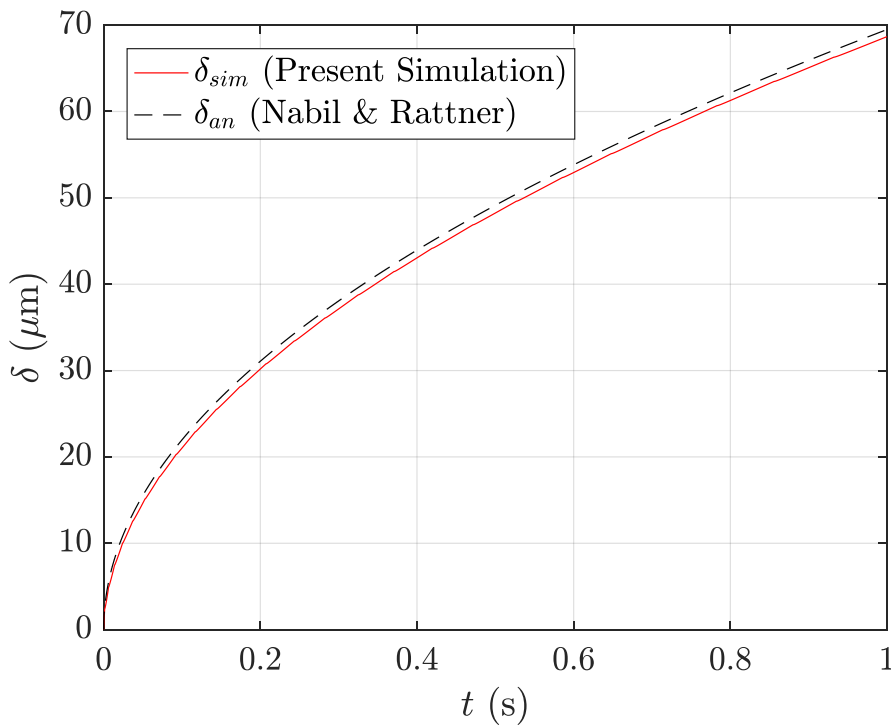


Figure 5.2. Film thickness growth of the Stefan problem

5.2.2 Smooth Falling Film Condensation

The second test problem solved is gravity-driven smooth falling film condensation (Nusselt problem). The simulation domain and boundary conditions are given in Fig. 5.3. A liquid film flows down an isothermal vertical subcooled surface. A 2D geometry with a wall height of 8 mm, and the thickness of the domain is 0.6 mm is

used. A short inlet guide vane (250 μm long) was used to prevent waviness of the inlet film. The film thickness (150 μm) was resolved with 25 cells, and there are 200 cells along the wall.

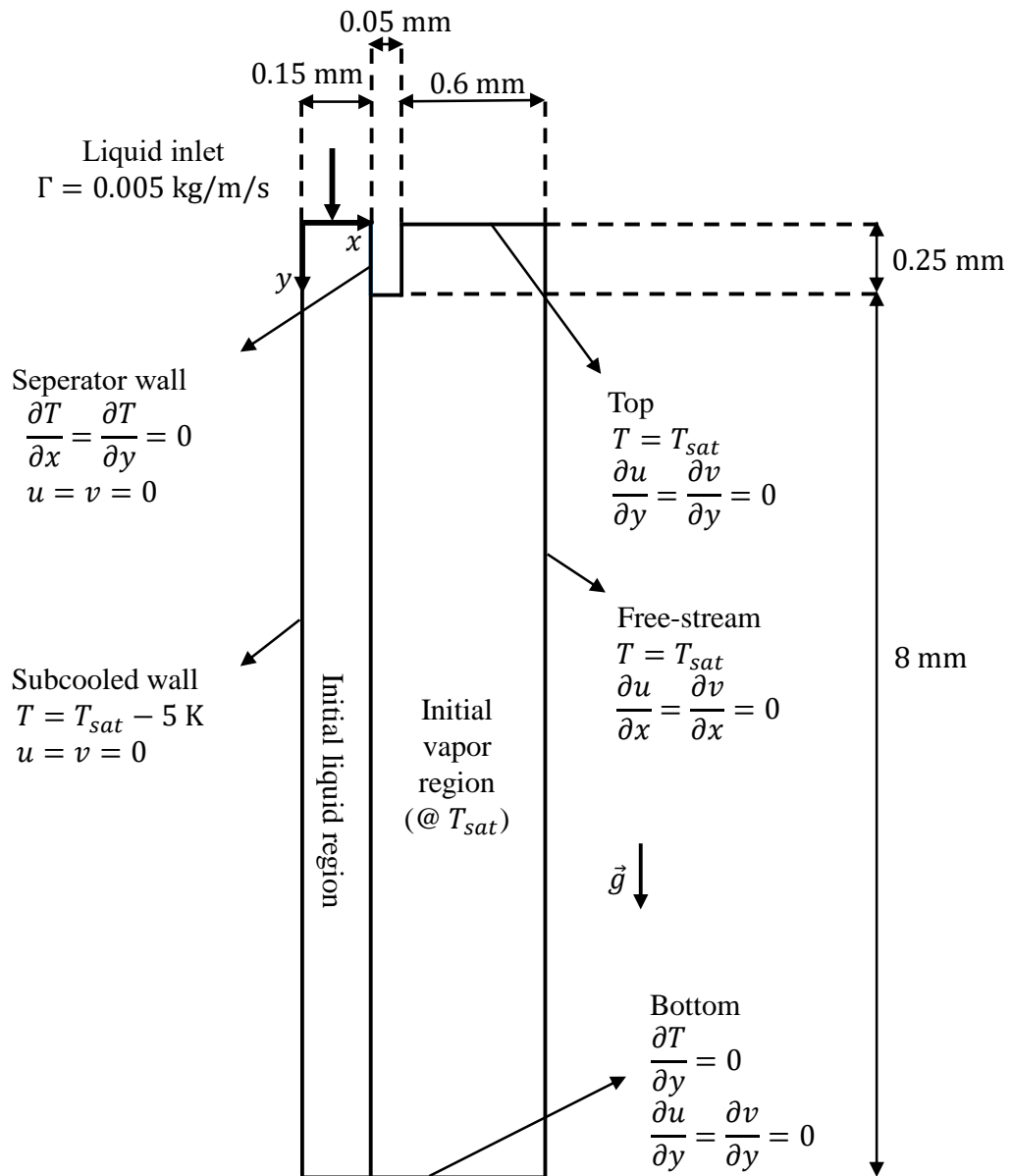


Figure 5.3. Problem domain for smooth falling film condensation (Nusselt Problem)

The simulation is run with a hypothetical fluid with properties given in Table 5.3. Analysis properties are presented in Table 5.4.

Analytical solution for wall heat flux is given below (Nabil & Rattner, 2016).

$$q_{w,an} = \frac{(T_{sat} - T_w)k_L}{\left(\frac{3\mu_L^2}{4\rho_L(\rho_L - \rho_V)g}\right)^{1/3} Re_{f,sim}^{1/3}} \quad (5.13)$$

The time variation of the calculated wall heat flux is shown in Fig. 5.4 in comparison with the analytical solution,. The time-averaged ($t = 0 - 250$ ms) wall heat flux difference of the of two results is 1.7%.

Table 5.3. Fluid properties for the smooth falling film condensation problem

Fluid property	Liquid phase	Vapor phase
Dynamic viscosity (μ , kg/m/s)	5×10^{-4}	2×10^6
Density (ρ , kg/m ³)	500	20
Thermal conductivity (k , W/m/K)	0.5	0.02
Specific heat (c_p , kJ/kg/K)	2.0	1.5
Surface tension (σ , kg/s ²)	0.04	
Enthalpy of phase change (h_{LV} , kJ/kg)	2000	
Saturation temperature (T_{sat} , K)	298	

Table 5.4. Analysis details for the smooth falling film condensation problem

Surface Tension Model	CSF (Brackbill)
Phase Change Model	Empirical Rate Parameter ($r_l = 1, r_v = 1$) & Interface Equilibrium
Time Step	Variable (limited by Courant Number = 0.5)
Mesh Size	$63 \times 413 \times 1$

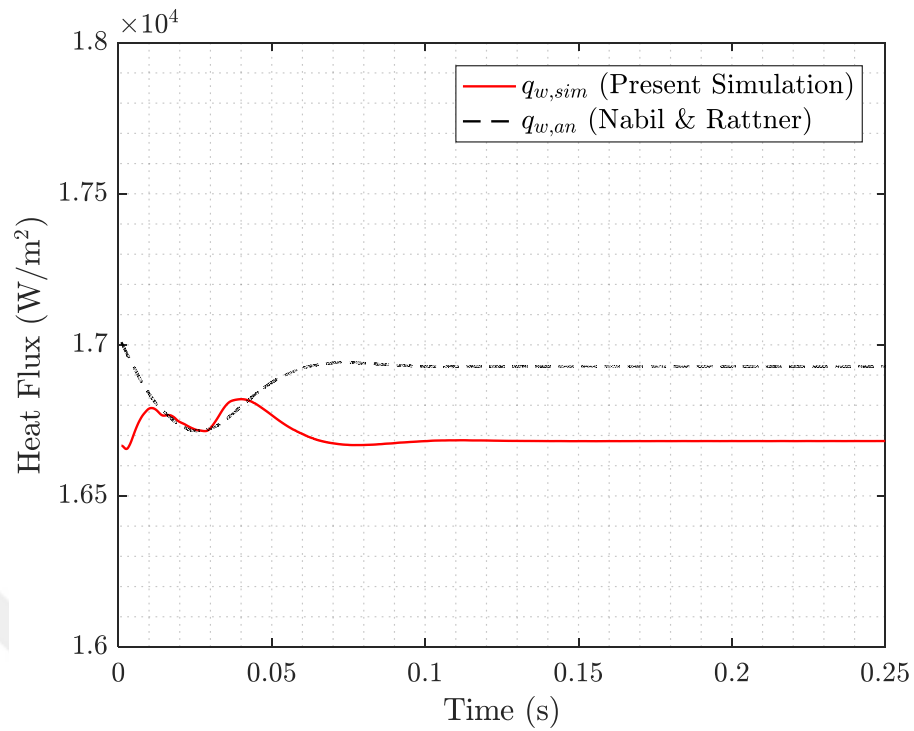


Figure 5.4. Wall heat flux result comparison for the smooth falling film condensation problem

5.2.3 Bubble Condensation

Third problem shows the condensation of a small vapor bubble in a quiescent subcooled liquid environment. The 2D axisymmetric problem domain and boundary conditions are given in Fig. 5.5. A stationary saturated vapor bubble with a diameter of 600 μm is initiated in the middle of the domain. In order for the bubble to condense, the surrounding liquid medium is subcooled by 1 K. In this case, a hypothetical fluid is used as a medium whose properties are given in Table 5.5. Analysis properties are shown in Table 5.6.

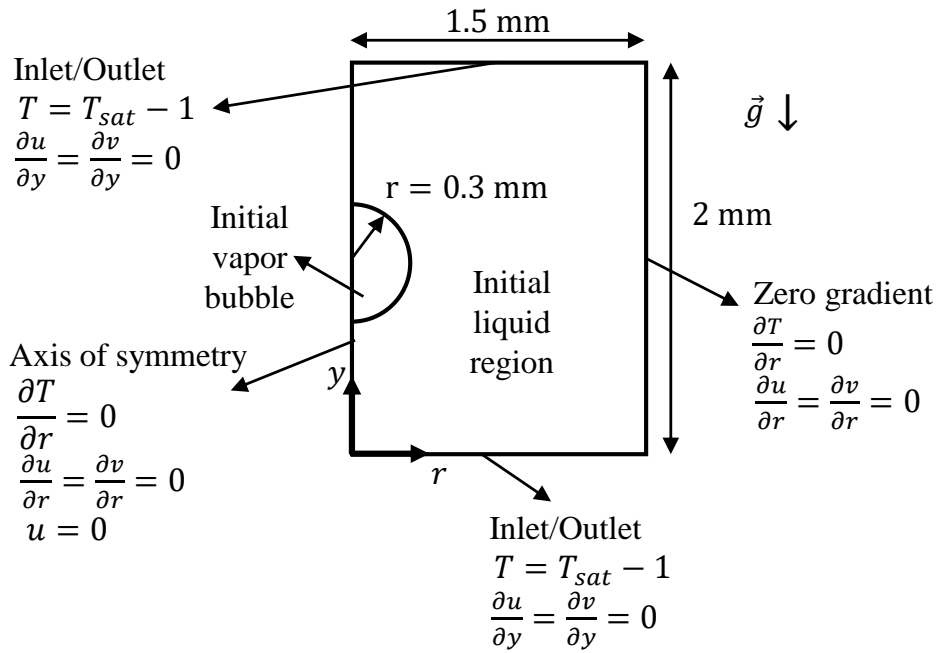


Figure 5.5. Solution domain and boundary conditions that are used for bubble condensation problem in this study

Table 5.5. Fluid properties for bubble condensation problem

Fluid property	Liquid phase	Vapor phase
Dynamic viscosity (μ , kg/m/s)	4.5×10^{-3}	4×10^{-5}
Density (ρ , kg/m ³)	900	10
Thermal conductivity (k , W/m/K)	1.0	0.02
Specific heat (c_p , kJ/kg/K)	2.0	2.5
Surface tension (σ , kg/s ²)	0.005	
Enthalpy of phase change (h_{LV} , kJ/kg)	2000	
Saturation temperature (T_{sat} , K)	100	

Table 5.6. Analysis properties for bubble condensation problem

Surface Tension Model	CSF (Brackbill)
Phase Change Model	Empirical Rate Parameter ($r_l = 1, r_v = 1$) & Interface Equilibrium
Time Step	Variable (limited by Courant Number = 0.5)
Mesh Size	137×224

A comparison of the average heat transfer coefficient, h_{pc} calculated by the current simulation and an analytical method (Ranz & Marshall, 1952) can be seen in Fig. 5.6. h_{pc} is calculated as follows

$$h_{pc} = \frac{Q_{pc}}{A_{pc}\Delta T} \quad (5.14)$$

using the heat transfer rate due to phase change, Q_{pc} , surface area of the bubble, A_{bub} , and the temperature difference between liquid and vapor phases ($\Delta T = 1$ K). Q_{pc} and A_{bub} are extracted by user-defined scripts from OpenFOAM at each time step. Due to the initial zero-thickness thermal boundary layer, there is an unphysical, high heat flux before 50 ms. After the thermal boundary layer settles, the results show good agreement. Excluding the first 50 ms of the simulation, the time-averaged ($t = 50 - 320$ ms) absolute deviation of the heat flux coefficient of the current simulation and the analytical result is 8%.

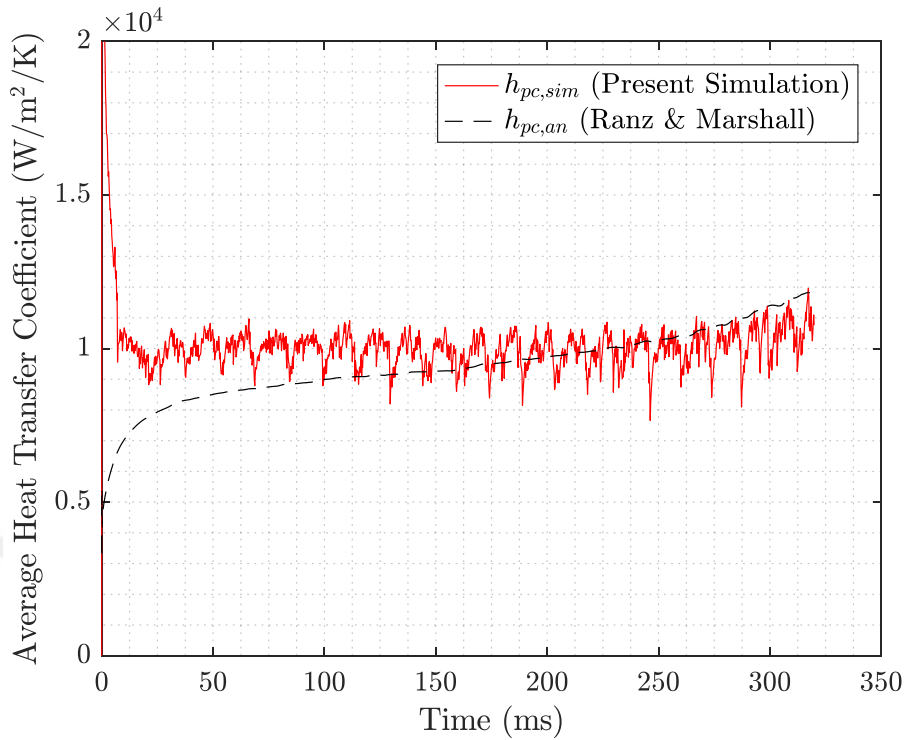


Figure 5.6. Heat transfer coefficient comparison for the bubble condensation problem (Ranz & Marshall, 1952)

5.2.4 Rising Bubble Problem

This problem is used to test the performance of the adaptive mesh refinement (AMR) capabilities of the developed solver. A single bubble rises with buoyancy forces in a liquid as shown in Fig. 5.7. The domain size and bubble location are taken from Hysing et al. (2009). The terminal shapes of a single rising bubble under a range of Reynolds (Re), Eötvös (EO , also known as Bond number, Bo) and Morton (Mo) numbers were observed and reported in a study by Bhaga and Weber (1981). The definitions of these non-dimensional numbers are given below. U_∞ denotes the bubble terminal rise velocity. Since its value was unknown before the calculations, a new Reynolds Number, Re^* was defined to eliminate U_∞ .

$$Re = \frac{\rho_{liquid} D U_{\infty}}{\mu_{liquid}} \quad (5.15)$$

$$Re^* = \frac{\rho_{liquid} g^{1/2} D^{3/2}}{\mu_{liquid}} \quad (5.16)$$

$$Eo = \frac{\rho_{liquid} g D^2}{\sigma} \quad (5.17)$$

$$Mo = \frac{g \mu_{liquid}^4}{\rho_{liquid} \sigma^3} \quad (5.18)$$

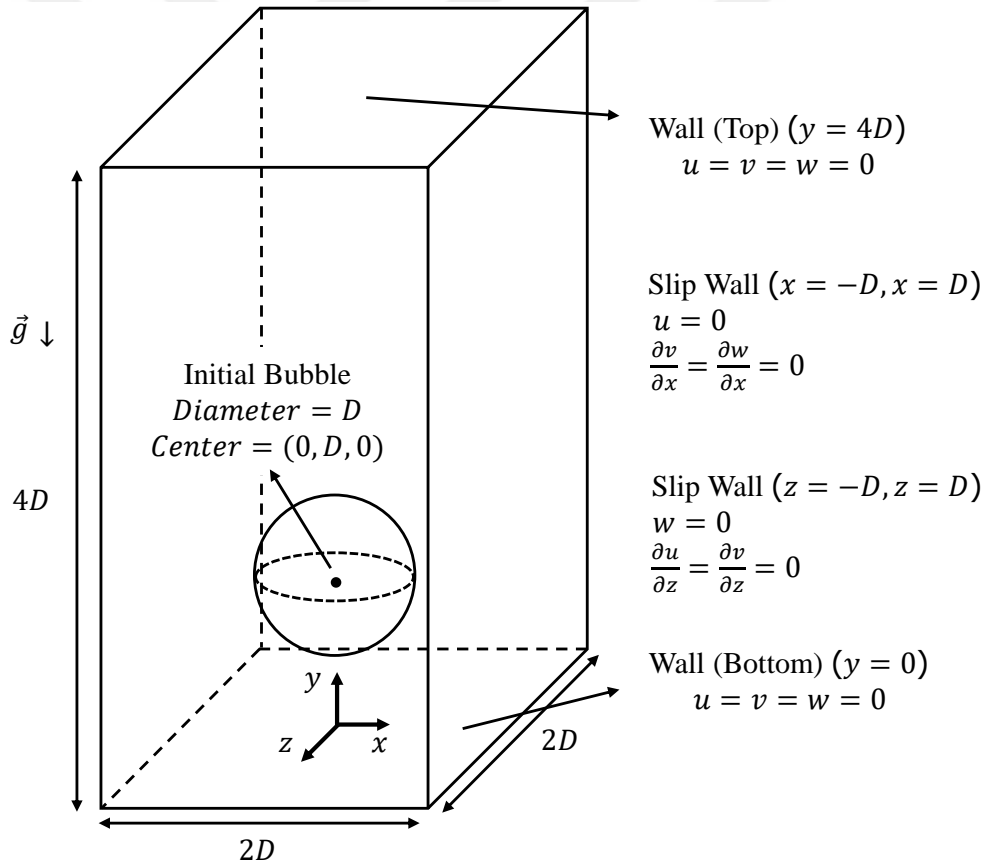


Figure 5.7. Solution domain and boundary conditions for the rising bubble problem

Various bubble shapes (spherical, oblate ellipsoid, disk-like, oblate ellipsoidal cap, skirt bubble, and spherical-cap) were found in various flow regimes investigated experimentally by Bhaga and Weber (1981). The current simulations were performed with hypothetical fluids with the properties given in Table 5.7 for two different cases. For the Case-1 and Case-2, oblate ellipsoid and oblate ellipsoidal cap type terminal bubbles shapes are expected.

Table 5.7. Fluid properties, physical properties and dimensionless numbers for the rising bubble problem

	Case-1		Case-2	
	Liquid	Vapor	Liquid	Vapor
Dynamic viscosity (μ , kg/m/s)	10	1	10	0.1
Density (ρ , kg/m ³)	1000	100	1000	1
Thermal conductivity (k , W/m/K)	1.0	0.02	1.0	0.02
Specific heat (c_p , kJ/kg/K)	2.0	2.5	2.0	2.5
Surface tension (σ , kg/s ²)	24.5		1.96	
Enthalpy of phase change (h_{LV} , kJ/kg)	2000		2000	
Saturation temperature (T_{sat} , K)	373		373	
Bubble diameter (D , m)	0.5		0.5	
Re^*	35		35	
Eo	10		125	

The initial mesh used has 40, 80 and 40 cells along the x , y and z directions respectively, which is the coarsest mesh used by Hysing et al. (2009). AMR is applied based on the volume fraction field, α at each time step. The upper and lower limits for applying refinement are $\alpha = 0.9$ and $\alpha = 0.1$, respectively (i.e. mesh is refined when α is between these values.). The maximum refinement level is limited to 1, i.e. AMR divides 1 hexahedral cell into at most 8 hexahedral cells.

Figure 5.8 compares the final shape of the rising bubble at $t = 3$ s using the uniform grid and the AMR grid with the reference 2D numerical study (Hysing et al., 2009) for Case-1. Both the uniform grid and grid with AMR can accurately predict the final oblate ellipsoid shape, however, the interface of the uniform grid is more diffused.

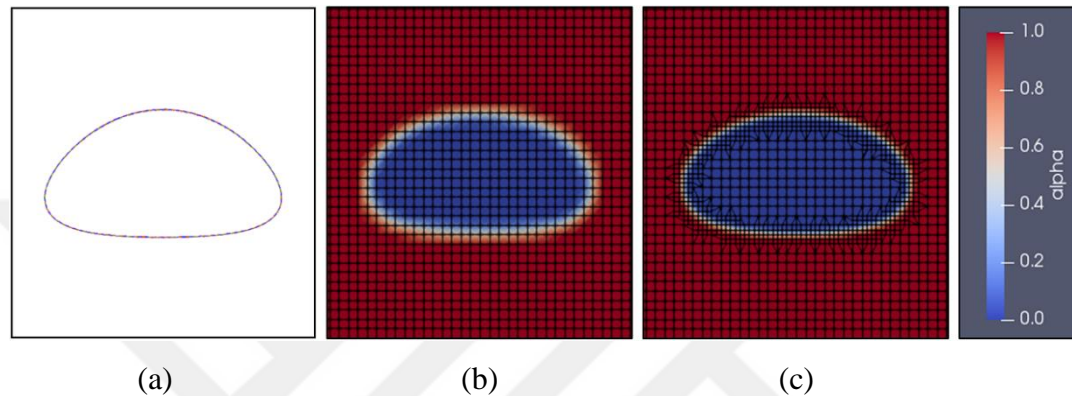


Figure 5.8. Comparison of final shapes of the bubble for Case-1, (a) reference 2D simulation by Hysing et al. (2009), (b) current 3D simulation on $z = 0$ plane, (c) current 3D simulation with AMR on $z = 0$ plane (alpha indicates the phase, alpha=1 is pure liquid and alpha=0 is pure vapor)

A comparison of the final shapes of the rising bubble with an experimental study for Case-2 is presented in Fig. 5.9. In contrast to the dimpled ellipsoidal cap obtained by Bhaga and Weber (1981) in their experiments, the uniform grid results in a final bubble shape with a large skirt. Due to diffusion, break up cannot occur in the solution with uniform mesh. The solution with AMR predicts the bubble shape better and the interface more sharply. It also accurately predicts the break ups mentioned by Hysing et al. (2009).

Another comparison of the final shapes of the rising bubble for Case-2 with 2D (Hysing et al., 2009) and 3D numerical studies (Hua & Lou, 2007) is presented in Fig. 5.10. The 2D reference simulation has a narrower shape compared to the current

simulation, on the other hand, the 3D reference study has a wider shape and a longer skirt. Similar to the current study, the 2D simulation predicted break ups.

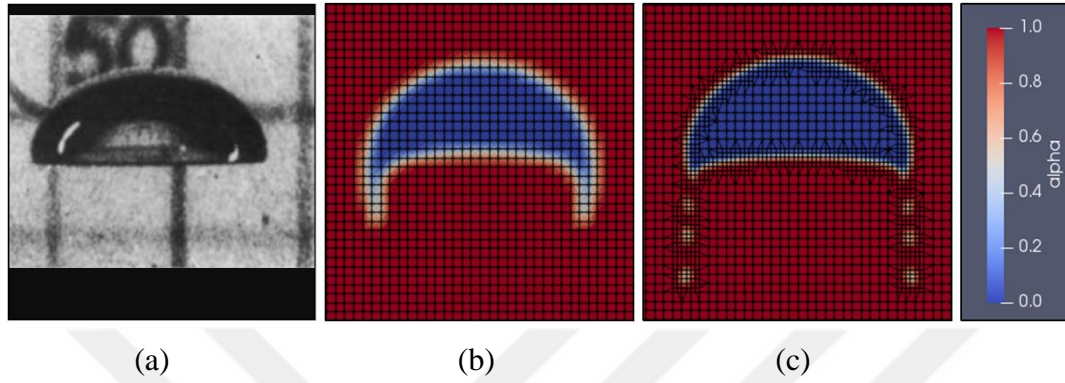


Figure 5.9. Comparison of final shapes of the bubble for Case-2, (a) experimental result by Bhaga and Weber (1981), (b) current 3D simulation on $z = 0$ plane (c) current 3D simulation with AMR on $z = 0$ plane

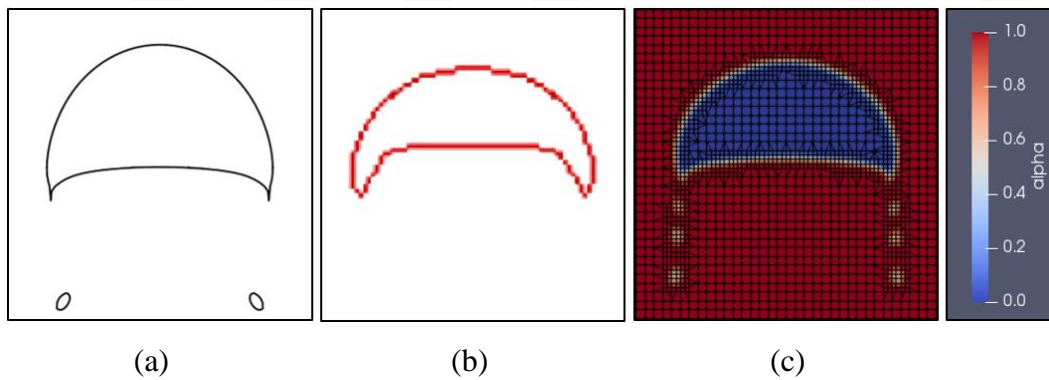


Figure 5.10. Comparison of final shapes of the bubble for Case-2, (a) reference 2D simulation by Hysing et al. (2009), (b) reference 3D simulation by Hua and Lou (2007), (c) current 3D simulation on $z = 0$ plane

As can be seen in Table 5.8, the terminal velocity of the bubble at $t = 3$ s for Case-1 are 8.7% and 3.6% higher than the reference numerical study for the uniform and AMR grid, respectively. The differences can be mainly attributed to the fact that

current solutions are 3D while the reference result is 2D. The terminal velocity of the bubble for Case-2 are 14.8% and 6.3% lower than the reference experimental study for the uniform and AMR grid, respectively. Hua and Lou (2007) also numerically solved the same problem in 3D. They reported that the number of cells in the grid and the domain size are important in accurately predicting the terminal velocity and showed that under-resolved meshes result in lower terminal velocities.

Table 5.8. Comparison of terminal velocities of the rising bubble problem

	Reference Experimental Study	Reference Numerical Study	Current Study (Uniform Grid)	Current Study (AMR Grid)
Case-1	-	0.195 m/s **	0.212 m/s	0.202 m/s
Case-2	0.432 m/s *	0.421 m/s ***	0.368 m/s	0.405 m/s

* Bhaga & Weber (1981)

** Hysing et al. (2009)

*** Hua & Lou (2007)

The development of the bubble shape of Case-2 is showed in Figure 5.11 using the $\alpha = 0.5$ isosurface.

Rising bubble problem (Case-2) was also solved with STAR-CCM+ with the default VOF and AMR settings (“Free Surface Mesh Refinement”). The maximum refinement level was limited to 1 in order to allow a fair comparison of the available results. Figure 5.12 shows the final shape of the rising bubble. The results obtained with different solvers are similar for the use of both uniform and AMR grids. All simulations correctly predict the final oblate ellipsoid shape, however, the interfaces of the uniform grids are more diffused for both solvers. In contrast to OpenFOAM’s large skirted final bubble shape, STAR-CCM+ anticipates a very diffused tail with a uniform grid. A sharp interface is obtained using AMR with STAR-CCM+, but it fails to predict the break ups.

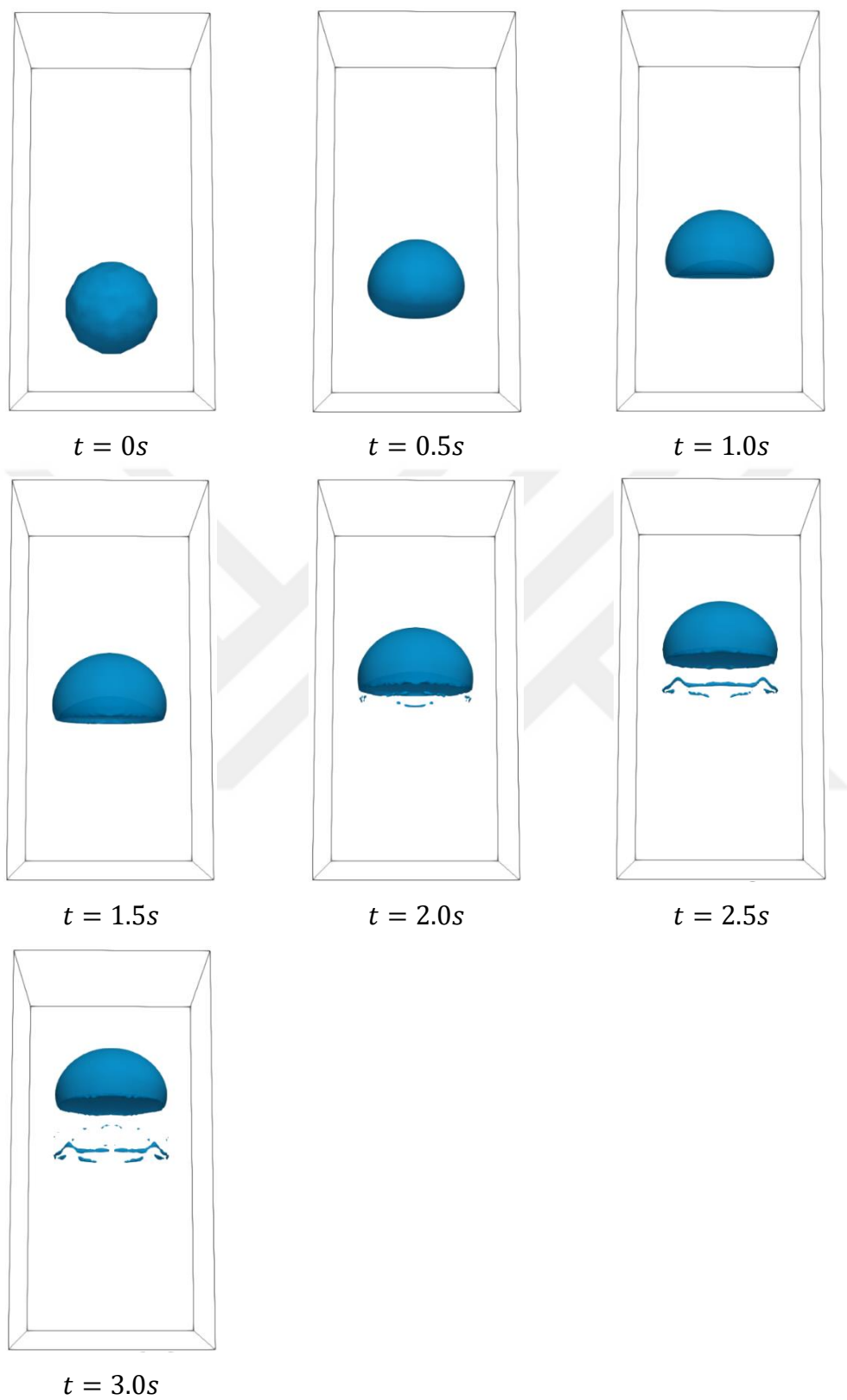


Figure 5.11. Bubble shape development for Case-2 of the rising bubble problem

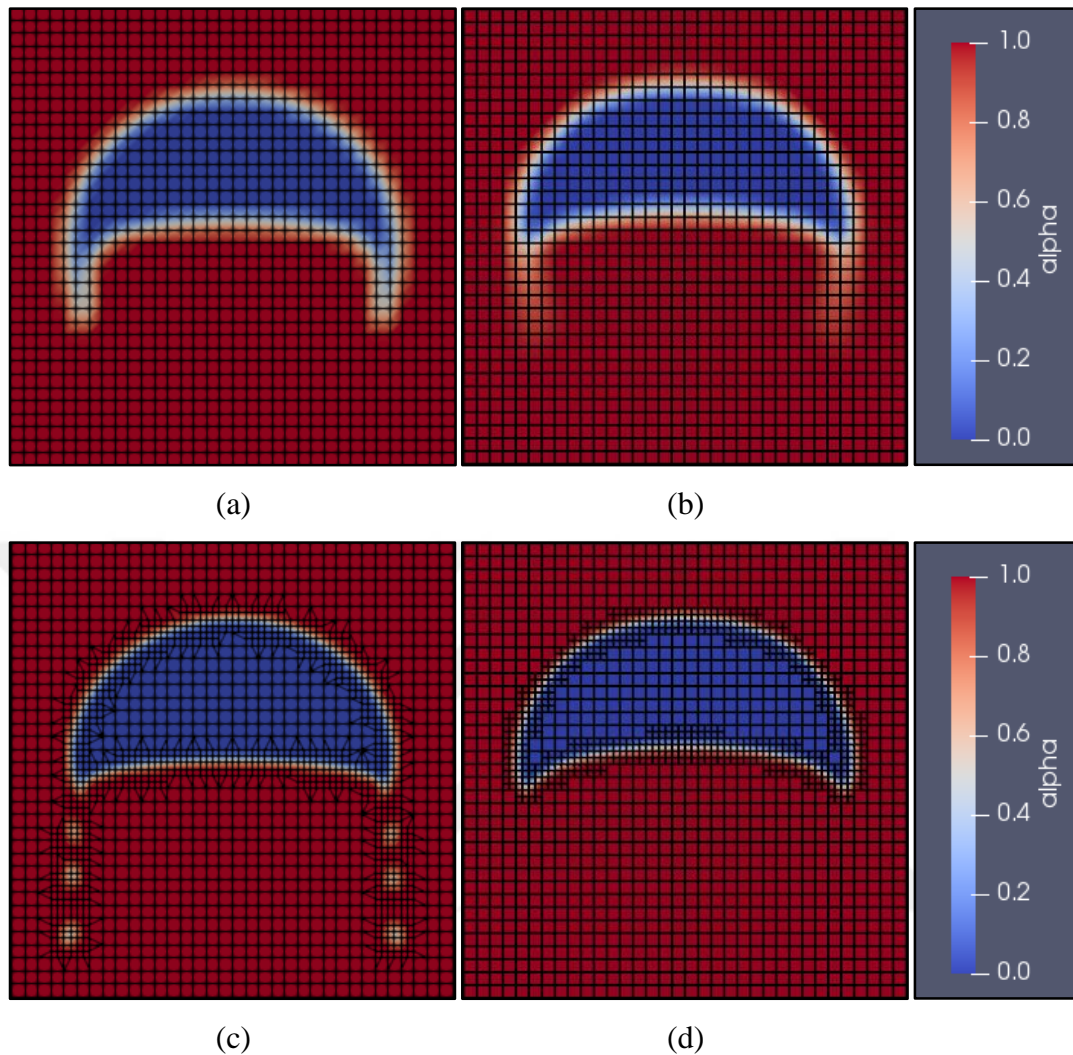


Figure 5.12. Comparison of final shapes of the bubble on $z = 0$ plane for the Case-2 , (a) current 3D OpenFOAM simulation with uniform mesh, (b) current 3D STAR-CCM+ simulation with uniform mesh, (c) current 3D OpenFOAM simulation with AMR and (d) current 3D STAR-CCM+ simulation with AMR

As can be seen in Table 5.9, the terminal velocities (STAR-CCM+) of bubbles for Case-2 are 7.4% and 6.9% lower than the reference study (Bhaga & Weber, 1981) for uniform and AMR grid, respectively. It can be said that STAR-CCM+ predicts bubble terminal velocity better than OpenFOAM for the uniform grid.

The performance of the three simulations, two using uniform grids and one using an AMR grid, in terms of both accuracy and run time are compared in Table 5.10.

Compared to the coarse uniform grid, the AMR grid has 1.34 times more cells at the end of the simulation. The AMR grid calculations took 2.1 times more time compared to using uniform coarse grid, while calculating the terminal velocity with considerably higher accuracy. Compared to the uniform fine grid, which uses 8 times more cells than the uniform coarse one, the AMR grid results are only slightly different and take 5.7 times less time. These results demonstrate the effectiveness of the AMR technique.

Table 5.9. Terminal velocities of rising bubble (Case-2) with STAR-CCM+

Reference Study	Uniform Grid	AMR Grid
0.432 m/s *	0.400 m/s	0.402 m/s

* taken from Bhaga's work (Bhaga & Weber, 1981)

Table 5.10. Performance comparison of uniform and AMR grids for Case-2

	Coarse Grid	AMR Grid	Fine Uniform
Grid	40 × 80 × 40	40 × 80 × 40 + AMR	80 × 160 × 80
# of Cells	128,000	171,200*	1,024,000
Run Time**	9 minutes	19 minutes	108 minutes
Terminal Velocity	0.368 m/s	0.405 m/s	0.412 m/s
Error in Terminal Velocity***	14.8%	6.3%	5.5%

*At the end of the simulation.

**Intel(R) Xeon(R) CPU E3-1535M v6 @ 3.10GHz x 8

***Compared to the reference experimental study of Hysing et al. (2009)

5.2.5 Subcooled Flow Boiling in a Rectangular Channel

This experimental validation case, sketched in Fig. 5.13, is taken from Liu et al. (2005). There are 25 parallel-cut mini-channels measured 275 μm in width (w_c), 636 μm in height (H_c) and 25.4 mm in length (L_c). The top of the channels was covered by a viewing window and therefore assumed to be adiabatic. Only one of the 25 channels is considered for the current analysis. The boundary conditions for the analysis are shown in Fig. 5.14. Unlike the test case, the solid part is not considered in the analysis, so the heat fluxes in the side and bottom walls are calculated from the heat flux given for the base area of the copper block. Both Liu et al. (2005) and Özdemir (2016) stated that uniform heat flux can be assumed along the channel surfaces (bottom and side walls). The properties of the water used in this simulation are given in Table 5.11.

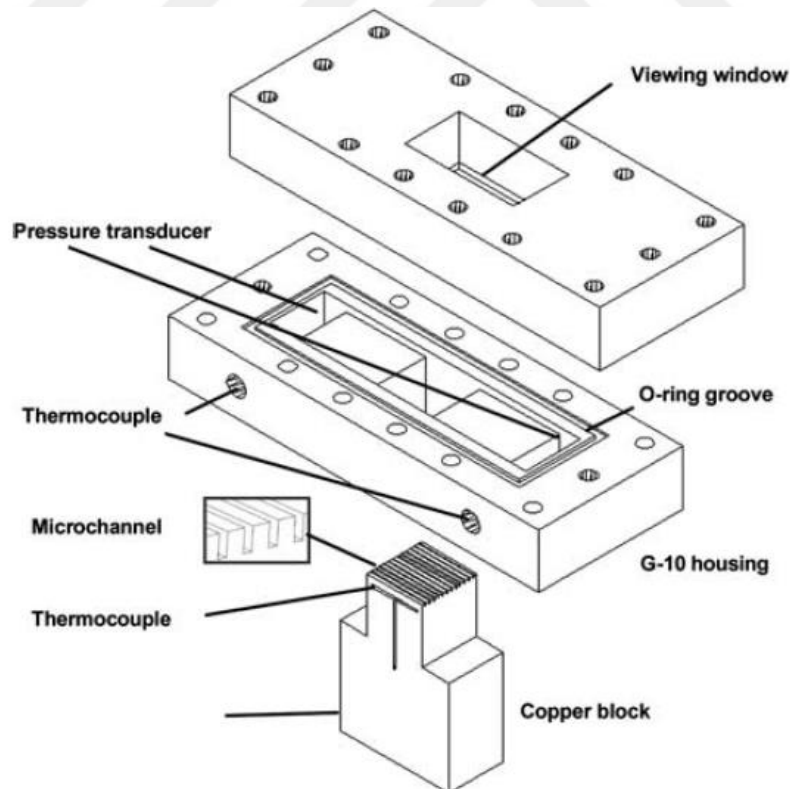


Figure 5.13. 3-D view of mini-channel test section (Liu et al., 2005)

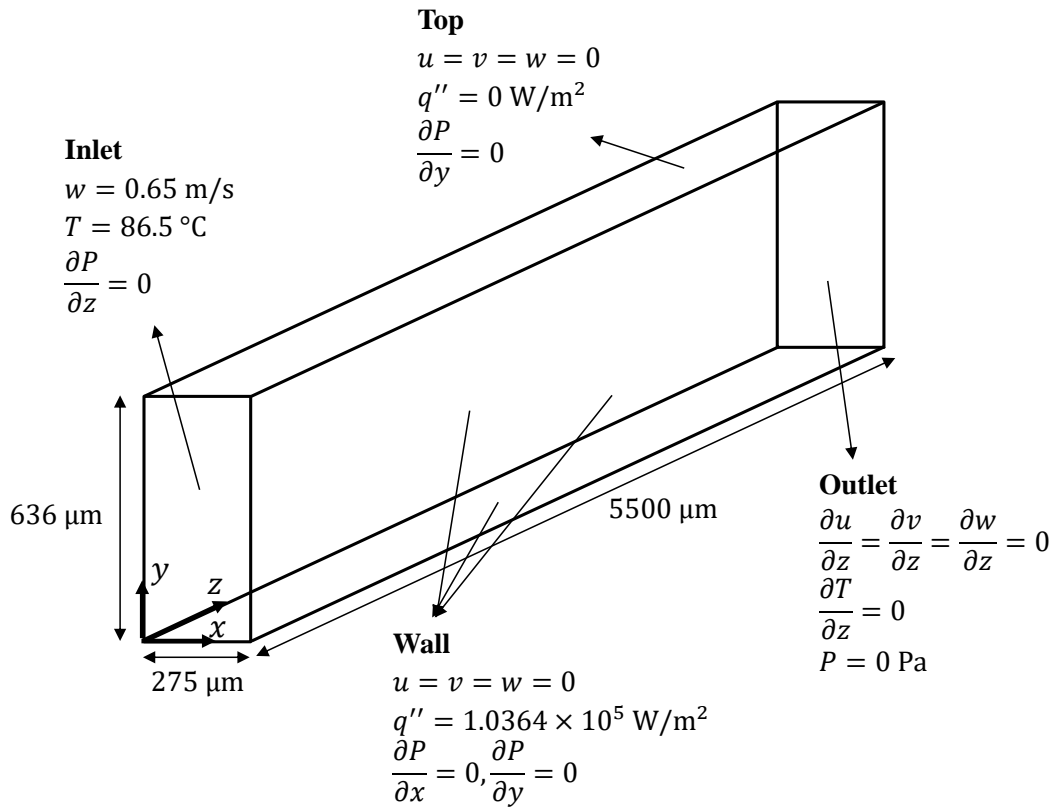


Figure 5.14. Domain and boundary conditions for flow boiling analyses

Table 5.11. Water properties for subcooled flow boiling in rectangular channel

Fluid property	Liquid phase	Vapor phase
Dynamic viscosity (μ , kg/m/s)	2.8×10^{-4}	1.2×10^{-5}
Density (ρ , kg/m ³)	958.4	0.59
Thermal conductivity (k , W/m/K)	0.677	2.0
Specific heat (c_p , kJ/kg/K)	4.2	2.0
Surface tension (σ , kg/s ²)	0.043	
Enthalpy of phase change (h_{LV} , kJ/kg)	2258	
Saturation temperature (T_{sat} , K)	373.15	

In this problem, nucleate boiling is expected at the bottom wall, especially at its edges. Zhuan and Wang (2010) studied this problem with uniform grids with element

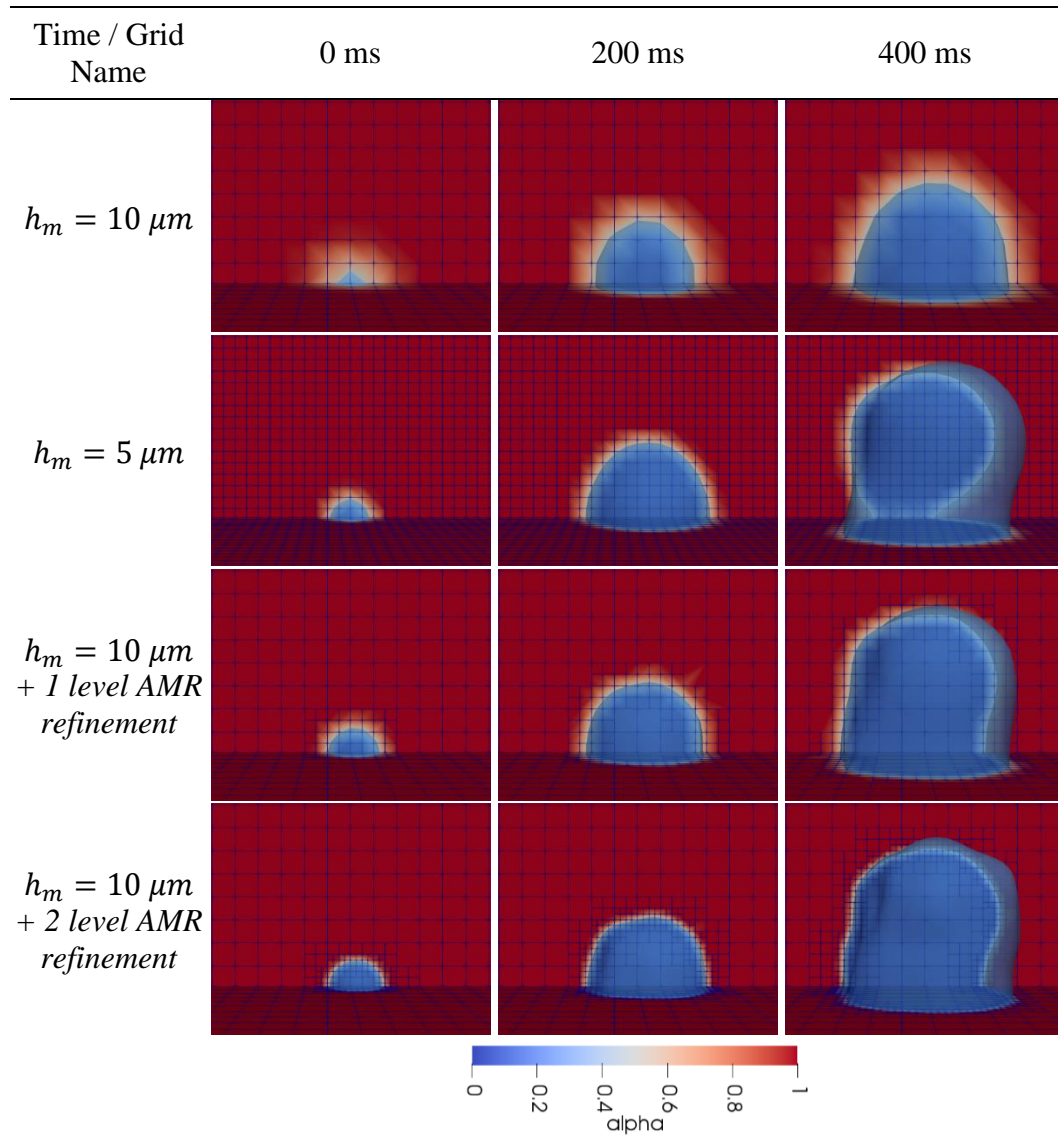
edge lengths (h_m) of 15 μm and 20 μm . These grids led to errors of up to 35% in the bubble radius. Using refined regions with element sizes (h_m) of 5 μm and 2 μm , they were able to reduce errors down to 18% and 5%, respectively. As can be seen in Fig. 5.14, only the first 5.5 mm of the channel geometry was solved in order to reduce the simulation time. This length is sufficient to observe bubbles (Zhuan & Wang, 2010). In the current simulations, two uniform hexahedral meshes with element edge lengths (h_m) of 10 μm and 5 μm and the two AMR grids based on a uniform mesh with $h_m = 10 \mu\text{m}$ were used. One of the AMR grids is allowed to refine grids by one level which means h_m is locally reduced to 5 μm , and the other one is allowed to refine grids by two levels, which means that h_m is locally decreased to 2.5 μm . The AMR methodology uses volume fraction (α) as a criteria for mesh refinement at each time step. $\alpha = 0$ and $\alpha = 1$ represent completely vapor and completely liquid cells. The range $0 < \alpha < 1$ represents a cell filled with both vapor and liquid phases, i.e. the interface region between the phases. Cells are refined when α is between 0.1 and 0.9. When α is less than 0.1 or greater than 0.9, cells are coarsened.

In order to model surface tension, the continuous surface force method (CSF) (Brackbill et al., 1992), which is the default model in OpenFOAM, is used. Lee's (Lee, 2013) empirical rate parameters were employed for mass transfer modeling. The tuning coefficients for boiling and condensation, r_l and r_v , were both set to 1 for the first set of analyses. Unfortunately, the interface equilibrium model cannot be applied to this problem because it cannot start the initial nucleation. The time step is variable and limited to the Courant Number of 0.5 which is same for all the validation and verification analyses.

Approximately 50 ms after the start of the analysis, the first bubble with a radius of 10 μm appears near the exit at the bottom wall edge, as expected (Özdemir, 2016). The sharp edges of the rectangular channel enhance nucleation and behave as effective nucleation sites. After the first bubble with a radius of 10 μm was detected, the analyses are continued for another 400 ms, during which time the growth trend

of the bubbles is monitored. In order to calculate the bubble radius, the bubble boundary with a vapor volume fraction (α) of 0.5 was determined. Table 5.12 shows the effect of grid on bubble shape in different simulation time. $h_m = 10 \mu m$ grid cannot resolve and wrongly predicted the bubble shape. The other three grids similar bubble shapes and predict a developing neck at the base of the bubble at 400 ms.

Table 5.12. Comparison of bubble growth and resulting grids of uniform and AMR grids at simulation physical times of 0, 200 and 400 ms ($alpha = 1$ is pure liquid, $alpha = 0$ is pure vapor, the bubble boundary is $alpha = 0.5$)



A comparison of the bubble growth with reference studies is given in Fig. 5.15. As can be seen in Fig. 5.15, the trends of the current simulation, reference experiment and reference simulation are similar for the first 100 ms, after which the current simulation using a uniform grid with $h_m = 10 \mu\text{m}$ predicts smaller bubble radius values. The same deviation trend was also reported by Zhuan and Wang (2010) with meshes of $h_m = 15 \mu\text{m}$ and $h_m = 20 \mu\text{m}$, but results for these meshes are not reported. For locally refined grids with $h_m = 5 \mu\text{m}$, the bubble radius values after 250 ms had the signs of deviation mentioned above. Decreasing the element edge lengths (h_m) locally to $2 \mu\text{m}$ in Zhuan and Wang's (2010) study provided very good agreement with experimental results (Liu et al., 2005).

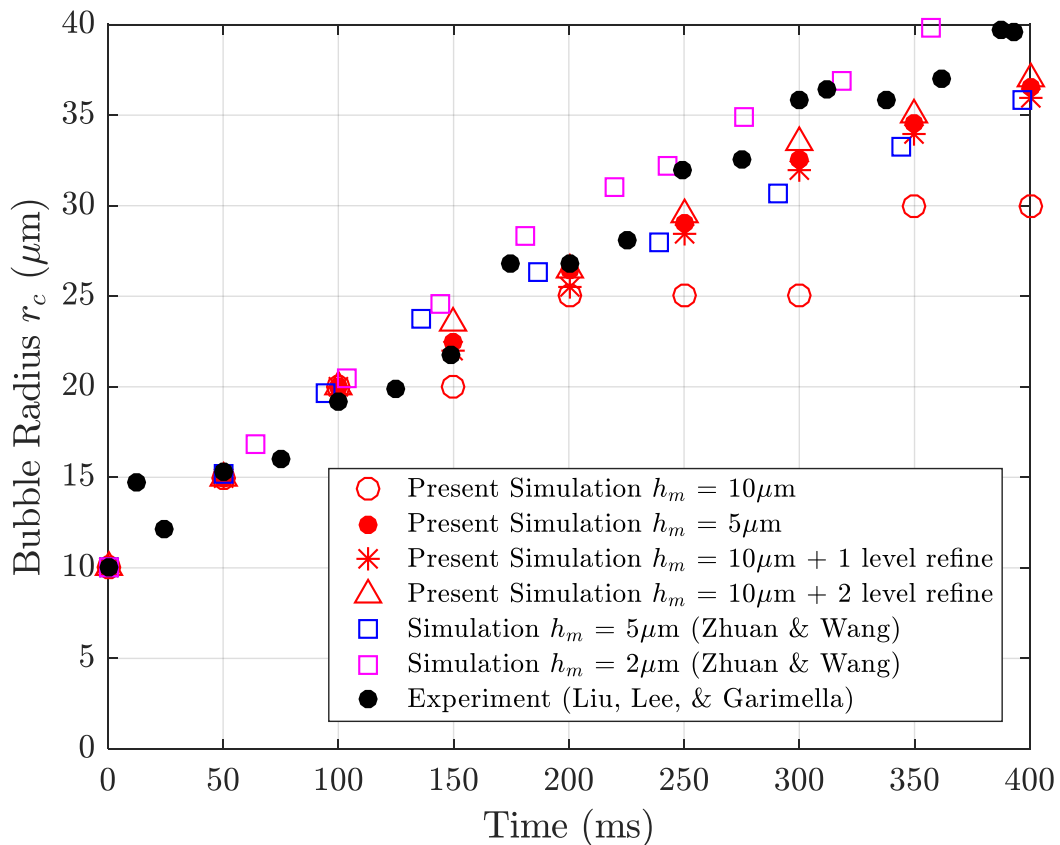


Figure 5.15. Comparison of the bubble growth with reference experimental (Liu et al., 2005) and numerical (Zhuan & Wang, 2010) studies

For the current simulations, other than uniform grid with $h_m = 10 \mu\text{m}$, all three grids predict similar bubble growth trends as can be seen in Figure 5.15. It can be said that decreasing h_m value below $5 \mu\text{m}$ doesn't significantly affect the result. Current results are in good agreement with the experiment and Zhuan and Wang's locally refined grids with $h_m = 5 \mu\text{m}$. However, there is a 10% difference with the experimental value at the end of simulation.

The computational performances of the 4 grids used in the current simulations are compared in Table 5.13. The AMR with 1 level of refinement takes only 2.1 times the analysis time of the uniform coarse grid ($h_m = 10 \mu\text{m}$), while the uniform fine grid ($h_m = 5 \mu\text{m}$) takes 11 times. Even the AMR with 2-level of refinement takes 4.4 times the duration of the uniform coarse grid. The 1 and 2-level AMR refinement causes only a 2% and 9% increase in the base number of grids, on the other hand, the fine uniform mesh has 8 times more grids compared the coarse grid. These results demonstrate the effectiveness of the AMR technique for this problem.

Table 5.13. Computational performance comparison of uniform and AMR grids

Grid Name	$h_m = 10 \mu\text{m}$	$h_m = 5 \mu\text{m}$	$h_m = 10 \mu\text{m}$ + 1 level AMR refinement	$h_m = 10 \mu\text{m}$ + 2 level AMR refinement
Base Grid	28×64 $\times 550$	56×128 $\times 1100$	28×64 $\times 550$	28×64 $\times 550$
# of Cells	985,600	7,884,800	1,004,900*	1,077,200*
Run Time**	28 hours	310 hours	58 hours	123 hours

*Maximum value during refinement

**Using Intel(R) Xeon(R) 6258R 2.70 Ghz x 56 Cores (TRUBA)

In the second set of analyses, the tuning coefficients for boiling and condensation mass transfer, r_l and r_v were examined. The analyses were performed with the AMR grid with 1 level of refinement because it is best one when computational performance and accuracy are taken into consideration. Figure 5.16 shows the effect of 4 different mass transfer model coefficients (r_l and r_v) on bubble growth. Using $r_l = r_v = 2$, a very good agreement with the experimental data is achieved. $r_l = r_v = 4$ and $r_l = r_v = 8$ both predicted higher bubble radius values than expected.

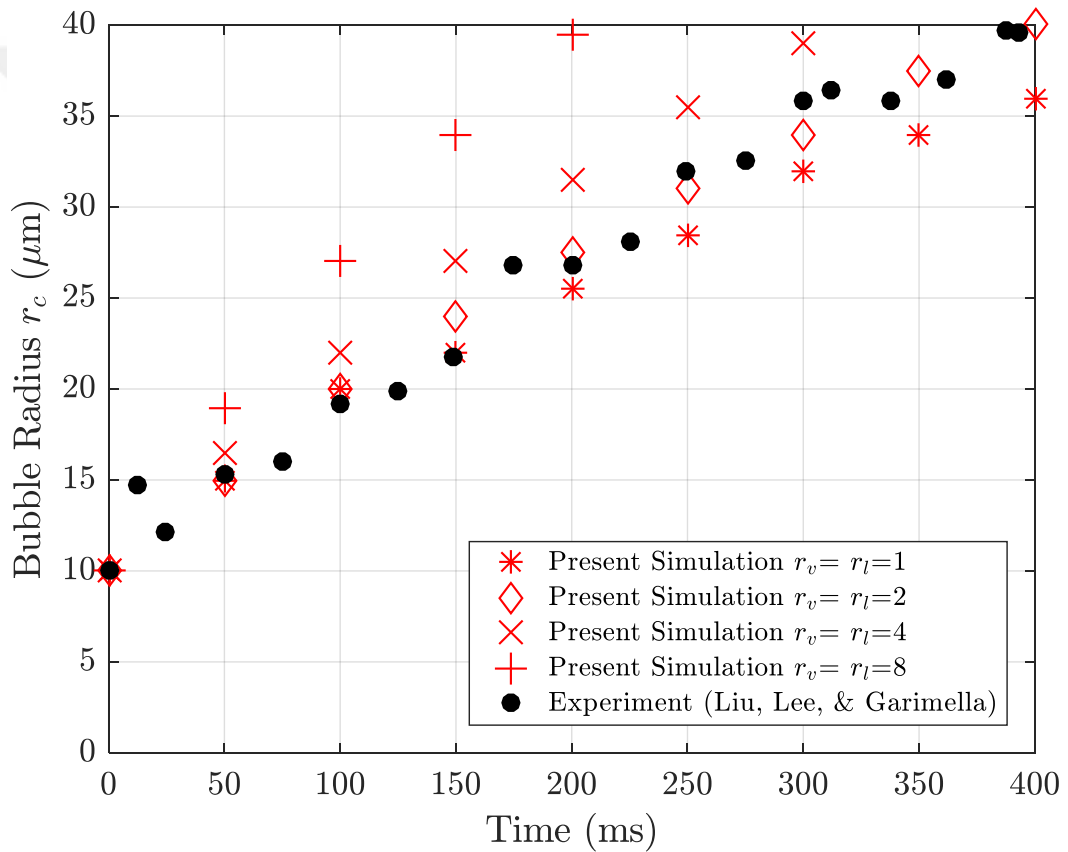


Figure 5.16. Effect of mass transfer model coefficients ($r_l = r_v = 1, 2, 4, 8$) on bubble growth

5.2.6 Comparison with Current Experiments

Lastly, experimental data obtained by the current study is used to validate the solver. Test-7 which is one of the experiments with subcooled flow boiling, is chosen for this purpose. Details of this case can be found in CHAPTER 3. The boundary conditions for the analysis are shown in Fig. 5.17. The properties of the water used in this simulation are given in Table 5.11. The flow is modelled as laminar. The analysis is run for 400 ms, and all the results presented reflect the last time step.

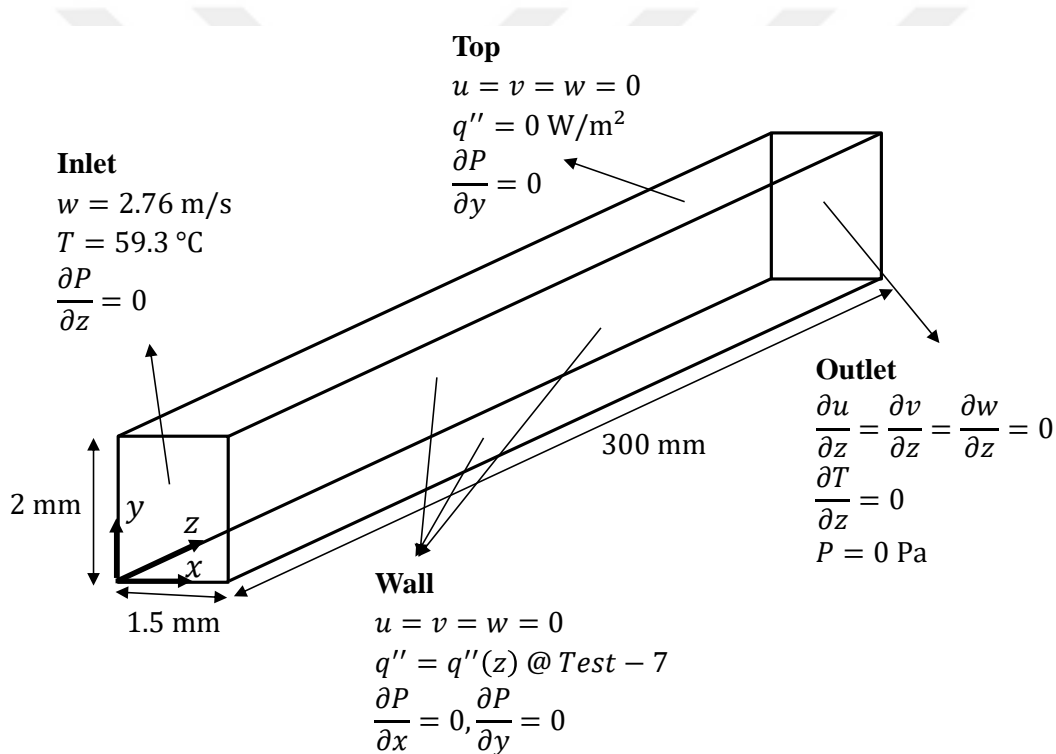


Figure 5.17. Domain and boundary conditions for the simulation of Test-7

An AMR grid with 2 level refinement is used for the current analysis. Base grids element edge length (h_m) is $20 \mu\text{m}$. By using 2 level refinement, h_m is locally reduced to $5 \mu\text{m}$ which is determined from the previous validation case (Section 5.2.5). The AMR is applied based on the volume fraction field, α , at each time step Mesh is adopted when α is between 0.1 and 0.9.

Lee's (Lee, 2013) empirical rate parameters were employed for mass transfer modeling. The tuning coefficients for boiling and condensation, r_l and r_v , were both set to 2 which gave the correct bubble growth in Section 5.2.5. In order to model surface tension, the continuous surface force method (CSF) (Brackbill et al., 1992), which is the default model in OpenFOAM, is used. The time step is variable and limited to the Courant Number of 0.5, which is same for all the validation and verification analyses.

Experimental data and coolant bottom wall temperatures ($x = 0.75$ mm line) are compared in Fig. 5.18. The calculated wall temperatures are in good agreement with the test data. The average bubble radius for every 20 mm is also shown in the Figure 5.19. It can be seen that after 250 mm from inlet, bubble radius is started to shrink as expected because of the reduced heat transfer rate near the exit.

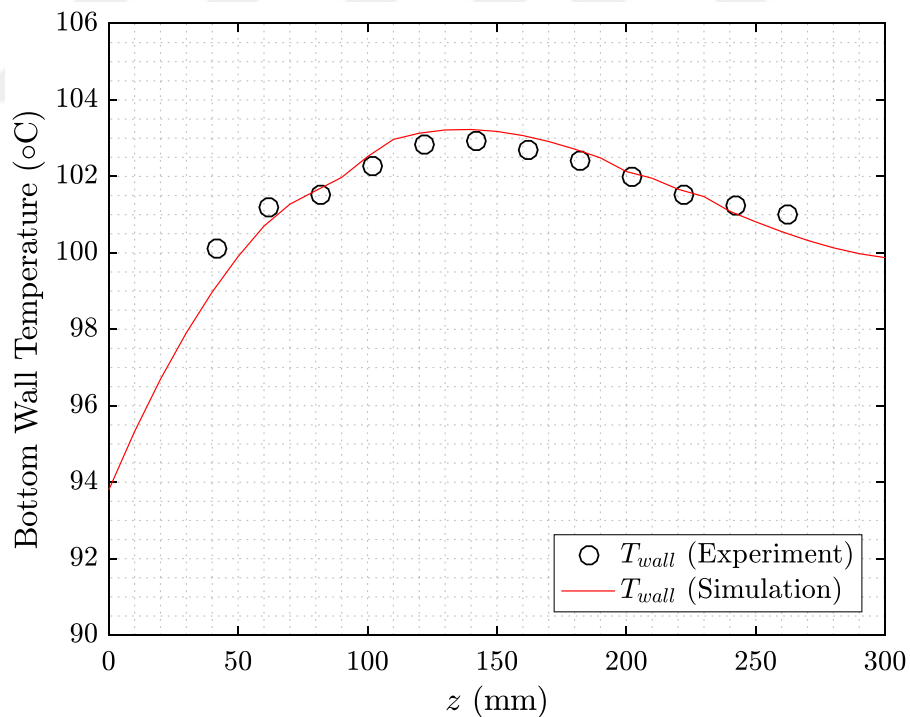


Figure 5.18. Comparison of the coolant bottom wall ($x = 0.75$ mm line) temperature with experiment data (Test-7)

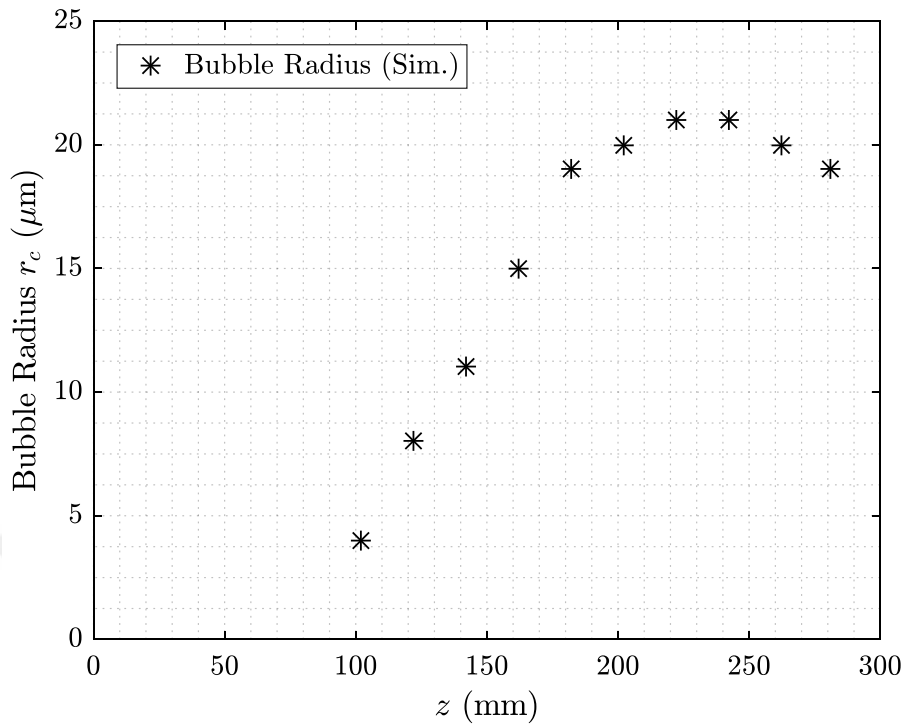


Figure 5.19. Predicted bubble radius change by simulation through the channel for Test-7

The pressure drop on the test specimen for Test-7 is calculated as 0.21 bar. Compared with the experimental value (0.23 bar), the difference is below 10%.

A snapshot of a part of the channel at the last time step is presented in Figure 5.20. Looking to the left of the figure, the bubbles are barely visible, even if we are examining only 5 mm of the canal. One of the two bubbles (the bubble on $x = 0$ mm line) is shown more closely on the right of Figure 5.20. The velocity vectors around the bubble is shown in Figure 5.21. Based on the shape of the bubble and the velocity vectors, it is evident that the bubble is starting to detach from the surface. The figure also shows the adaptive mesh refinement (AMR) by examining the gray element edges. Both the bubble boundary and its interior are refined. If there is an opportunity to use better computational power, it would be beneficial to improve the resolution of the velocity field around the bubble by enhancing the mesh.

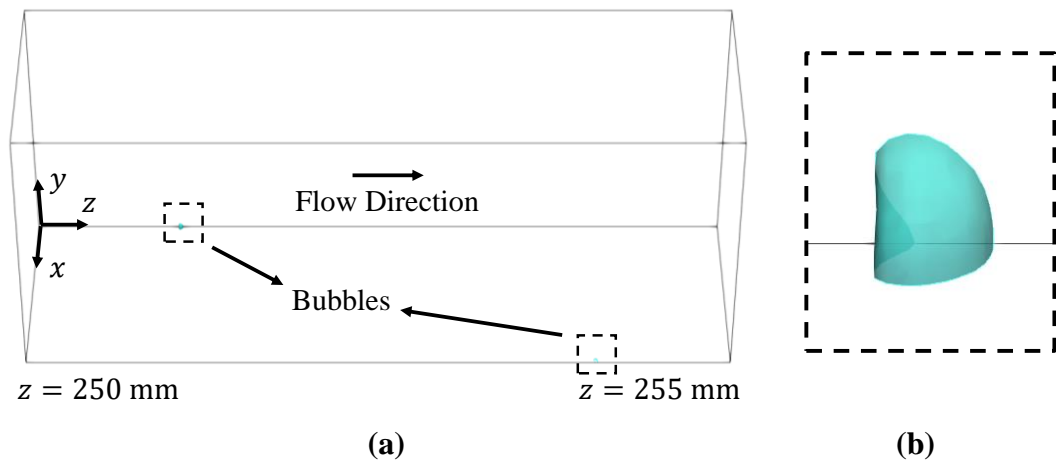


Figure 5.20. A snapshot of the simulation at the 400 ms, (a) bubble locations on the channel ($z = 250 - 255$ mm), (b) the shape of the bubble that indicated with dashed lines square on $x = 0$ mm line (the bubble boundary is transparent pale blue with $\alpha = 0.5$)

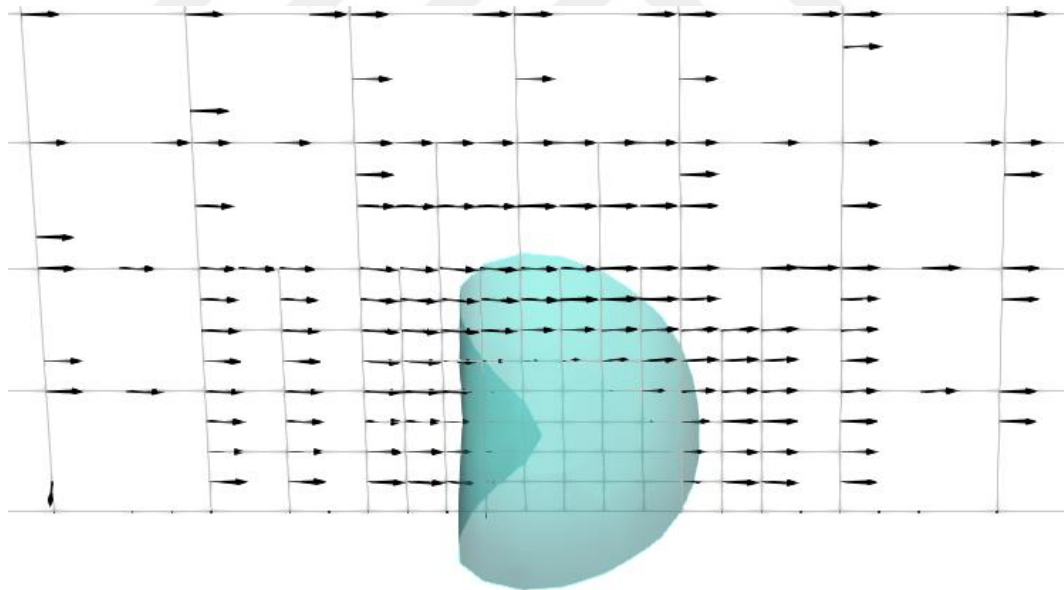


Figure 5.21. The velocity vectors (in black) around the bubble at the 400 ms, the length of the arrows indicates the velocity magnitude, gray lines shows the grid element edges (the bubble boundary is transparent pale blue with $\alpha = 0.5$)

CHAPTER 6

CONCLUSION

6.1 Conclusions

When convective heat transfer is insufficient for engine cooling, boiling flow becomes the most suitable alternative. However, in the literature there is a limited amount of test data for boiling flow in cooling channels and there is no tool in the open literature that can be used for rocket engine thermal design. In this study, a test series with subcooled boiling flow was carried out to investigate the effect of boiling on heat transfer inside a cooling channel with a rectangular cross-sectional area as used in rocket engines. The results show that the boiling flow significantly increases the heat transfer coefficient, thus demonstrating its importance for rocket engine thermal design. There are no correlations in the literature modeling heat transfer for a rectangular duct. Using the test data obtained in this study, it is shown that the Sieder and Tate equation for single-phase flows in circular ducts and its corrected version with the model developed by Mohammed for subcooled flow boiling can predict the heat transfer coefficient with high accuracy (<7% error). This proves that the Sieder and Tate and Mohammed correlations can be used in design tools to be developed.

The developed rocket engine design toolkit consists of 3 tools. The 1D design tool is used to perform sensitivity analysis for the design space in the absence or neglect of boiling using the thermal circuit principle. A 2D FDM solver, the first open source solver in the literature, was developed to evaluate the performance of the design alternatives identified by the 1D solver and to detect and analyze the effect of subcooled flow boiling.

Although the use of boiling flow in a rocket engine contributes significantly to heat transfer, bubbles generated by boiling must not be allowed to reach the injector at the end of the cooling channel or cause a blockage in the channel or injector. In order to determine the size of the bubbles and the locations of their formation and vanish, a 3D solver was developed by updating an existing solver in the OpenFOAM framework and implementing adaptive mesh refinement capability. For the boiling problem where only the bubble boundary needs to be modeled with a finer mesh, the use of AMR is shown to provide 5-6 times speedup over the use of a fine uniform grids. Two different phase change models were used to model the mass transfer between phases. Lee's method successfully models the initial bubble formation due to boiling, yet deviations occur as the bubble grows, whereas Rattner's technique is unable to model the initial bubble formation by boiling, but is able to model the steady growth and contraction of a bubble already of a certain size.

All three solvers have been verified and validated using results from the available literature and results obtained in the experiments conducted in this thesis. As a result, a design toolkit for rocket engine regenerative cooling design were developed in the scope of this thesis.

6.2 Recommendations for Future Work

The following potential areas for improvement and additions to the toolkit are highlighted for the three solvers.

The implementation of an optimization algorithm in the 1D solver will make it possible to obtain the optimal cooling channel design for the specified conditions in a larger design space.

The 2D solver calculates the temperature distributions assuming that the coolant is the bulk liquid at each station. However, this method can introduce errors, especially in high aspect ratio cooling channels (HARCC) used with cryogenic propellants. In order to investigate the stratification phenomenon in cryogenic liquids with this

solver, the bulk coolant approach needs to be changed to a discretized one. In addition, gaining the ability to generate the necessary mesh and boundary conditions for a blocked channel problem (Naraghi, 2002; Suer, 2019) is important for investigating the performance of the cooling channel under off-design conditions.

For the developed OpenFOAM solver, it may be efficient to develop a hybrid method in which the two phase change models (Lee's method and Rattner's model) are used together. Finally, an investigation of the effects of surface tension models can be of great importance for the accurate determination of the bubble shape.



REFERENCES

- AK Steel 316L Austenitic Stainless steel*. AK Steel 316l Austenitic Stainless Steel. (n.d.). Retrieved December 29, 2022, from <http://www.matweb.com/search/datasheettext.aspx?matguid=9e9ab696974044cab4a7fd83687934eb>
- ANSYS Fluent Software: CFD Simulation*. (n.d.). Available: <https://www.ansys.com/products/fluids/ansys-fluent>. [Accessed: 04-Nov-2018].
- Bartz, D. R. (1957). A Simple Equation for Rapid Estimation of Rocket Nozzle Convective Heat Transfer Coefficient. *Journal of Jet Propulsion*, 27(1), 49–53. <https://doi.org/10.2514/8.12572>
- Bhaga, D., & Weber, M. E. (1981). Bubbles in Viscous Liquids: Shapes, Wakes and Velocities. *Journal of Fluid Mechanics*, 105(-1), 61. <https://doi.org/10.1017/s002211208100311x>
- Boysan, M. E. (2008). *Analysis of Regenerative Cooling in Liquid Propellant Rocket Engines* (thesis). Ankara.
- Boysan, M. E. & Ulas, A. (2013). Numerical Analysis of regenerative cooling in liquid propellant rocket engines. *Aerospace Science and Technology*, 24(1), 187–197. <https://doi.org/10.1016/j.ast.2011.11.006>
- Brackbill, J. U., Kothe, D. B., & Zemach, C. (1992). A Continuum Method for Modeling Surface Tension. *Journal of Computational Physics*, 100(2), 335–354. [https://doi.org/10.1016/0021-9991\(92\)90240-y](https://doi.org/10.1016/0021-9991(92)90240-y)

- Carlile, J. & Quentmeyer, R. (1992). An experimental investigation of high-aspect-ratio cooling passages. *28th Joint Propulsion Conference and Exhibit*.
<https://doi.org/10.2514/6.1992-3154>
- Castro, A. J., Maprelian, E., & Ting, D. K. (2001). Onset of nucleate boiling and onset of fully developed subcooled boiling using pressure transducers signals spectral analysis. *Journal of the Brazilian Society of Mechanical Sciences*, 23(4), 513–522. <https://doi.org/10.1590/s0100-73862001000400012>
- Chen, L., Tian, Y., & Karayiannis, T. (2006). The Effect of Tube Diameter on Vertical Two-phase Flow Regimes in Small Tubes. *International Journal of Heat and Mass Transfer*, 49(21-22), 4220-4230.
[doi:10.1016/j.ijheatmasstransfer.2006.03.025](https://doi.org/10.1016/j.ijheatmasstransfer.2006.03.025)
- COMSOL Multiphysics® Modeling Software. (n.d.). Available: <https://www.comsol.com/>. [Accessed: 16-Nov-2018].
- Crocco, L. (1967). Early Italian Rocket and Propellant Research. *First Steps Toward Space*, edited by F. C. Durant III and G. S. James, American Astronautical Society History Series, Vol. 6, Univelt, San Diego, CA, pp. 33-48.
- Davis, E. J., & Anderson, G. H. (1966). The Incipience of Nucleate Boiling in Forced Convection Flow. *AIChE Journal*, 12(4), 774–780.
<https://doi.org/10.1002/aic.690120426>
- Dhir, V. K. (1998). Boiling Heat Transfer. *Annual Review of Fluid Mechanics*, 30(2), 365-401. <https://doi.org/10.1146/annurev.fluid.30.1.365>
- Dhir, V. K. (2001). Numerical Simulations of Pool-boiling Heat Transfer. *AIChE Journal*, 47(4), 813–834. <https://doi.org/10.1002/aic.690470407>

- Dhir, V. K., Warrier, G. R., & Aktinol, E. (2013). Numerical Simulation of Pool Boiling: A Review. *Journal of Heat Transfer*, 135(6). <https://doi.org/10.1115/1.4023576>
- Diani, A., Mancin, S., Balcon, M., Savio, E., & Rossetto, L. (2017). R1234YF Flow Boiling Heat Transfer in a Rectangular Channel Heated from the Bottom. *Heat Transfer Engineering*, 39(3), 198-207. doi:10.1080/01457632.2017.1295733
- Dobrovolski, M. V. (2018). Sıvı Yakıtlı Roket Motoru. Promat Press.
- E., J., Zhang, Z., Tu, Z., Zuo, W., Hu, W., Han, D., & Jin, Y. (2018). Effect analysis on flow and boiling heat transfer performance of cooling water-jacket of bearing in the gasoline engine turbocharger. *Applied Thermal Engineering*, 130, 754–766. <https://doi.org/10.1016/j.applthermaleng.2017.11.070>
- Esmaeeli, A., & Tryggvason, G. (2004a). A front tracking method for computations of boiling in complex geometries. *International Journal of Multiphase Flow*, 30(7-8), 1037–1050. <https://doi.org/10.1016/j.ijmultiphaseflow.2004.04.008>
- Esmaeeli, A., & Tryggvason, G. (2004b). Computations of film boiling. part I: Numerical method. *International Journal of Heat and Mass Transfer*, 47(25), 5451–5461. <https://doi.org/10.1016/j.ijheatmasstransfer.2004.07.027>
- Esmaeeli, A., & Tryggvason, G. (2004c). Computations of film boiling. part II: Multi-mode film boiling. *International Journal of Heat and Mass Transfer*, 47(25), 5463–5476. <https://doi.org/10.1016/j.ijheatmasstransfer.2004.07.028>
- Froelich, A., Immich, H., Lebail, F., Popp, M., & Scheuerer, G. (1991). Three-dimensional flow analysis in a rocket engine coolant channel of high depth/width ratio. *27th Joint Propulsion Conference*. <https://doi.org/10.2514/6.1991-2183>

- Froehlich, A., Popp, M., Schmidt, G., & Thelemann, D. (1993). Heat Transfer Characteristics of H₂/O₂-Combustion Chambers. *29th Joint Propulsion Conference and Exhibit*. <https://doi.org/10.2514/6.1993-1826>
- Fuchs, T., Kern, J., & Stephan, P. (2006). A transient nucleate boiling model including microscale effects and wall heat transfer. *Journal of Heat Transfer*, *128*(12), 1257–1265. <https://doi.org/10.1115/1.2349502>
- Galvis, E., & Culham, R. (2012). Measurements and Flow Pattern Visualizations of Two-phase Flow Boiling in Single Channel Microevaporators. *International Journal of Multiphase Flow*, *42*, 52-61. doi:10.1016/j.ijmultiphaseflow.2012.01.009
- Gerstley, J. G. & Tobin, R. D. (1975). Regenerative Cooling Design and Analysis Computer Program.
- Graves, R. S., Kollie, T. G., McElroy, D. L. & Gilchrist, K. E. (1991). The Thermal Conductivity of AISI 304L Stainless Steel. *International Journal of Thermophysics*, *12*, 409-415. doi.org/10.1007/BF00500761
- Grisson, W. M. (1991). *Liquid Film Cooling in Rocket Engines*. U.S. Air Force.
- Hardt, S., & Wondra, F. (2008). Evaporation Model for Interfacial Flows based on a Continuum-field Representation of the Source Terms. *Journal of Computational Physics*, *227*(11), 5871–5895. <https://doi.org/10.1016/j.jcp.2008.02.020>
- Harmon, T. (2009). Rocketdyne - SE-7 and SE-8 Engines. Chapter 4, Appendix F.
- Hendricks, R. C., Niino, M., Kumakawa, A., Yeroshenko, V. M., Yaskin, L. A., Majumdar, A. K., & Mukerjee, T. (1986). Friction factors and heat transfer coefficients for hydrogen systems operating at supercritical pressures.

- International Symposium on Hydrogen Systems*, 185–196.
<https://doi.org/10.1016/b978-1-4832-8375-3.50078-3>
- Hirt, C. W., & Nichols, B. D. (1981). Volume of Fluid (VOF) Method for the Dynamics of Free Boundaries. *Journal of Computational Physics*, 39(1), 201–225. [https://doi.org/10.1016/0021-9991\(81\)90145-5](https://doi.org/10.1016/0021-9991(81)90145-5)
- Hua, J., & Lou, J. (2007). Numerical Simulation of Bubble Rising in Viscous Liquid. *Journal of Computational Physics*, 222(2), 769–795.
<https://doi.org/10.1016/j.jcp.2006.08.008>
- Huang, Q., Jia, L., Dang, C., & Yang, L. (2018). Experimental Study on Flow Boiling of Deionized Water in a Horizontal Long Small Channel. *Journal of Thermal Science*, 27(2), 157-166. doi:10.1007/s11630-018-0996-1
- Huff, N. E. V., & Fairchild, D. A. (1972). *Liquid Rocket Engine Fluid-cooled Combustion Chambers*. National Aeronautics and Space Administration.
- Huzel, D. K., Huang, D. H., & Arbit, H. (1992). Modern Engineering for Design of Liquid-propellant Rocket Engines. *American Inst. of Aeronautics and Astronautics*.
- Hysing, S., Turek, S., Kuzmin, D., Parolini, N., Burman, E., Ganesan, S., & Tobiska, L. (2009). Quantitative Benchmark Computations of Two-dimensional Bubble Dynamics. *International Journal for Numerical Methods in Fluids*, 60(11), 1259–1288. <https://doi.org/10.1002/flid.1934>
- Incropera, F. P. (2007). *Fundamentals of heat and mass transfer with introduction to mass and heat transfer*. John Wiley & Sons Inc.
- Ishimoto, T. & Fink, L. (1971). Systems Improved Numerical Differencing Analyzer (SINDA): Engineering-program Manual. *Computer Science*.

- Juric, D., & Tryggvason, G. (1998). Computations of Boiling Flows. *International Journal of Multiphase Flow*, 24(3), 387–410. [https://doi.org/10.1016/s0301-9322\(97\)00050-5](https://doi.org/10.1016/s0301-9322(97)00050-5)
- Kakaç S., & Yener, Y. (1995). *Convective Heat Transfer*. CRC Press.
- Kakaç S., Bergles, A. E., & Fernandes, O. E. (1988). *Two-phase flow heat exchangers: Thermal-Hydraulic Fundamentals and Design: Proceeding of the Nato Advanced Study Institute on Thermal-Hydraulic Fundamentals and design of two-phase flow heat exchangers, póvoa de Varzim, Portugal, July 6-17, 1987*. Published in cooperation with NATO Scientific Affairs Division by Kluwer Academic.
- Kandlikar, S. G. (1998). Heat transfer characteristics in partial boiling, fully developed boiling, and significant void flow regions of subcooled flow boiling. *Fluids Engineering*. <https://doi.org/10.1115/imece1997-0765>
- Kang, Y. D., & Sun, B. (2011). Numerical simulation of liquid rocket engine thrust chamber regenerative cooling. *Journal of Thermophysics and Heat Transfer*, 25(1), 155–164. <https://doi.org/10.2514/1.47701>
- Kern, J., & Stephan, P. (2003a). Investigation of Decisive Mixture Effects in Nucleate Boiling of Binary Mixtures Using a Theoretical Model. *Journal of Heat Transfer*, 125(6), 1116–1122. <https://doi.org/10.1115/1.1622716>
- Kern, J., & Stephan, P. (2003b). Theoretical model for nucleate boiling heat and mass transfer of binary mixtures. *Journal of Heat Transfer*, 125(6), 1106–1115. <https://doi.org/10.1115/1.1622717>
- Kline, S. J., & McClintock, F. A. (1953). “Describing Uncertainties in Single-sample Experiments”. *Mechanical Engineering*, Vol.75, no. 1, pp. 3-8.

- Kumakawa, A., Niino, M., Hendricks, R. C., Giarratano, P.J., & Arp, V.D. (1986). Volume-energy parameters for heat transfer to supercritical fluids. *Proceeding of the Fifteenth International Symposium of Space Technology and Science*, 185–196. <https://doi.org/10.1016/b978-1-4832-8375-3.50078-3>
- Kunkelmann, C., Stephan, P., & Jakirlić Suad. (2011). *Numerical Modeling and Investigation of Boiling Phenomena* (thesis). Darmstadt.
- Lee, W. H. (2013). A Pressure Iteration Scheme for Two-phase Flow Modeling. *Computational Methods for Two-Phase Flow and Particle Transport*, 61–82. https://doi.org/10.1142/9789814460286_0004
- Li, D., & Dhir, V. K. (2007). Numerical study of single bubble dynamics during Flow Boiling. *Journal of Heat Transfer*, 129(7), 864–876. <https://doi.org/10.1115/1.2717942>
- Lin, S., Kew, P., & Cornwell, K. (2001). Flow boiling of refrigerant r141b in small tubes. *Chemical Engineering Research and Design*, 79(4), 417-424. doi:10.1205/026387601750282346
- Liu, D., & Garimella, S. V. (2007). Flow Boiling Heat Transfer in Microchannels. *Journal of Heat Transfer*, 129(10), 1321-1332. <https://doi.org/10.1115/1.2754944>
- Liu, D., Lee, P., & Garimella, S. V. (2005). Prediction of the Onset of Nucleate Boiling in Microchannel Flow. *International Journal of Heat and Mass Transfer*, 48(25-26), 5134-5149. doi:10.1016/j.ijheatmasstransfer.2005.07.021
- Liu, D., Weng, X., & Xu, X. (2011). Experimental Study on the Heat Transfer Coefficient of Water Flow Boiling in Mini/microchannels. *Experimental Thermal and Fluid Science*, 35(7), 1392-1397. doi:10.1016/j.expthermflusci.2011.05.007

- McCarthy, J. R., & Wolf, H. (1960). Forced Convection Heat Transfer To Gaseous Hydrogen At High Heat Flux And High Pressure In A Smooth, Round, Electrically Heated Tube. *ARS Journal*, 30(4), 423–425. <https://doi.org/10.2514/8.5092>
- Meyer, M. (1995). Electrically Heated Tube Investigation of Cooling Channel Geometry Effects. *31st Joint Propulsion Conference and Exhibit*. <https://doi.org/10.2514/6.1995-2500>
- Mohammed, S. (1977) A General Correlation for Heat Transfer During Subcooled Boiling in Pipes and Annuli, *ASHRAE Transactions*, vol. 83, no. 1, pp. 202–217.
- Mukherjee, A., & Dhir, V. K. (2004). Study of lateral merger of vapor bubbles during nucleate pool boiling. *Journal of Heat Transfer*, 126(6), 1023–1039. <https://doi.org/10.1115/1.1834614>
- Mukherjee, A., & Kandlikar, S. G. (2005). Numerical simulation of growth of a vapor bubble during flow boiling of water in a microchannel. *Microfluidics and Nanofluidics*, 1(2), 137–145. <https://doi.org/10.1007/s10404-004-0021-8>
- Mukherjee, A., & Kandlikar, S. G. (2007). Numerical study of single bubbles with dynamic contact angle during nucleate pool boiling. *International Journal of Heat and Mass Transfer*, 50(1-2), 127–138. <https://doi.org/10.1016/j.ijheatmasstransfer.2006.06.037>
- Mukherjee, A., Kandlikar, S. G., & Edel, Z. J. (2011). Numerical study of bubble growth and wall heat transfer during flow boiling in a microchannel. *International Journal of Heat and Mass Transfer*, 54(15-16), 3702–3718. <https://doi.org/10.1016/j.ijheatmasstransfer.2011.01.030>

- Nabil, M., & Rattner, A. S. (2016). Interthermalphasechange foam—A Framework for Two-phase Flow Simulations with Thermally Driven Phase Change. *SoftwareX*, 5, 216–226. <https://doi.org/10.1016/j.softx.2016.10.002>
- Naraghi, M. H. (1987). *A Two-dimensional Finite Difference Program for Thermal Analysis of Rocket Thrust Chambers*. NTIS.
- Naraghi, M. H. (2002). User Manual For RTE2002 Version 1: A Computer Code for Three-Dimensional Rocket Thermal Evaluation.
- Naraghi, M. H. (2015). *Thermal Analysis Of Liquid Rocket Engines*. nanopdf. Retrieved December 29, 2022, from https://nanopdf.com/download/lp-heat-transfer-notes_pdf
- Naraghi, M., & Armstrong, E. (1988). Three Dimensional Thermal Analysis of Rocket Thrust Chambers. *23rd Thermophysics, Plasmadynamics and Lasers Conference*. <https://doi.org/10.2514/6.1988-2643>
- Naraghi, M. H., & Foulon, M. (2008). A Simple Approach for Thermal Analysis of Regenerative Cooling of Rocket Engines. *Volume 10: Heat Transfer, Fluid Flows, and Thermal Systems, Parts A, B, and C*. <https://doi.org/10.1115/imece2008-67988>
- NASA. (2017). “Space launch report - NASA.” [Online]. Available: <https://sma.nasa.gov/LaunchVehicle/assets/space-launch-report-falcon-9-data-sheet.pdf>. [Accessed: 18-Dec-2022].
- OpenFOAM® - Official home of The Open Source Computational Fluid Dynamics (CFD) Toolbox*. (n.d.). Available: <https://www.openfoam.com/>. [Accessed: 05-Nov-2017].

- Özdemir, M. R. (2016). *Single-phase Flow and Flow Boiling of Water in Rectangular Metallic Microchannels* (Doctor of Philosophy thesis). Brunel University.
- Özdemir, M. R., Mahmoud, M. M., & Karayiannis, T. G. (2020). Flow Boiling of Water in a Rectangular Metallic Microchannel. *Heat Transfer Engineering*, 42(6), 492-516. doi:10.1080/01457632.2019.1707390
- Parris, D., & Landrum, B. (2005). Effect of tube geometry on regenerative cooling performance. *41st AIAA/ASME/SAE/ASEE Joint Propulsion Conference & Exhibit*. <https://doi.org/10.2514/6.2005-4301>
- Pauckert, R. P., & Tobin, R. D. (1975). (rep.). Space Shuttle Orbit Maneuvering Engine Reusable Thrust Chamber Program (pp. 123–142). Canoga Park, California: Rockwell International Rocketdyne Division. Retrieved December 30, 2022, from <https://ntrs.nasa.gov/citations/19750024091>.
- Petterson, J. (2014). *Numerical Simulations of Subcooled Nucleate Boiling for a Power Electronic Device* (Master's Thesis). Gothenburg: Chalmers University of Technology.
- Pizzarelli, M. (2007). *Modeling of Cooling Channel Flow in Liquid-Propellant Rocket Engines* (Ph.D. Thesis). Roma: Università degli Studi di Roma "La Sapienza".
- Pizzarelli, M., Nasuti, F., & Onofri, M. (2012). CFD analysis of transcritical methane in rocket engine cooling channels. *The Journal of Supercritical Fluids*, 62, 79–87. <https://doi.org/10.1016/j.supflu.2011.10.014>
- Punekar, H., & Das, S. (2013). Numerical simulation of subcooled nucleate boiling in cooling jacket of IC Engine. *SAE Technical Paper Series*. <https://doi.org/10.4271/2013-01-1651>

- Qu, W., & Mudawar, I. (2002a). Prediction and Measurement of Incipient Boiling Heat Flux in Micro-channel Heat Sinks. *International Journal of Heat and Mass Transfer*, 45(19), 3933–3945. [https://doi.org/10.1016/s0017-9310\(02\)00106-0](https://doi.org/10.1016/s0017-9310(02)00106-0)
- Qu, W., & Mudawar, I. (2002b). Transport phenomena in two-phase micro-channel heat sinks. *Heat Transfer, Volume 7*. doi:10.1115/imece2002-33711
- Raeini, A. Q., Blunt, M. J., & Bijeljic, B. (2012). Modelling Two-phase Flow in Porous Media at the Pore Scale Using the Volume-of-fluid Method. *Journal of Computational Physics*, 231(17), 5653–5668. <https://doi.org/10.1016/j.jcp.2012.04.011>
- Rider, W. J., & Kothe, D. B. (1998). Reconstructing Volume Tracking. *Journal of Computational Physics*, 141(2), 112–152. <https://doi.org/10.1006/jcph.1998.5906>
- Rocket Thermal Evaluation (RTE)*. (n.d.). Available: <http://sierraengineering.com/RTE/rte.html>. [Accessed: 29-Dec-2022].
- Samkhaniani, N., & Ansari, M. R. (2016). Numerical simulation of bubble condensation using CF-VOF. *Progress in Nuclear Energy*, 89, 120–131. <https://doi.org/10.1016/j.pnucene.2016.02.004>
- Schrage, R. W. (1953). *A Theoretical Study of Interphase Mass Transfer*. Columbia University Press.
- Shakir, S., & Thome, J. R. (1986). Boiling Nucleation of Mixtures on Smooth and Enhanced Surfaces. *Proceeding of International Heat Transfer Conference 8*. <https://doi.org/10.1615/ihtc8.4060>

- Sieder, E. N., & Tate, G. E. (1936). Heat Transfer and Pressure Drop of Liquids in Tubes. *Industrial & Engineering Chemistry*, 28(12), 1429–1435. <https://doi.org/10.1021/ie50324a027>
- Son, G., & Dhir, V. K. (1997). Numerical Simulation of Saturated Film Boiling on a Horizontal Surface. *Journal of Heat Transfer*, 119(3), 525–533. <https://doi.org/10.1115/1.2824132>
- Son, G., & Dhir, V. K. (2007). A Level Set Method For Analysis of Film Boiling on an Immersed Solid Surface. *Numerical Heat Transfer, Part B: Fundamentals*, 52(2), 153–177. <https://doi.org/10.1080/10407790701347720>
- Son, G., & Dhir, V. K. (2008). Numerical Simulation of Nucleate Boiling on a Horizontal Surface at High Heat Fluxes. *International Journal of Heat and Mass Transfer*, 51(9-10), 2566–2582. <https://doi.org/10.1016/j.ijheatmasstransfer.2007.07.046>
- Son, G., Dhir, V. K., & Ramanujapu, N. (1999). Dynamics and heat transfer associated with a single bubble during nucleate boiling on a horizontal surface. *Journal of Heat Transfer*, 121(3), 623–631. <https://doi.org/10.1115/1.2826025>
- STAR-CCM+. (n.d.). Available: <https://mdx.plm.automation.siemens.com/star-ccm-plus>. [Accessed: 14-Nov-2018].
- Steinke, M. E., & Kandlikar, S. G. (2004). An Experimental Investigation of Flow Boiling Characteristics of Water in Parallel Microchannels. *Journal of Heat Transfer*, 126(4), 518-526. doi:10.1115/1.1778187
- Stephan, P., & Hammer, J. (1994). A new model for nucleate boiling heat transfer. *Wärme- Und Stoffübertragung*, 30(2), 119–125. <https://doi.org/10.1007/bf00715018>

- Sun, T., Li, W., & Yang, S. (2013). Numerical Simulation of Bubble Growth and Departure During Flow Boiling Period by Lattice Boltzmann Method. *International Journal of Heat and Fluid Flow*, 44, 120–129. <https://doi.org/10.1016/j.ijheatfluidflow.2013.05.003>
- Sutton, G. P. (2006). *History of Liquid Propellant Rocket Engines*. American Institute of Aeronautics and Astronautics.
- Sutton, G. P., & Biblarz, O. (2017). *Rocket Propulsion Elements*. John Wiley & Sons Inc.
- Suer, T. U., Cenik, B., & Uslu, S. (2019). Regenerative Cooling of a Liquid Rocket Engine Walls Using CFD-CHT Modelling. *AIAC*.
- Suer, T. U. (2019). *Regenerative cooling of a liquid rocket engine using computational fluid dynamics and conjugate heat transfer* (Master of science thesis). TOBB University of Economics and Technology.
- Tanasawa, I. (1991). Advances in Condensation Heat Transfer. *Advances in Heat Transfer Volume 21*, 55–139. [https://doi.org/10.1016/s0065-2717\(08\)70334-4](https://doi.org/10.1016/s0065-2717(08)70334-4)
- Taylor, M. F. (1970). *Prediction of Friction and Heat-transfer Coefficients with Large Variations in Fluid Properties*. Washington, D. C., National Aeronautics and Space Administration.
- The British Library. (2013). *John Scott-Scott*. The British Library. Retrieved December 18, 2022, from <https://www.bl.uk/voices-of-science/interviewees/john-scott-scott#>
- The MathWorks Inc. (2016). Optimization Toolbox version: 7.4 (R2016a), Natick, Massachusetts: The MathWorks Inc. <https://www.mathworks.com>

- Thermophysical Properties of Fluid Systems*. NIST Chemistry WebBook, SRD 69. (2021). Retrieved December 29, 2022, from <https://webbook.nist.gov/chemistry/fluid/>
- Torres, Y., & Desmet, B. (2008). *Transferts Énergétiques Dans Les Canaux De Refroidissement Courbes De Moteurs Fusées* (thesis).
- Torres, Y., Stefanini, L., & Suslov, D. (2009). Influence of curvature in regenerative cooling system of rocket engine. *Progress in Propulsion Physics*. <https://doi.org/10.1051/eucass/200901171>
- Tryggvason, G., Bunner, B., Esmaeeli, A., Juric, D., Al-Rawahi, N., Tauber, W., Han, J., Nas, S., & Jan, Y.-J. (2001). A front-tracking method for the computations of Multiphase Flow. *Journal of Computational Physics*, 169(2), 708–759. <https://doi.org/10.1006/jcph.2001.6726>
- Wadel, M. F., (1997). Comparison of High Aspect Ratio Cooling Channel Designs for a Rocket Combustion Chamber. *33rd Joint. Propulsion Conference and Exhibit*.
- Wadel, M., & Meyer, M. (1996). Validation of High Aspect Ratio Cooling in a 89 Kn (20,000 Lbf) Thrust Combustion Chamber. *32nd Joint Propulsion Conference and Exhibit*. <https://doi.org/10.2514/6.1996-2584>
- Welch, S. W. J. (1998). Direct simulation of Vapor Bubble Growth. *International Journal of Heat and Mass Transfer*, 41(12), 1655–1666. [https://doi.org/10.1016/s0017-9310\(97\)00285-8](https://doi.org/10.1016/s0017-9310(97)00285-8)
- Welch, S. W., & Rachidi, T. (2002). Numerical Computation of Film Boiling Including Conjugate Heat Transfer. *Numerical Heat Transfer, Part B: Fundamentals*, 42(1), 35–53. <https://doi.org/10.1080/10407790190053824>

- Welch, S. W. J., & Wilson, J. (2000). A volume of fluid based method for fluid flows with phase change. *Journal of Computational Physics*, 160(2), 662–682. <https://doi.org/10.1006/jcph.2000.6481>
- Wen, D., Yan, Y., & Kenning, D. (2004). Saturated Flow Boiling of Water in a Narrow Channel: Time-averaged Heat Transfer Coefficients and Correlations. *Applied Thermal Engineering*, 24(8-9), 1207-1223. doi:10.1016/j.applthermaleng.2003.12.025
- Wennerberg, J., Jung, H., Schuff, R., Anderson, W., & Merkle, C. (2006). Study of simulated fuel flows in high aspect ratio cooling channels. *42nd AIAA/ASME/SAE/ASEE Joint Propulsion Conference & Exhibit*. <https://doi.org/10.2514/6.2006-4708>
- Wu, J., & Dhir, V. K. (2007). Numerical Simulations of Dynamics and Heat Transfer Associated with a Single Bubble in the Presence of Noncondensables. *Volume 8: Heat Transfer, Fluid Flows, and Thermal Systems, Parts A and B*. <https://doi.org/10.1115/imece2007-43551>
- Wu, J., Dhir, V. K., & Qian, J. (2007). Numerical Simulation of Subcooled Nucleate Boiling by Coupling Level-Set Method with Moving-Mesh Method. *Numerical Heat Transfer, Part B: Fundamentals*, 51(6), 535–563. <https://doi.org/10.1080/10407790601177763>
- Yagley, J., Feng, J., & Merkle, C. (1993). CFD Analyses of Coolant Channel Flowfields. *29th Joint Propulsion Conference and Exhibit*. <https://doi.org/10.2514/6.1993-1830>
- Yang, L. X., Guo, A., & Liu, D. (2014). Experimental investigation of subcooled vertical upward flow boiling in a narrow rectangular channel. *Experimental Heat Transfer*, 29(2), 221-243. doi:10.1080/08916152.2014.973978

- Yang, Z., Peng, X., & Ye, P. (2008). Numerical and Experimental Investigation of Two Phase Flow During Boiling in a Coiled Tube. *International Journal of Heat and Mass Transfer*, 51(5-6), 1003-1016. doi:10.1016/j.ijheatmasstransfer.2007.05.025
- Zhuan, R., & Wang, W. (2010). Simulation on Nucleate Boiling in Micro-channel. *International Journal of Heat and Mass Transfer*, 53(1-3), 502-512. <https://doi.org/10.1016/j.ijheatmasstransfer.2009.08.019>
- Zou, L. (2011). *Experimental Study on Subcooled Flow Boiling on Heating Surfaces with Different Thermal Conductivities* (Master's thesis, 2011). Urbana, IL.: University of Illinois.

APPENDICES

A. Tabulated Results of Experiments

Table A.1. Computational performance comparison of uniform and AMR grids

		Station 1	Station 2	Station 3	Station 4	Station 5	Station 6
Test-1	ΔT (K)	-16.23	-14.76	-13.71	-12.88	-11.99	-10.70
	q'' (W/m ²)	1.27E+05	1.35E+05	1.42E+05	1.46E+05	1.47E+05	1.49E+05
	h (W/m ² /K)	2.37E+04	2.41E+04	2.51E+04	2.58E+04	2.59E+04	2.57E+04
Test-2	ΔT (K)	-13.20	-11.28	-9.78	-9.22	-7.22	-6.88
	q'' (W/m ²)	1.47E+05	1.55E+05	1.62E+05	1.79E+05	1.83E+05	1.84E+05
	h (W/m ² /K)	2.28E+04	2.29E+04	2.34E+04	2.62E+04	2.58E+04	2.66E+04
Test-3	ΔT (K)	-10.19	-8.16	-7.76	-6.40	-5.60	-3.22
	q'' (W/m ²)	1.68E+05	1.77E+05	1.87E+05	1.90E+05	1.91E+05	2.01E+05
	h (W/m ² /K)	2.29E+04	2.33E+04	2.53E+04	2.54E+04	2.59E+04	2.59E+04
Test-4	ΔT (K)	-4.53	-3.58	-2.14	-1.19	0.02	1.57
	q'' (W/m ²)	1.93E+05	1.97E+05	2.03E+05	2.09E+05	2.15E+05	2.35E+05
	h (W/m ² /K)	2.23E+04	2.29E+04	2.35E+04	2.43E+04	2.50E+04	2.71E+04
Test-5	ΔT (K)	-3.40	0.35	2.27	2.56	2.73	3.26
	q'' (W/m ²)	2.03E+05	2.13E+05	2.26E+05	2.42E+05	2.48E+05	2.60E+05
	h (W/m ² /K)	2.24E+04	2.19E+04	2.27E+04	2.51E+04	2.67E+04	2.87E+04
Test-6	ΔT (K)	-1.56	0.50	2.32	3.40	4.46	5.56
	q'' (W/m ²)	2.15E+05	2.33E+05	2.57E+05	2.88E+05	2.97E+05	3.02E+05
	h (W/m ² /K)	2.29E+04	2.43E+04	2.64E+04	3.00E+04	3.14E+04	3.26E+04
Test-7	ΔT (K)	3.13	4.19	4.50	5.28	5.85	5.91
	q'' (W/m ²)	2.67E+05	2.84E+05	3.07E+05	3.26E+05	3.18E+05	3.52E+05
	h (W/m ² /K)	2.50E+04	2.68E+04	3.00E+04	3.26E+04	3.28E+04	3.82E+04
Test-8	ΔT (K)	4.85	5.94	6.49	6.78	6.88	7.83
	q'' (W/m ²)	3.09E+05	3.34E+05	3.57E+05	3.69E+05	3.76E+05	3.92E+05
	h (W/m ² /K)	2.84E+04	3.13E+04	3.46E+04	3.75E+04	4.03E+04	4.35E+04
Test-9	ΔT (K)	6.19	6.71	7.79	8.73	9.60	9.91
	q'' (W/m ²)	3.49E+05	3.85E+05	4.14E+05	4.43E+05	4.48E+05	4.51E+05
	h (W/m ² /K)	3.15E+04	3.59E+04	3.95E+04	4.37E+04	4.59E+04	4.89E+04

* ΔT :Wall superheat, q'' :Wall heat flux, h :Convective heat transfer coefficient

CURRICULUM VITAE

Surname, Name: Göçmen, Mahmut Murat

EDUCATION

Degree	Institution	Year of Graduation
MS	METU Mechanical Engineering	2014
BS	METU Mechanical Engineering	2011
High School	Ankara Science School, Ankara	2007

EXPERIENCE

Title	Company Name	Period
Lead Engineer	Roketsan A.Ş.	2016-Present
Senior Engineer	Arcelik A.Ş.	2015-2016

FOREIGN LANGUAGES

Advanced English

PUBLICATIONS

1. Yilmaz, C., Bayramoglu, M., Gocmen, M. M., Ulas, A., "Design and Testing of a Green Bipropellant Thruster for Satellite Propulsion", 53rd AIAA/SAE/ASEE Joint Propulsion Conference, (2017)
2. Gocmen, M. M., Sert, C., "Parallel Implementation Of The Finite Element Method On Graphics Processors For The Solution Of Incompressible Flows", ENUMATH 2015 Conference, (2015)